Fermilab

FERMILAB-THESIS-1997-38

Observation and Study of Exclusive Decays of Beauty Baryons at the Tevatron Proton–Antiproton Collider

A thesis presented to the faculty of

The Rockefeller University

in partial fulfillment of the requirements for

the degree of Doctor of Philosophy

by

Alexey Y. Titov

1997

Observation and Study of Exclusive Decays of Beauty Baryons at the Tevatron Proton–Antiproton Collider

by

Alexey Y. Titov

Abstract

In a study of proton–antiproton collisions at a center of mass energy of 1.8 TeV, we have observed the $\Lambda_b^0 \to J/\psi\,\Lambda^0$ decay and measured the Λ_b^0 mass and its production cross section times branching fraction relative to that of the $B^0 \to J/\psi\,K_s^0$ decay. In addition, we have established a limit for the production cross section times branching fraction for the decay $\Lambda_b^0 \to J/\psi\,\Lambda(1520)$. Our results are:

- $\mathrm{M}(\Lambda_b^0) = 5621 \pm 4(stat.) \pm 3(sys.)\ \mathrm{MeV}/c^2$
- $\frac{\sigma_{\Lambda_b^0} \cdot B(\Lambda_b^0 \to J/\psi\,\Lambda^0)}{\sigma_{B^0} \cdot B(B^0 \to J/\psi\,K_S^0)} = 0.27 \pm 0.12(stat.) \pm 0.05(sys.)$
- $\frac{\sigma_{\Lambda_b^0}}{\sigma_{B^0}} \cdot B(\Lambda_b^0 \to J/\psi\Lambda(1520)) < 1.38 \cdot 10^{-4}$

Acknowledgements

I would like to use this opportunity to thank several people I have been very fortunate to work with during my tenure as a graduate student. First of all, I would like to express the gratitude to my advisor, Professor Konstantin Goulianos, who provided me with an opportunity to be a member of the Rockefeller University Experimental Physics group and guided me since my early days as a graduate student working on an electromagnetic calorimeter project. My special thanks and acknowledgements go to Professor Giorgio Apollinari who turned my attention to B-baryon physics and provided me with guidance and support during the data analysis. I learned a lot from Giorgio and matured as a physicist working with him. He was very generous with me in his time and effort. I am grateful to have worked with such colleagues as Luc Demortier, who helped me to make this thesis to be less painful to a reader, Phil Melese, Anwar Bhatti, Nikos Giokaris, Roger Rusack, and my fellow graduate students Arthur Maghakian, Suren Bagdasarov, and Alexander Akopian. I am very grateful to my graduate school, the Rockefeller University, for providing me with a remarkable research opportunity.

Within the range of a dissertation, I necessarily cannot convey the scope of all the work required to produce the data analyzed herein. Without the dedicated effort of many of the members of the CDF collaboration and of those of Fermilab Accelerator Division the collection of the data used in this analysis would not have been possible. All of the people involved have my sincerest thanks. Both my analysis and I have benefitted from useful discussions with many members of the CDF Bottom Group. Special thanks

go to Vaia Papadimitriou, Slawek Tkaczyk, William Wester, Jeff Tseng, and Jonathan Lewis. The conveners, Paris Sphicas and Michael Schmidt were especially supportive.

Finally, I cannot thank my family enough for the love and support they have given me. My parents have always encouraged and inspired me to achieve in academics, particularly in the area of experimental physics.

CDF COLLABORATION

F. Abe,[17] H. Akimoto,[36] A. Akopian,[31] M. G. Albrow,[7] S. R. Amendolia,[27] D. Amidei,[20] J. Antos,[33] S. Aota,[36] G. Apollinari,[31] T. Asakawa,[36] W. Ashmanskas,[18] M. Atac,[7] F. Azfar,[26] P. Azzi-Bacchetta,[25] N. Bacchetta,[25] W. Badgett,[20] S. Bagdasarov,[31] M. W. Bailey,[22] J. Bao,[39] P. de Barbaro,[30] A. Barbaro-Galtieri,[18] V. E. Barnes,[29] B. A. Barnett,[15] M. Barone,[9] E. Barzi,[9] G. Bauer,[19] T. Baumann,[11] F. Bedeschi,[27] S. Behrends,[3] S. Belforte,[27] G. Bellettini,[27] J. Bellinger,[38] D. Benjamin,[35] J. Benlloch,[19] J. Bensinger,[3] D. Benton,[26] A. Beretvas,[7] J. P. Berge,[7] J. Berryhill,[5] S. Bertolucci,[9] B. Bevensee,[26] A. Bhatti,[31] K. Biery,[7] M. Binkley,[7] D. Bisello,[25] R. E. Blair,[1] C. Blocker,[3] A. Bodek,[30] W. Bokhari,[19] V. Bolognesi,[2] G. Bolla,[29] D. Bortoletto,[29] J. Boudreau,[28] L. Breccia,[2] C. Bromberg,[21] N. Bruner,[22] E. Buckley-Geer,[7] H. S. Budd,[30] K. Burkett,[20] G. Busetto,[25] A. Byon-Wagner,[7] K. L. Byrum,[1] J. Cammerata,[15] C. Campagnari,[7] M. Campbell,[20] A. Caner,[27] W. Carithers,[18] D. Carlsmith,[38] A. Castro,[25] D. Cauz,[27] Y. Cen,[30] F. Cervelli,[27] P. S. Chang,[33] P. T. Chang,[33] H. Y. Chao,[33] J. Chapman,[20] M. -T. Cheng,[33] G. Chiarelli,[27] T. Chikamatsu,[36] C. N. Chiou,[33] L. Christofek,[13] S. Cihangir,[7] A. G. Clark,[10] M. Cobal,[27] E. Cocca,[27] M. Contreras,[5] J. Conway,[32] J. Cooper,[7] M. Cordelli,[9] C. Couyoumtzelis,[10] D. Crane,[1] D. Cronin-Hennessy,[6] R. Culbertson,[5] T. Daniels,[19] F. DeJongh,[7] S. Delchamps,[7] S. Dell'Agnello,[27] M. Dell'Orso,[27] R. Demina,[7] L. Demortier,[31] M. Deninno,[2] P. F. Derwent,[7] T. Devlin,[32] J. R. Dittmann,[6] S. Donati,[27] J. Done,[34] T. Dorigo,[25] A. Dunn,[20] N. Eddy,[20] K. Einsweiler,[18] J. E. Elias,[7] R. Ely,[18] E. Engels, Jr.,[28] D. Errede,[13] S. Errede,[13] Q. Fan,[30] G. Feild,[39] C. Ferretti,[27] I. Fiori,[2] B. Flaugher,[7]

G. W. Foster,[7] M. Franklin,[11] M. Frautschi,[35] J. Freeman,[7] J. Friedman,[19] H. Frisch,[5] Y. Fukui,[17] S. Funaki,[36] S. Galeotti,[27] M. Gallinaro,[26] O. Ganel,[35] M. Garcia-Sciveres,[18] A. F. Garfinkel,[29] C. Gay,[11] S. Geer,[7] D. W. Gerdes,[15] P. Giannetti,[27] N. Giokaris,[31] P. Giromini,[9] G. Giusti,[27] L. Gladney,[26] D. Glenzinski,[15] M. Gold,[22] J. Gonzalez,[26] A. Gordon,[11] A. T. Goshaw,[6] Y. Gotra,[25] K. Goulianos,[31] H. Grassmann,[27] L. Groer,[32] C. Grosso-Pilcher,[5] G. Guillian,[20] R. S. Guo,[33] C. Haber,[18] E. Hafen,[19] S. R. Hahn,[7] R. Hamilton,[11] R. Handler,[38] R. M. Hans,[39] F. Happacher,[9] K. Hara,[36] A. D. Hardman,[29] B. Harral,[26] R. M. Harris,[7] S. A. Hauger,[6] J. Hauser,[4] C. Hawk,[32] E. Hayashi,[36] J. Heinrich,[26] B. Hinrichsen,[14] K. D. Hoffman,[29] M. Hohlmann,[5] C. Holck,[26] R. Hollebeek,[26] L. Holloway,[13] S. Hong,[20] G. Houk,[26] P. Hu,[28] B. T. Huffman,[28] R. Hughes,[23] J. Huston,[21] J. Huth,[11] J. Hylen,[7] H. Ikeda,[36] M. Incagli,[27] J. Incandela,[7] G. Introzzi,[27] J. Iwai,[36] Y. Iwata,[12] H. Jensen,[7] U. Joshi,[7] R. W. Kadel,[18] E. Kajfasz,[25] H. Kambara,[10] T. Kamon,[34] T. Kaneko,[36] K. Karr,[37] H. Kasha,[39] Y. Kato,[24] T. A. Keaffaber,[29] K. Kelley,[19] R. D. Kennedy,[7] R. Kephart,[7] P. Kesten,[18] D. Kestenbaum,[11] H. Keutelian,[7] F. Keyvan,[4] B. Kharadia,[13] B. J. Kim,[30] D. H. Kim,[7a] H. S. Kim,[14] S. B. Kim,[20] S. H. Kim,[36] Y. K. Kim,[18] L. Kirsch,[3] P. Koehn,[23] K. Kondo,[36] J. Konigsberg,[8] S. Kopp,[5] K. Kordas,[14] A. Korytov,[8] W. Koska,[7] E. Kovacs,[7a] W. Kowald,[6] M. Krasberg,[20] J. Kroll,[7] M. Kruse,[30] T. Kuwabara,[36] S. E. Kuhlmann,[1] E. Kuns,[32] A. T. Laasanen,[29] S. Lami,[27] S. Lammel,[7] J. I. Lamoureux,[3] M. Lancaster,[18] T. LeCompte,[1] S. Leone,[27] J. D. Lewis,[7] P. Limon,[7] M. Lindgren,[4] T. M. Liss,[13] J. B. Liu,[30] Y. C. Liu,[33] N. Lockyer,[26] O. Long,[26] C. Loomis,[32] M. Loreti,[25] J. Lu,[34] D. Lucchesi,[27] P. Lukens,[7] S. Lusin,[38] J. Lys,[18] K. Maeshima,[7] A. Maghakian,[31] P. Maksimovic,[19]

M. Mangano,[27] J. Mansour,[21] M. Mariotti,[25] J. P. Marriner,[7] A. Martin,[39] J. A. J. Matthews,[22] R. Mattingly,[19] P. McIntyre,[34] P. Melese,[31] A. Menzione,[27] E. Meschi,[27] S. Metzler,[26] C. Miao,[20] T. Miao,[7] G. Michail,[11] R. Miller,[21] H. Minato,[36] S. Miscetti,[9] M. Mishina,[17] H. Mitsushio,[36] T. Miyamoto,[36] S. Miyashita,[36] N. Moggi,[27] Y. Morita,[17] A. Mukherjee,[7] T. Muller,[16] P. Murat,[27] H. Nakada,[36] I. Nakano,[36] C. Nelson,[7] D. Neuberger,[16] C. Newman-Holmes,[7] C-Y. P. Ngan,[19] M. Ninomiya,[36] L. Nodulman,[1] S. H. Oh,[6] K. E. Ohl,[39] T. Ohmoto,[12] T. Ohsugi,[12] R. Oishi,[36] M. Okabe,[36] T. Okusawa,[24] R. Oliveira,[26] J. Olsen,[38] C. Pagliarone,[27] R. Paoletti,[27] V. Papadimitriou,[35] S. P. Pappas,[39] N. Parashar,[27] S. Park,[7] A. Parri,[9] J. Patrick,[7] G. Pauletta,[27] M. Paulini,[18] A. Perazzo,[27] L. Pescara,[25] M. D. Peters,[18] T. J. Phillips,[6] G. Piacentino,[27] M. Pillai,[30] K. T. Pitts,[7] R. Plunkett,[7] L. Pondrom,[38] J. Proudfoot,[1] F. Ptohos,[11] G. Punzi,[27] K. Ragan,[14] D. Reher,[18] A. Ribon,[25] F. Rimondi,[2] L. Ristori,[27] W. J. Robertson,[6] T. Rodrigo,[27] S. Rolli,[37] J. Romano,[5] L. Rosenson,[19] R. Roser,[13] T. Saab,[14] W. K. Sakumoto,[30] D. Saltzberg,[5] A. Sansoni,[9] L. Santi,[27] H. Sato,[36] P. Schlabach,[7] E. E. Schmidt,[7] M. P. Schmidt,[39] A. Scribano,[27] S. Segler,[7] S. Seidel,[22] Y. Seiya,[36] G. Sganos,[14] M. D. Shapiro,[18] N. M. Shaw,[29] Q. Shen,[29] P. F. Shepard,[28] M. Shimojima,[36] M. Shochet,[5] J. Siegrist,[18] A. Sill,[35] P. Sinervo,[14] P. Singh,[28] J. Skarha,[15] K. Sliwa,[37] F. D. Snider,[15] T. Song,[20] J. Spalding,[7] T. Speer,[10] P. Sphicas,[19] F. Spinella,[27] M. Spiropulu,[11] L. Spiegel,[7] L. Stanco,[25] J. Steele,[38] A. Stefanini,[27] K. Strahl,[14] J. Strait,[7] R. Ströhmer,[7a] D. Stuart,[7] G. Sullivan,[5] K. Sumorok,[19] J. Suzuki,[36] T. Takada,[36] T. Takahashi,[24] T. Takano,[36] K. Takikawa,[36] N. Tamura,[12] B. Tannenbaum,[22] F. Tartarelli,[27] W. Taylor,[14] P. K. Teng,[33] Y. Teramoto,[24] S. Tether,[19] D. Theriot,[7]

T. L. Thomas,[22] R. Thun,[20] R. Thurman-Keup,[1] M. Timko,[37] P. Tipton,[30] A. Titov,[31] S. Tkaczyk,[7] D. Toback,[5] K. Tollefson,[30] A. Tollestrup,[7] H. Toyoda,[24] W. Trischuk,[14] J. F. de Troconiz,[11] S. Truitt,[20] J. Tseng,[19] N. Turini,[27] T. Uchida,[36] N. Uemura,[36] F. Ukegawa,[26] G. Unal,[26] J. Valls,[7a] S. C. van den Brink,[28] S. Vejcik, III,[20] G. Velev,[27] R. Vidal,[7] R. Vilar,[7a] M. Vondracek,[13] D. Vucinic,[19] R. G. Wagner,[1] R. L. Wagner,[7] J. Wahl,[5] N. B. Wallace,[27] A. M. Walsh,[32] C. Wang,[6] C. H. Wang,[33] J. Wang,[5] M. J. Wang,[33] Q. F. Wang,[31] A. Warburton,[14] T. Watts,[32] R. Webb,[34] C. Wei,[6] H. Wenzel,[16] W. C. Wester, III,[7] A. B. Wicklund,[1] E. Wicklund,[7] R. Wilkinson,[26] H. H. Williams,[26] P. Wilson,[5] B. L. Winer,[23] D. Winn,[20] D. Wolinski,[20] J. Wolinski,[21] S. Worm,[22] X. Wu,[10] J. Wyss,[25] A. Yagil,[7] W. Yao,[18] K. Yasuoka,[36] Y. Ye,[14] G. P. Yeh,[7] P. Yeh,[33] M. Yin,[6] J. Yoh,[7] C. Yosef,[21] T. Yoshida,[24] D. Yovanovitch,[7] I. Yu,[7] L. Yu,[22] J. C. Yun,[7] A. Zanetti,[27] F. Zetti,[27] L. Zhang,[38] W. Zhang,[26] and S. Zucchelli[2]

(CDF Collaboration)

[1] *Argonne National Laboratory, Argonne, Illinois 60439*

[2] *Istituto Nazionale di Fisica Nucleare, University of Bologna, I-40127 Bologna, Italy*

[3] *Brandeis University, Waltham, Massachusetts 02264*

[4] *University of California at Los Angeles, Los Angeles, California 90024*

[5] *University of Chicago, Chicago, Illinois 60638*

[6] *Duke University, Durham, North Carolina 28708*

[7] *Fermi National Accelerator Laboratory, Batavia, Illinois 60510*

[8] *University of Florida, Gainesville, FL 33611*

[9] *Laboratori Nazionali di Frascati, Istituto Nazionale di Fisica Nucleare, I-00044 Frascati, Italy*

[10] *University of Geneva, CH-1211 Geneva 4, Switzerland*

[11] *Harvard University, Cambridge, Massachusetts 02138*

[12] *Hiroshima University, Higashi-Hiroshima 724, Japan*

[13] *University of Illinois, Urbana, Illinois 61801*

[14] *Institute of Particle Physics, McGill University, Montreal H3A 2T8, and University of Toronto, Toronto M5S 1A7, Canada*

[15] *The Johns Hopkins University, Baltimore, Maryland 21218*

[16] *Universotät Karlsruhe, 76128 Karlsruhe, Germany*

[17] *National Laboratory for High Energy Physics (KEK), Tsukuba, Ibaraki 315, Japan*

[18] *Ernest Orlando Lawrence Berkeley National Laboratory, Berkeley, California 94720*

[19] *Massachusetts Institute of Technology, Cambridge, Massachusetts 02139*

[20] *University of Michigan, Ann Arbor, Michigan 48109*

[21] *Michigan State University, East Lansing, Michigan 48824*

[22] *University of New Mexico, Albuquerque, New Mexico 87132*

[23] *The Ohio State University, Columbus, OH 43320*

[24] *Osaka City University, Osaka 588, Japan*

[25] *Universita di Padova, Istituto Nazionale di Fisica Nucleare, Sezione di Padova, I-36132 Padova, Italy*

[26] *University of Pennsylvania, Philadelphia, Pennsylvania 19104*

[27] *Istituto Nazionale di Fisica Nucleare, University and Scuola Normale Superiore of Pisa, I-56100 Pisa, Italy*

[28] *University of Pittsburgh, Pittsburgh, Pennsylvania 15270*

[29] *Purdue University, West Lafayette, Indiana 47907*

[30] *University of Rochester, Rochester, New York 14628*

[31] *Rockefeller University, New York, New York 10021*

[32] *Rutgers University, Piscataway, New Jersey 08854*

[33] *Academia Sinica, Taipei, Taiwan 11530, Republic of China*

[34] *Texas A&M University, College Station, Texas 77843*

[35] *Texas Tech University, Lubbock, Texas 79409*

[36] *University of Tsukuba, Tsukuba, Ibaraki 315, Japan*

[37] *Tufts University, Medford, Massachusetts 02155*

[38] *University of Wisconsin, Madison, Wisconsin 53806*

[39] *Yale University, New Haven, Connecticut 06511*

Contents

Table of Contents xi

List of Figures xiii

List of Tables xvi

1 Introduction 1

2 Theory 3
- 2.1 The Standard Model . . . 3
- 2.2 Λ_b^0 Production in $p\overline{p}$ Collisions . . . 5
- 2.3 Λ_b^0 Decay . . . 9
- 2.4 Λ_b^0 Mass and Rate Expectations . . . 12

3 The Collider Detector at Fermilab 15
- 3.1 The Fermilab Tevatron Collider . . . 15
- 3.2 CDF Detector . . . 18
  - 3.2.1 Track Parameterization . . . 22
  - 3.2.2 Tracking System . . . 24
  - 3.2.3 Muon Systems . . . 31
  - 3.2.4 Calorimetry . . . 34
  - 3.2.5 Trigger . . . 35

4 Data Set 38
- 4.1 Offline Production . . . 38
- 4.2 J/ψ Selection . . . 40

5 Search for $\Lambda_b^0 \to J/\psi\,\Lambda(1520)$ 50
- 5.1 Track Selection . . . 51
- 5.2 Constrained Fits . . . 51

5.3 P_T Scale 53
5.4 $\Lambda_b^0 \to J/\psi\Lambda(1520)$ Decay Reconstruction 54
5.4.1 $\Lambda(1520)$ and K^* Candidate Selection 54
5.4.2 Λ_b^0 and B^0 Candidates 55
5.5 Cut Optimization 56
5.5.1 Additional Tracking Selection and $c\tau$ Cut 56
5.5.2 Kinematics Cuts 59
5.5.3 Check for B^0 Reflections 63

6 Limit on $\frac{\sigma_{\Lambda_b^0}}{\sigma_{B^0}} B(\Lambda_b^0 \to J/\psi\,\Lambda(1520))$ 67
6.1 Additional Selection Requirements 68
6.2 Ratio of Efficiencies and Systematic Uncertainties 71
6.3 Determination of $N_{\Lambda_b^0}$ and N_{B^0} 76
6.4 The Limit on the Branching Ratio 79

7 Observation of $\Lambda_b^0 \to J/\psi\,\Lambda$ 85
7.1 Λ and K_s^0 Candidate Selection 86
7.2 Λ_b^0 and B^0 Candidate Selection 88
7.3 Λ_b^0 Mass Determination 93
7.4 Systematic Uncertainties on the Λ_b^0 Mass Measurement 93
7.5 Determination of $\frac{\sigma_{\Lambda_b^0} \cdot B(\Lambda_b^0 \to J/\psi\,\Lambda)}{\sigma_{B^0} \cdot B(B^0 \to J/\psi\,K_s^0)}$ 97

8 Conclusions 102

Bibliography 106

List of Figures

2.1 Lowest order Feynman diagrams of the processes contributing to $b\bar{b}$ production 6
2.2 b-quark production cross section 8
2.3 Diagrams for b-quark decay 10
2.4 Lower-order Λ_b^0 decays proceeding via internal (top) and external (bottom) W emission 11

3.1 Elements in the generation and acceleration of protons and antiprotons at Fermilab 17
3.2 Topology of Tevatron Collider at Fermilab 19
3.3 Isometric cut-away view of CDF 20
3.4 Side view of the CDF detector and coordinate system 21
3.5 Track of a particle with positive charge 23
3.6 SVX barrel 26
3.7 The SVX detector ladder 27
3.8 The CTC endplate 30
3.9 Arrangement of CMU drift cells, showing a muon track 32
3.10 Location of central muon chambers within a calorimeter wedge 33

4.1 The $\mu^+\mu^-$ invariant mass reconstructed without vertex constraining the muon tracks 39
4.2 The $\mu^+\mu^-$ invariant mass distribution after vertex constraining the muon tracks 41
4.3 The P_T distribution of the muon tracks in Run 1A 43
4.4 The P_T distribution of the muon tracks in Run 1B 44
4.5 The $\mu^+\mu^-$ invariant mass distribution after the P_T cuts on the muon candidates 45
4.6 χ^2 distributions for matching between CTC tracks and muon stubs for each muon detector subsystem 47

4.7 The $\mu^+\mu^-$ invariant mass distribution after making P_T cuts and muon quality cuts 48
4.8 The $\mu^+\mu^-$ invariant mass distribution when both muons are measured in the SVX or CTC detectors 49

5.1 The transverse $\Lambda_b^0 \to J/\psi\Lambda(1520)$ event topology 52
5.2 The J/ψ–p–K (top) and J/ψ–K–π (bottom) invariant masses 57
5.3 The J/ψ–p–K (top) and J/ψ–K–π (bottom) invariant masses after the $c\tau$ cut 60
5.4 The P_T distribution of the Monte Carlo simulated Λ_b^0 and $\Lambda(1520)$ and the P_T distributions of the background from the data . . . 61
5.5 The J/ψ–p–K (top) and J/ψ–K–π (bottom) invariant mass distributions after the P_T cuts 62
5.6 The B^0 reflections, Monte Carlo 64
5.7 The J/ψ–p–K invariant mass distribution and B^0 reflections . 66

6.1 The B^0 signal after requiring the muons to be detected in the CMU system only 69
6.2 The B^0 signal after requiring the tracks to have transverse momentum above 400 MeV/c and to exit the CTC at a radius greater that 130 cm 70
6.3 The invariant mass distribution of the B^0 candidates used as a reference signal for the Λ_b branching fraction limit measurement 72
6.4 Λ_b^0 candidates rejected by the track quality requirements . . . 73
6.5 The Λ_b^0 sample used for the branching ratio limit calculation . 74
6.6 The distribution of the difference between world average and measured mass weighted by the measured mass uncertainty for the B^0 sample 78
6.7 Likelihood as a function of the number of signal events for Λ_b^0 and B^0 80
6.8 The probability distribution of observing a number of Λ_b signal events 82
6.9 $\frac{\sigma_{\Lambda_b^0}}{\sigma_{B^0}} B(\Lambda_b^0 \to J/\psi\Lambda(1520))$ distribution 83

7.1 The transverse $\Lambda_b^0 \to J/\psi\,\Lambda$ event topology 87
7.2 The $p\,\pi^-$ invariant mass distribution 89
7.3 The $\pi^+\,\pi^-$ invariant mass distribution 90
7.4 The $J/\psi\,\Lambda$ invariant mass distribution 91
7.5 The $J/\psi\,K_s^0$ invariant mass distribution 92
7.6 The measured J/ψ mass variation in the course of Run I . . . 95

7.7 The measured J/ψ mass variation as a function of the opening angle between the two muons 96
7.8 Λ_b^0 and B^0 candidates used for the Λ_b^0 production branching fraction measurement 99

8.1 Measurements of the Λ_b^0 mass by different experiments 103
8.2 Measurements of the $\Lambda_b^0 \to J/\psi\,\Lambda$ branching ratio by various experiments, and a range of theoretical predictions 105

List of Tables

2.1 Quark properties 4
2.2 Lepton properties 4
2.3 B-hadron production fractions 9
2.4 Theoretical predictions for the Λ_b^0 mass 12
2.5 Experimental results on the Λ_b^0 mass 13
2.6 Experimental results on the observation of the semileptonic $\Lambda_b^0 \to \Lambda_c^+ \ell X$ decays 13

3.1 SVX characteristics 24
3.2 Summary of CTC properties 29
3.3 Calorimetry components 35

5.1 Signal and background for different numbers of tracks with SVX information for the B^0 58
5.2 Signal and background for the different values of the the $c\tau$ cut for the B^0 58
5.3 Signal and background for several values of the the P_T cuts on B^0 and K^* 63

6.1 Systematic uncertainties on $\varepsilon_{B^0}/\varepsilon_{\Lambda_b^0}$ 75

7.1 Systematic uncertainties in the Λ_b^0 mass measurement 97
7.2 One standard deviation systematic uncertainties on $\varepsilon_{B^0}/\varepsilon_{\Lambda_b^0}$. 100

Chapter 1

Introduction

The primary object of this work is the investigation of exclusive decays of beauty baryons at CDF with the goal of measuring some of their properties like the mass and production branching fractions. The standard model [1] predicts the existence of the Λ_b^0, the lightest beauty baryon with a (udb) quark composition. In November of 1991 the UA1 collaboration reported the first observation of the Λ_b^0 in the decay channel $\Lambda_b^0 \to J/\psi\,\Lambda$ at the CERN proton-antiproton collider [2]. Using 4.7 pb^{-1} of data collected in the 1988–1989 collider runs, UA1 reconstructed 16 ± 5 Λ_b^0 events with mass $M(\Lambda_b^0) = 5640 \pm 50 \pm 30$ MeV/c^2 and found a branching ratio $\sigma_{\Lambda_b^0} \cdot B(\Lambda_b^0 \to J/\psi\,\Lambda) = (1.8 \pm 1.0)\,10^{-3}$. Both CDF [3] and LEP experiments [4, 5], failed to confirm these results and set upper limits on the Λ_b production cross section below the value claimed by UA1. Finally, after analyzing 110 pb^{-1} of data, CDF observed the $\Lambda_b^0 \to J/\psi\,\Lambda$ decay [6] and measured the Λ_b^0 mass. Using the same data we also probed the exclusive channel $\Lambda_b^0 \to J/\psi\,\Lambda(1520)$ and established an upper limit for its production rate.

An accurate measurement of the Λ_b^0 mass provides a precision test of theoretical mass predictions based on B-hadron models and is important for future beauty baryon spectroscopy. The comparison of the production branching fractions for different Λ_b^0 decay channels can provide a useful input to theorists working on B-baryon decay models [7].

Chapter 2 provides a theoretical discussion, including the motivation for B-baryon physics. Chapter 3 gives an overview of the experimental apparatus, including the Tevatron collider. The detector description emphasizes the systems used for the present analysis, particularly the tracking and muon identification systems. Chapter 4 describes the data set used in this analysis with emphasis on the final J/ψ selection. Chapter 5 describes the search for the exclusive Λ_b^0 decay channel, $\Lambda_b^0 \to J/\psi\,\Lambda(1520)$. The limit for its production rate is calculated in Chapter 6. Chapter 7 describes the experimental procedure for the reconstruction of the $\Lambda_b^0 \to J/\psi\,\Lambda$ decay, and the measurement of its branching fraction and the Λ_b^0 mass. Chapter 8 summarizes the results.

Chapter 2

Theory

2.1 The Standard Model

The Standard Model of particle physics describes the fundamental particles and their interactions. The fundamental particles are fermions and force-carrying bosons with odd half-integer and integer spin angular momentum respectively. The fermions include six quarks interacting via the strong force mediated by the exchange of gluons. The quarks are divided in three families of doublets with a quark of charge $+2/3$ matched with a quark of charge $-1/3$. Quark properties are summarized in Table 2.1 [8], where the flavor of a quark has the same sign as its charge. Quantum Chromodynamics (QCD) describes the strong interaction by using the property of $SU_c(3)$ group symmetry [9]. Quarks and gluons carry the color property. Quarks come in 3 colors (R, G, B) and gluons mediate the strong interaction between quarks.

The Electroweak theory [1] arises from the requirement of invariance of the electromagnetic and weak interactions under transformations of the

quark	charge	mass, MeV/c^2
d	-1/3	5–15
u	+2/3	2–8
s	-1/3	100–300
c	+2/3	1000–1600
b	-1/3	4100–4500
t	+2/3	176000 ± 130000

Table 2.1: Quark properties.

$SU(2)_L \otimes U(1)_Y$ group. Fermions can exist in left-handed or right-handed states (except for neutrinos which are only left-handed in the Standard Model). Leptons do not interact via the strong force, but do interact via the electroweak force and hence are arranged in a similar doublet structure. Lepton properties are summarized in Table 2.2 [8].

lepton	charge	mass, MeV/c^2
ν_e	0	$< 1.5 \cdot 10^{-5}$
e	-1	0.511
ν_μ	0	< 0.17
μ	-1	105.66
ν_τ	0	< 24
τ	-1	1777.00

Table 2.2: Lepton properties.

Leptons are directly observable in nature. Quarks, however, are not directly observed. In the Standard Model, quarks are bound in objects which are color singlets. A colored quark can be bound with an antiquark with corresponding anti-color to form a meson. Three quarks of different color can be bound to form a baryon. Mesons and baryons are collectively called hadrons to be distinguished from the leptons and gauge bosons.

2.2 Λ_b^0 Production in $p\overline{p}$ Collisions

Several aspects of hadron colliders make them suitable for measurements in B physics. At a hadron collider, large numbers of B-hadrons are produced thanks to a b-quark production cross section which is very large relative to that at $e^+ e^-$ colliders. In $p\overline{p}$ collisions, incoming u and d quarks and gluons from the proton and antiproton interact producing a $b\overline{b}$ pair. The partons in the proton and antiproton consist not only of the three valence quarks or antiquarks but also of the sea of $q\overline{q}$ pairs and gluons. Thus, b-quark production includes the following processes:

$$q + \overline{q} \rightarrow bX$$

$$g + q \rightarrow bX$$

$$g + \overline{q} \rightarrow bX$$

$$g + g \rightarrow bX$$

Figure 2.1 shows some lowest order Feynman diagrams illustrating $p\overline{p}$ production of $b\overline{b}$ pairs.

A QCD calculation of these processes and all others to next-to-leading order has been performed [10]. The calculation includes two free parameters: the b-quark mass, m_b, for which the value of 4.75 GeV/c^2 is used and a renormalization mass scale, μ, which is taken to be $\mu_0 = \sqrt{m_b^2 + P_T^2}$, where P_T is the b-quark momentum component in the plane transverse to the $p\overline{p}$ collision axis. The former is not the same value shown in Table 2.1, because the mass that enters in the calculation depends on the renormalization scheme. In our analysis we use these parameters to simulate b-quark production as described later in detail. The cross section prediction also depends upon the structure

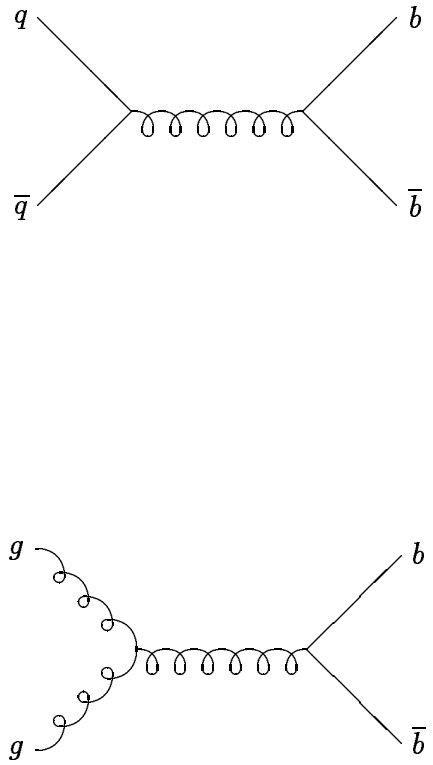

Figure 2.1: Lowest order Feynman diagrams of the processes contributing to $b\overline{b}$ production in hadron collisions.

functions which parameterize the composition and momentum distribution of quarks and gluons that make up the proton and antiproton. Using a set of parton distribution functions which have been shown to agree with the CDF data [11], one can calculate the theoretical expectation of the cross section for b-quark production as a function of the transverse momentum, P_T, of the quark. Figure 2.2 shows theoretical predictions along with measurements made by CDF.

Once b-quarks are produced they fragment into B-hadrons. The fragmentation process involves the fraction of the momentum the B-hadron carries relative to that of the original b-quark. In the Peterson model [12], this process is described by the equation

$$\mathrm{D_q^H(z) = N \cdot z^{-1}(1 - \frac{1}{z} - \frac{\epsilon_q}{1-z})^{-2}}$$

where $D_q^H(z)$ is the fragmentation function for quark q to fragment into hadron H, z is the fraction of the quark momentum carried by the hadron, N is a normalization constant, and ϵ_q is a (Peterson) fragmentation parameter. Measurements at $e^+ e^-$ experiments yield the value [13]

$$\epsilon_b = 0.006^{+0.001+0.002}_{-0.001-0.002}$$

The above argument pertains most directly to meson production via fragmentation, while baryon production requires coupling with a diquark. It is assumed for the present that the b-quark is heavy enough that the effective mass of the diquark is similar to that of the antiquark in the meson case and therefore that $\epsilon_b(\Lambda_b^0)$ is close to the inclusive ϵ_b value presented above. When performing Monte Carlo simulations, we will allow a greater variation for $\epsilon_b(\Lambda_b^0)$ than for $\epsilon_b(B^0)$ to account for this assumption.

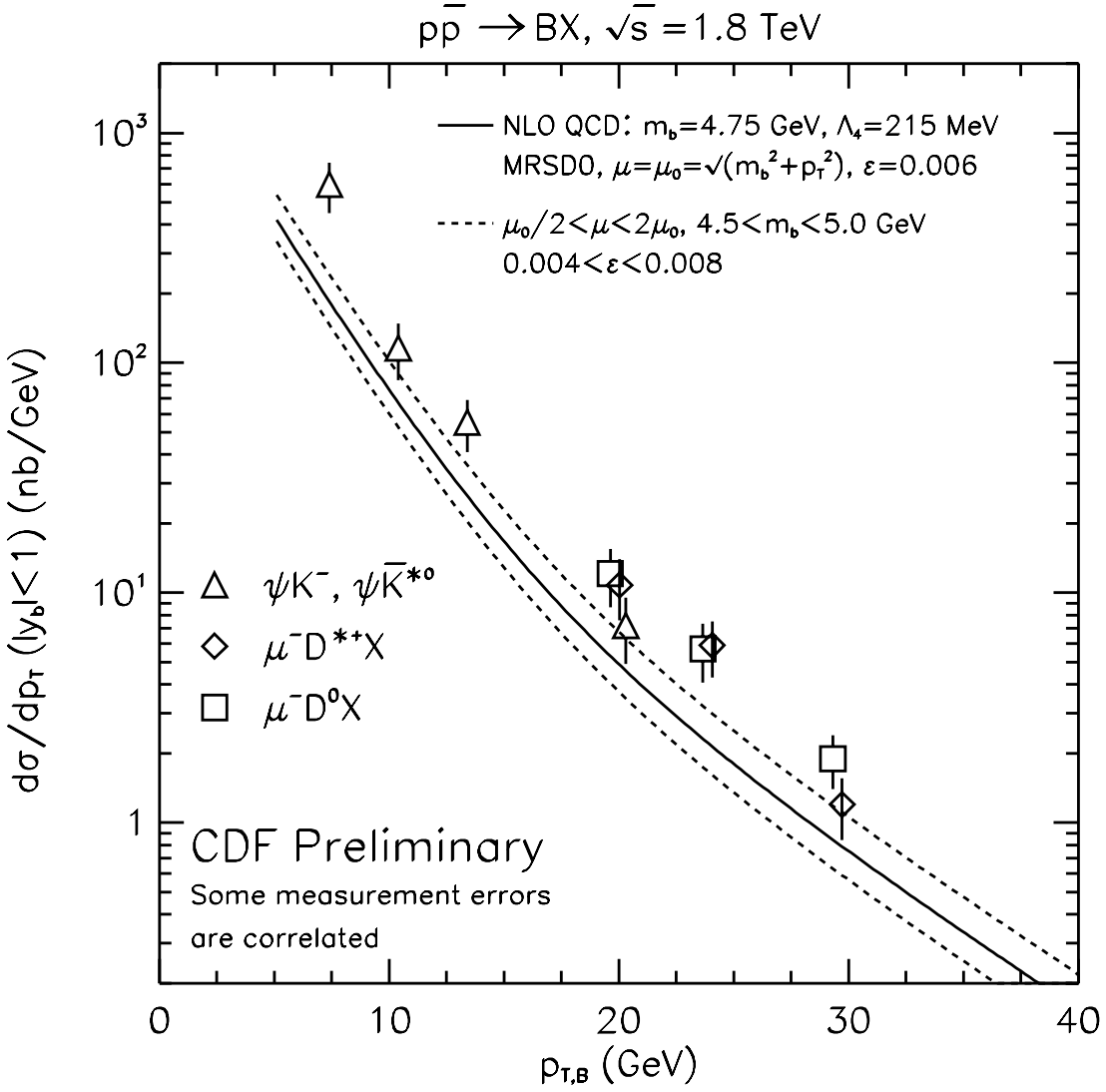

Figure 2.2: *b*-quark production cross section showing both experimental data from CDF and a range of theoretical predictions.

A second issue described by the fragmentation process is the expected species of the B-hadron. Since the s-quark is heavier than the u and d quarks, it is less likely to be created during the hadronization process. Baryon production rate is also expected to be suppressed in comparison with the B^0 and B^+ mesons production rates. Table 2.3 lists expected values for the production fractions of B-hadrons [14] based on the assumption that $f_{B^0} = f_{B^+}$ and $f_{B^0} + f_{B^+} + f_{B_s} + f_{\Lambda_b^0} = 1$.

B-hadron	Quark Composition	Fraction, %
B^+	$u\bar{b}$	37.8 ± 2.2
B^0	$d\bar{b}$	37.8 ± 2.2
B_s	$s\bar{b}$	$11.2^{+1.8}_{-1.9}$
Λ_b^0	udb	13.2 ± 4.1

Table 2.3: B-hadron production fractions.

2.3 Λ_b^0 Decay

The decays of b-quark have been studied intensively as they provide the source of information for the V_{cb} and V_{ub} elements of CKM matrix [15]. Most of B-decays proceed via a $b \rightarrow c$ transition. The $b \rightarrow c$ transition (Figure 2.3) is accompanied by the emission of a W boson. Since there is not enough mass to produce a real W, a virtual W is produced followed by the standard W decay modes. To produce the observed hadrons, the quarks must be "dressed" with other quarks, as shown in Figure 2.4. The Λ_b^0 decay proceeds either via internal W emission, where quarks from W decay join with spectator quarks, or external W emission, where the W decays into leptons or quarks that hadronize independently. Figure 2.4 shows the simplest diagrams for the

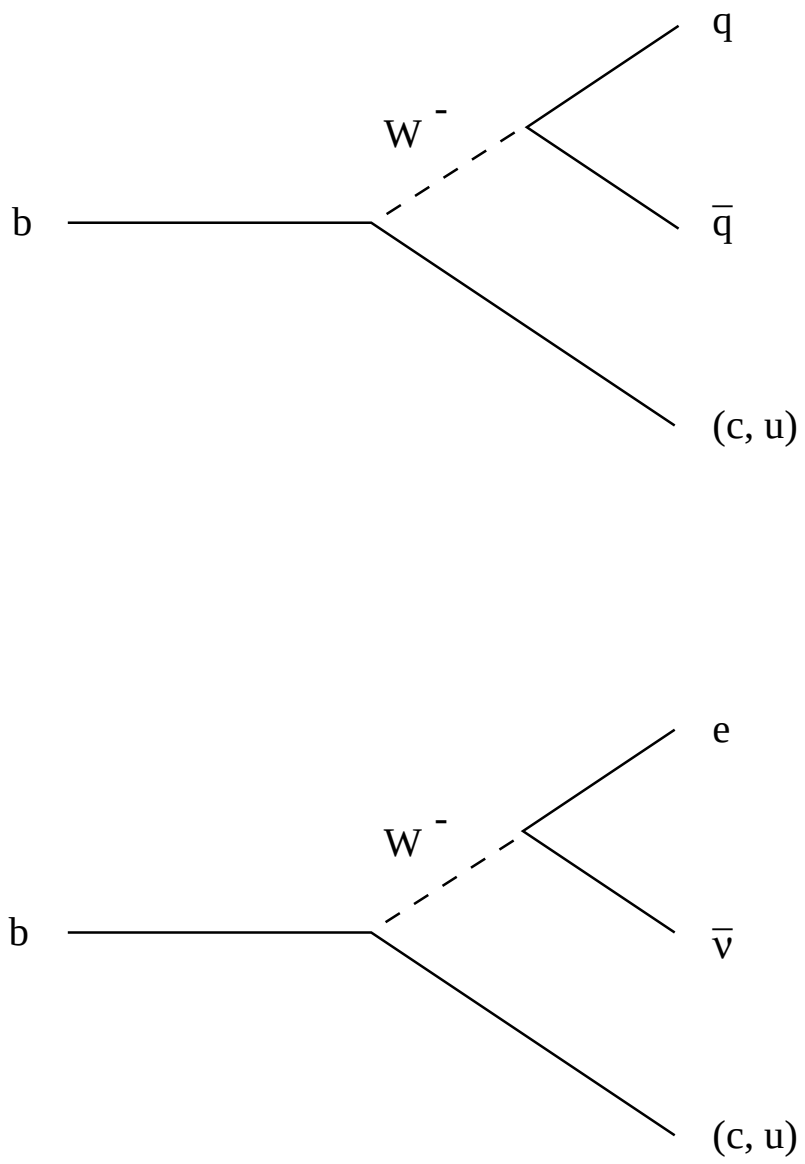

Figure 2.3: Diagrams for b-quark decay to a three-quark state (top) or a semileptonic final state (bottom). The amplitude of the $b \to u$ decay is suppressed by the factor $|\frac{V_{ub}}{V_{cb}}| = 0.08 \pm 0.02$.

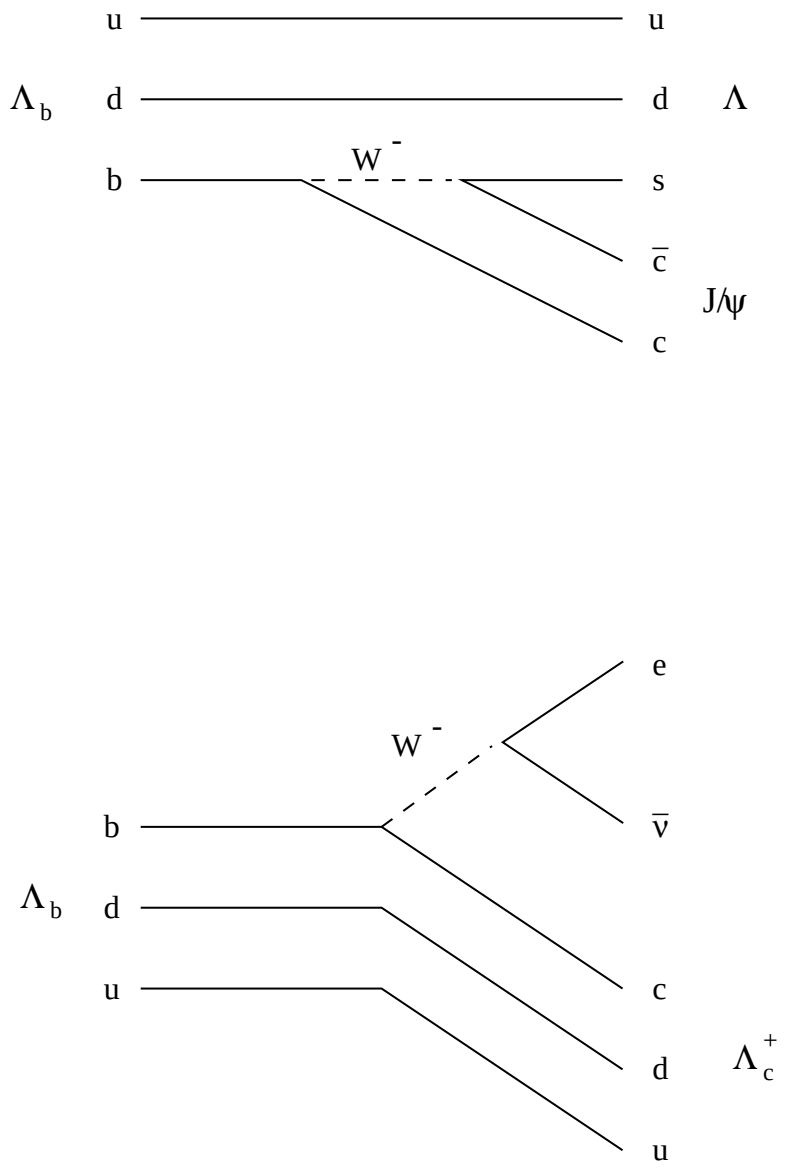

Figure 2.4: Lower-order Λ_b^0 decays proceeding via internal (top) and external (bottom) W emission.

two cases. The top diagram is an example of a color-suppressed spectator diagram. The virtual W is a color singlet and the diagram is possible only if the $\bar{c}$ from the W decay forms the color singlet J/ψ. The color suppression factor to first approximation is expected to be $1/N_c^2 = 1/9$, where $N_c = 3$ is the number of colors.

2.4 Λ_b^0 Mass and Rate Expectations

As soon as the first evidence of a Λ_b^0 signal was announced [16], an argument about its validity [17] has appeared. It became important to understand what is the expected mass of the Λ_b^0. Several studies, compiled in Table 2.4, predict that the Λ_b^0 mass should lie close to 5.6 GeV/c^2. Table 2.5 lists published experimental results of the Λ_b^0 mass measurements.

Mass, MeV/c^2	Year of Prediction	Reference
5596	1980	[18]
5585	1980	[19]
5640	1982	[20]
5580	1983	[21]
5547	1986	[22]
5379–5659	1987	[23]
5600–5660	1990	[24]
5600–5630	1991	[25]

Table 2.4: Theoretical predictions for the Λ_b^0 mass.

Recently, the Λ_b^0 semileptonic decay modes have been observed by CDF and LEP experiments. Branching fractions and lifetime measurements were performed. The measured branching fraction of inclusive semileptonic decays is in agreement with the theoretical expectations. The average lifetime is comparable with that of B-meson as expected too. These observations

Decay Channel	Events Observed	Mass, MeV/c^2	Reference
$\Lambda\, J/\psi$	16 ± 5	$5640 \pm 50 \pm 30$	UA1 [2]
$p\, D^0\, \pi^-$	52 ± 20	5640^{+100}_{-210}	SFM [26]
$\Lambda_c^+\, \pi^-\, \pi^+\, \pi^-$	90 ± 21	5650^{+150}_{-200}	SFM [26]
$\Lambda_c^+\, \pi^-$	4	$5621 \pm 17 \pm 15$	ALEPH [27]
$\Lambda_c^+\, a_1^-$	1	$5668 \pm 16 \pm 8$	DELPHI [5]

Table 2.5: Experimental results on the Λ_b^0 mass.

prove the existence of Λ_b^0. However, the semileptonic decays are not fully reconstructed (due to the presence of an undetected ν) and this makes it impossible to perform a precise mass measurement. Table 2.6 summarizes the results of measured Λ_b^0 properties and lists the references.

Events Observed	$f_{\Lambda_b} \cdot B(\Lambda_b \to \Lambda_c^+\, \ell\, X)$	Lifetime, ps	Reference
69 ± 13	$(0.8 \pm 0.3) \times 10^{-2}$	$1.14 \pm 0.22 \pm 0.07$	OPAL, [55]
107	$(1.5 \pm 0.4) \times 10^{-2}$	$1.24 \pm 0.15 \pm 0.05$	ALEPH, [56]
125	$(1.2 \pm 0.4) \times 10^{-2}$	$1.19 \pm 0.21 \pm 0.08$	DELPHI, [57]
197 ± 25	$(1.8 \pm 1.0) \times 10^{-2}$	$1.32 \pm 0.15 \pm 0.07$	CDF, [58]

Table 2.6: Experimental results on the observation of the semileptonic $\Lambda_b^0 \to \Lambda_c^+\, \ell\, X$ decays.

Theoretical studies [28, 29] estimate the branching ratio for $\Lambda_b^0 \to J/\psi\, \Lambda$ to be $B(\Lambda_b^0 \to J/\psi\, \Lambda) \leq 10^{-3}$. The Monte Carlo simulation suggests that if $B(\Lambda_b^0 \to J/\psi\, \Lambda) \approx 10^{-3}$, there should be approximately 50 reconstructed Λ_b^0 events in 110 pb^{-1} of data collected by CDF when the cuts used to suppress combinatorial backgrounds are similar to those used in B-meson reconstruction procedure [30].

The Relativistic Orsay Quark Model [31] predicts ratios of branching fractions for B-mesons which are in agreement with the CDF and CLEO

data. A calculation within the non-relativistic quark model was performed [7] since the relativistic model was not available for the calculations on baryons. The non-relativistic method is not appropriate for calculations of higher order partial waves. The calculated width ratios of the S-wave transitions of the hadronic Λ_b^0 decay channels are

$$, {}_S(\Lambda_b^0 \to J/\psi\,\Lambda)/, {}_S(\Lambda_b^0 \to J/\psi\,\Lambda(1405))/, {}_S(\Lambda_b^0 \to J/\psi\,\Lambda(1520)) = 1/0.9/0$$

According to these predictions, the decay $\Lambda_b^0 \to J/\psi\,\Lambda(1405)$ is not forbidden. Unfortunately, it always has neutral particles in the final state. Such a decay could not be observed at CDF, since the low mass resolution for neutral particles reconstructed in the calorimeter would not permit the signal to be seen above the large combinatorial background. The $\Lambda(1520)$, however, decays into a charged kaon and a proton, which enables CDF to perform a search for the $\Lambda_b^0 \to J/\psi\,\Lambda(1520)$ decay.

The disadvantage of $\Lambda_b^0 \to J/\psi\,\Lambda$ decay is that its reconstruction efficiency in CDF is limited by the Λ decay features and the detector performance. The proton from the Λ decay carries a large fraction of its parent momentum, making the pion spectrum relatively soft (see Chapter 7). The CDF tracking system is inefficient in reconstructing tracks with transverse momenta below 200 MeV/c (see Chapter 3) affecting the reconstruction efficiency of the $\Lambda_b^0 \to J/\psi\,\Lambda$ decay. The $\Lambda_b^0 \to J/\psi\,\Lambda(1520)$ decay is much less sensitive to the tracking system inefficiency at low-momenta since the $\Lambda(1520)$ decay products, kaon and proton, carry comparable fractions of the $\Lambda(1520)$ momentum. This makes a search for the $\Lambda_b^0 \to J/\psi\,\Lambda(1520)$ at CDF a reasonable task, even though its branching fraction could be smaller then that of $\Lambda_b^0 \to J/\psi\,\Lambda$.

Chapter 3

The Collider Detector at Fermilab

This chapter describes the experimental apparatus used to obtain the data for this analysis. The description includes all the steps from the production of p and $\bar{p}$ for collisions at energy $\sqrt{s} = 1.8$ TeV to the detection of the final decay products by the Collider Detector at Fermilab [32]. The detector is described with particular emphasis on the components most significant for this analysis, which includes the muon systems and the tracking systems as well as the dimuon J/ψ trigger, which allows a sample of events containing $J/\psi \rightarrow \mu^+\mu^-$ to be recorded. These events are used in selecting the final data sample for this analysis as described in the next chapter.

3.1 The Fermilab Tevatron Collider

The process of providing high energy $\bar{p}p$ collisions is outlined in Figure 3.1 and the topology of the accelerator is shown in Figure 3.2. The process begins by ionizing hydrogen gas and accelerating the H^- ions to 750 keV in

a Cockcroft-Walton electrostatic accelerator. The ions are then accelerated to 200 MeV in a 150 m long linear accelerator (linac), at the end of which they pass through a carbon foil to strip the electrons leaving only protons. These protons are stored in the Booster Ring, a synchrotron accelerator with a circumference of 475 m, that increases the energy to 8 GeV. In the Booster, proton bunches are collected and injected into a larger synchrotron with a circumference of 6.3 km, the Main Ring. At this point the proton energy is raised to 150 GeV. During $\bar{p}p$ collider activity, part of the protons are removed from the Main Ring and focused on a long beryllium target where they interact producing a number of secondary particles including antiprotons. The antiprotons are selected by magnets and stored in the Accumulator Ring. After a sufficient number of antiprotons are collected, they are reinjected first into the Main Ring (for an initial acceleration) and then into the Tevatron. The Tevatron is another circular accelerator, built from superconducting magnets, accelerating protons and antiprotons to 900 GeV in the same tunnel as the Main Ring. In collider operation, protons and antiprotons are accelerated simultaneously in counter-rotating beams and collide at regions equipped with strong focusing magnets.

The instantaneous luminosity of the Tevatron during $\bar{p}p$ collisions can be calculated using the equation:

$$\mathcal{L} = \frac{\mathrm{N_p N_{\bar{p}} f}}{4\pi r_x r_y} \tag{3.1}$$

where N_p and $N_{\bar{p}}$ are the numbers of p and $\bar{p}$ per bunch, f is the bunch "collision" frequency, and r_x and r_y are the major and minor axes of the elliptical cross section of the beam profile at the interaction point. The interaction region for the CDF experiment is at B0 (see Figure 3.2). Quadrupole magnets

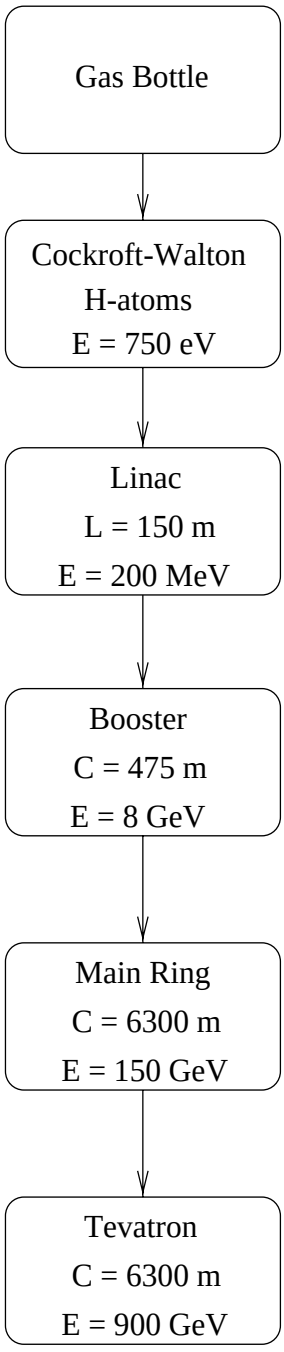

Figure 3.1: Elements in the generation and acceleration of protons and antiprotons at Fermilab.

focus the beam so that its shape at the center of the CDF detector is roughly circular in a cross section perpendicular to the beams, with a radius defined by $r = 40\,\mu$m. The longitudinal extent of the interaction region is approximately Gaussian with a width of 30 cm. In a typical collider store in run 1A (1992 – 1993) there were six bunches of 12×10^{10} protons and six bunches of 3×10^{10} antiprotons colliding every 3.5 μs. That resulted in average instantaneous luminosity of 3.5×10^{30} cm^{2}s^{-1}. Data from an integrated luminosity of approximately 20 pb^{-1} were written to tape during this run. In run 1B (1994 – 1995) the Tevatron luminosity was raised by increasing the number of protons to 22.5×10^{10} and the number of antiprotons to 6.5×10^{10} per bunch . The average instantaneous luminosity reached 8.3×10^{30} cm^{2}s^{-1}. The integrated luminosity of data recorded during run 1B was approximately 90 pb^{-1}. This analysis uses all the 110 pb^{-1} of data accumulated during the Tevatron Collider run 1A and run 1B.

3.2 CDF Detector

The CDF detector is located at the B0 interaction region of the Tevatron. CDF is a multipurpose detector consisting of tracking, calorimetry and muon subsystems. Figure 3.3 is an isometric cut-away view of CDF, showing the central, forward, and backward regions. Figure 3.4 shows a side-view cross section of 1/4 of the detector and its coordinate system. In the CDF coordinate system, z-axis is along the proton direction, x-axis points away from the Tevatron in the horizontal plane and y-axis points up; in polar coordinates, r is the radius, θ is the polar angle, and ϕ is the azimuthal angle. We will also use the parameter called pseudorapidity, defined as $\eta = -ln(tan(\theta/2))$.

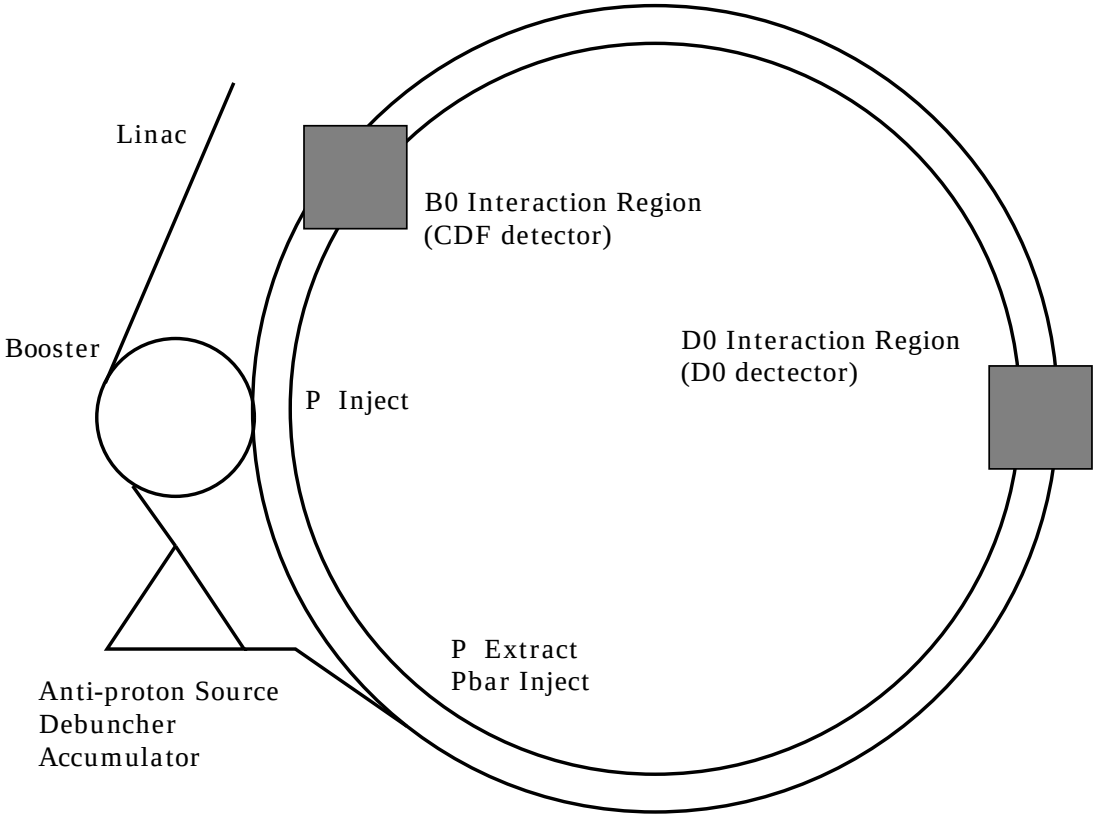

Figure 3.2: Topology of Tevatron Collider at Fermilab.

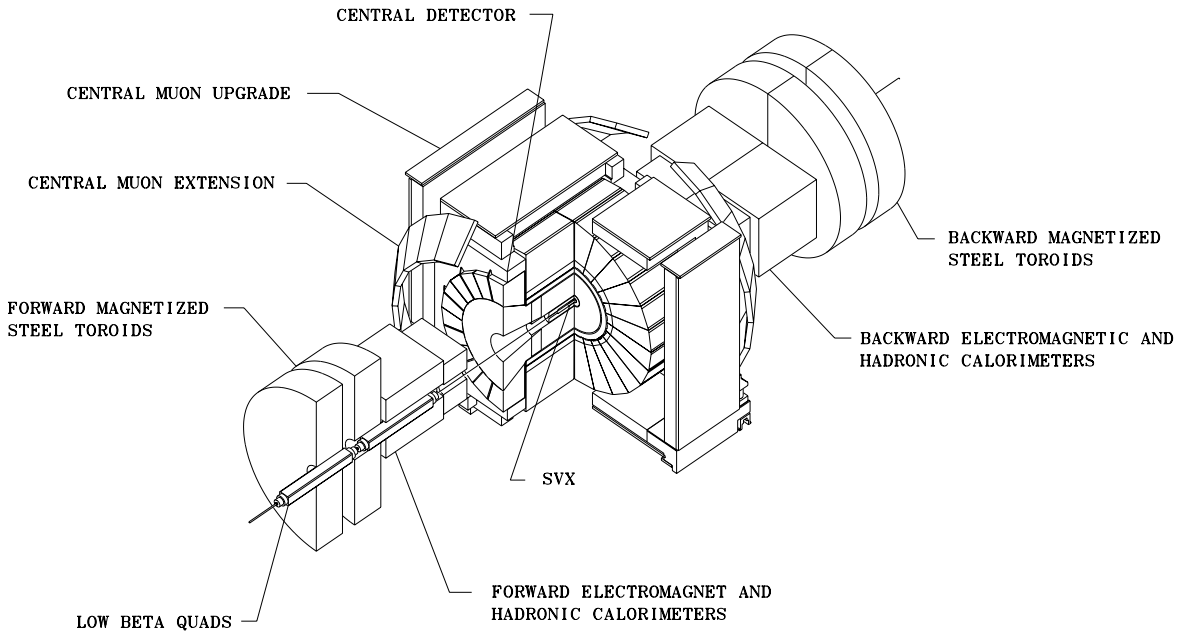

Figure 3.3: Isometric cut-away view of the CDF detector.

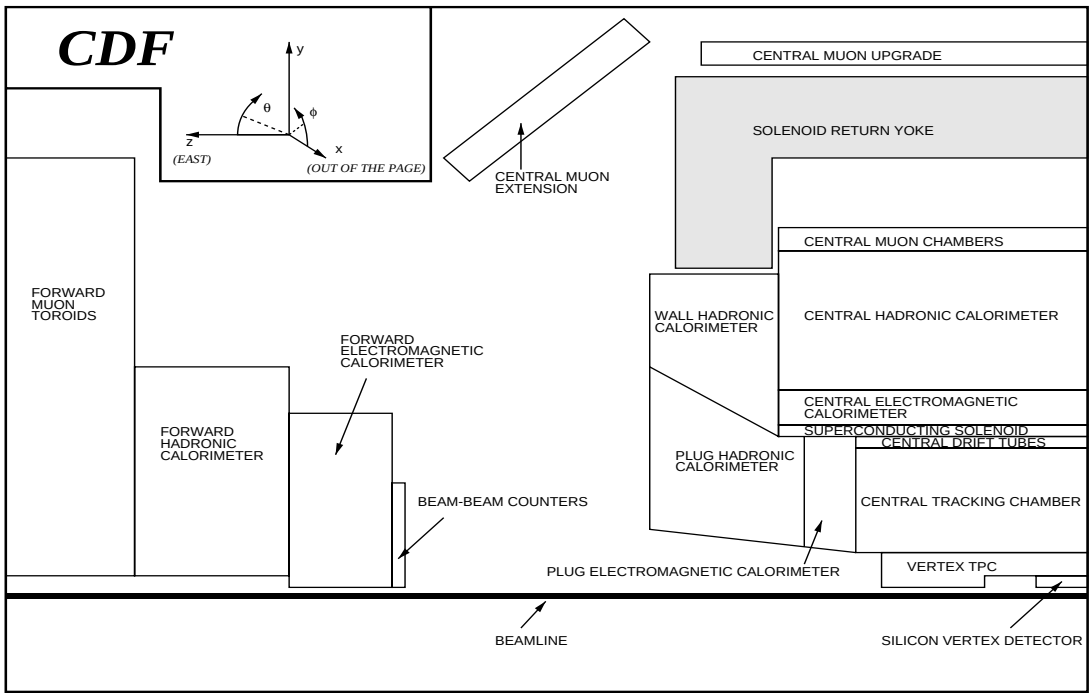

Figure 3.4: Quarter view of the CDF detector and global coordinate system.

Charged tracks are measured in the central pseudorapidity region ($|\eta| \leq 1.1$) of the detector. The tracking system achieves a momentum resolution of $\delta P_T/P_T^2 < 0.002(GeV/c)^{-1}$ using a solenoidal magnetic field of 14.1 kG and a large tracking volume. The muon system consists of drift chambers to record position information for charged particles that pass through the calorimeters. The calorimetry system consists of towers of alternating absorber and scintillator pointing to the nominal interaction vertex for energy measurements of both electromagnetic and hadronic showers.

3.2.1 Track Parameterization

In a homogenous magnetic field charged particles travel on a helix with the axis of the helix parallel to the magnetic field. At CDF the helix of a charged track is described by five parameters,

$$\vec{\alpha} = (\cot\theta,\, C,\, z_0,\, D,\, \phi_0)$$

where θ is the polar angle with respect to the proton beam direction, $C = 1/(2Q\rho)$ is the half curvature, where ρ is the radius and is the charge of the particle. z_0 is the z position at the point of closest approach, D is the impact parameter (minimum distance between helix and origin in plane transverse to the beamline), ϕ_0 is the azimuth of track at the point of closest approach. The magnetic field points in the negative z direction. The impact parameter is given by $D = Q \cdot (\sqrt{x_0^2 + y_0^2} - \rho)$, where $\rho = 1/(2QC)$ is the radius of the helix, and $(x_0,\, y_0)$ are its axis coordinates. Figure 3.5 shows the projection of the track helix in the $x - y$ plane.

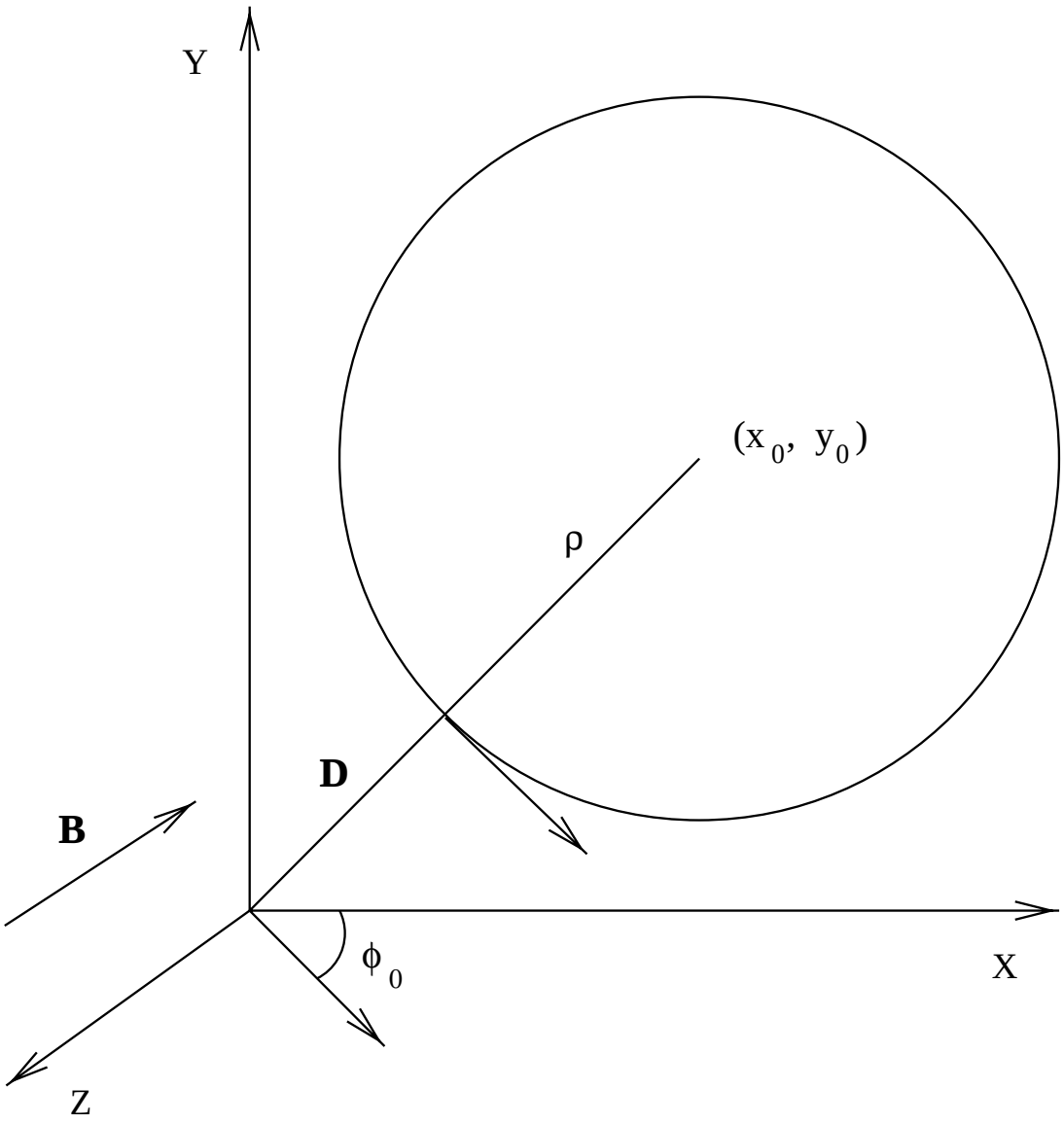

Figure 3.5: Track of a particle with positive charge.

3.2.2 Tracking System

The tracking system is used to provide position information of charged particles along their helical trajectories in the solenoidal magnetic field. It also enables us to measure the momenta of charged particles passing through the tracking system volume and to reconstruct decay vertices. The primary components of the tracking system are a solenoidal magnet, a silicon microstrip vertex detector (SVX), a vertex time projection chamber (VTX), and the central tracking chamber (CTC).

The CDF **solenoidal magnet** provides an axial magnetic field within a cylindrical volume of 3 m in diameter and 5 m in length. The magnet coil consists of NbTi/Cu superconductor. During normal operation a current of 4650 A results in a magnetic field of 14.1 kG. The magnetic field flux is returned through a steel yoke which supports the calorimeters. A precision mapping of the magnetic field is described in Reference [33].

The **silicon vertex detector** [34], SVX, shown in Figure 3.6, is the innermost tracking element. It consists of silicon microstrip detectors surrounding the beam pipe. SVX provides precise tracking in the $r - \phi$ plane and is used to obtain a measurement of the impact parameter of traversing particles.

Layer	Radius, cm	Width, cm	Pitch, μm	Number of Strips	Number of Chips
0	2.9899	1.6040	60	256	2
1	4.2710	2.3720	60	384	3
2	5.7022	3.1400	60	512	4
3	7.8508	4.2925	55	768	6

Table 3.1: Mechanical characteristics of SVX layers.

The SVX consists of two barrels which are situated side by side. A barrel is composed of 12 wedges, each of which covers 30 degrees in azimuth. Every wedge comprises four layers of 280 μm thick silicon strip detectors. Each layer, called ladder, has three 8.5 cm long rectangular silicon strip detectors, as shown on Figure 3.7. The total effective length of a ladder is 25 cm. The strips are wirebonded to the SVX readout chips mounted on the ear card (see Figure 3.7). On each detector face there are hundreds of metal strips, each separated by 55 or 60 μm. The bulk silicon is n-doped, and under each strip there is a p-doped region, resulting in an array of pn diodes. Passing charged particles excite electrons into conduction energy bands. The resulting charges and "holes" are swept out of the diode region by the electric fields and picked up by the metal strips. The high strip density results in a transverse impact parameter resolution of the SVX of about 40 μm, which is very valuable for studying particles with a lifetime of the order of a picosecond when selecting track combinations originated from a displaced secondary vertex, like those resulting from the decays of B-hadrons. The specifications of different SVX layers are given in Table 3.1. To position the measurements as close as possible to the beam pipe, Layer 0 and Layer 3 have the active silicon facing towards the beam pipe while Layer 1 and Layer 2 face outward.

For the Tevatron run 1B a new silicon vertex detector, SVX$'$ [35], has been installed to replace the SVX. It has the same overall configuration as the SVX, although several differences are improving the performance. The differences include higher radiation hardness, a readout chip with a higher gain, and a lower noise level due to the AC coupling of the readout chip, so that radiation induced currents do not saturate the input.

The information provided by the SVX significantly improves the mea-

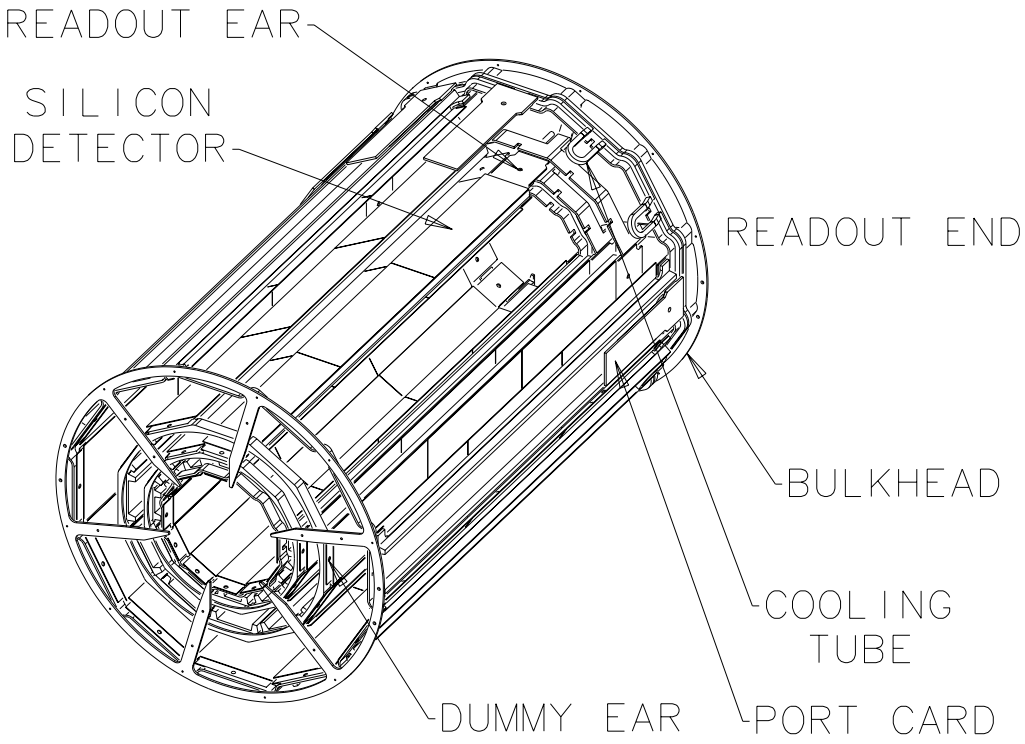

Figure 3.6: Isometric view of the SVX barrel.

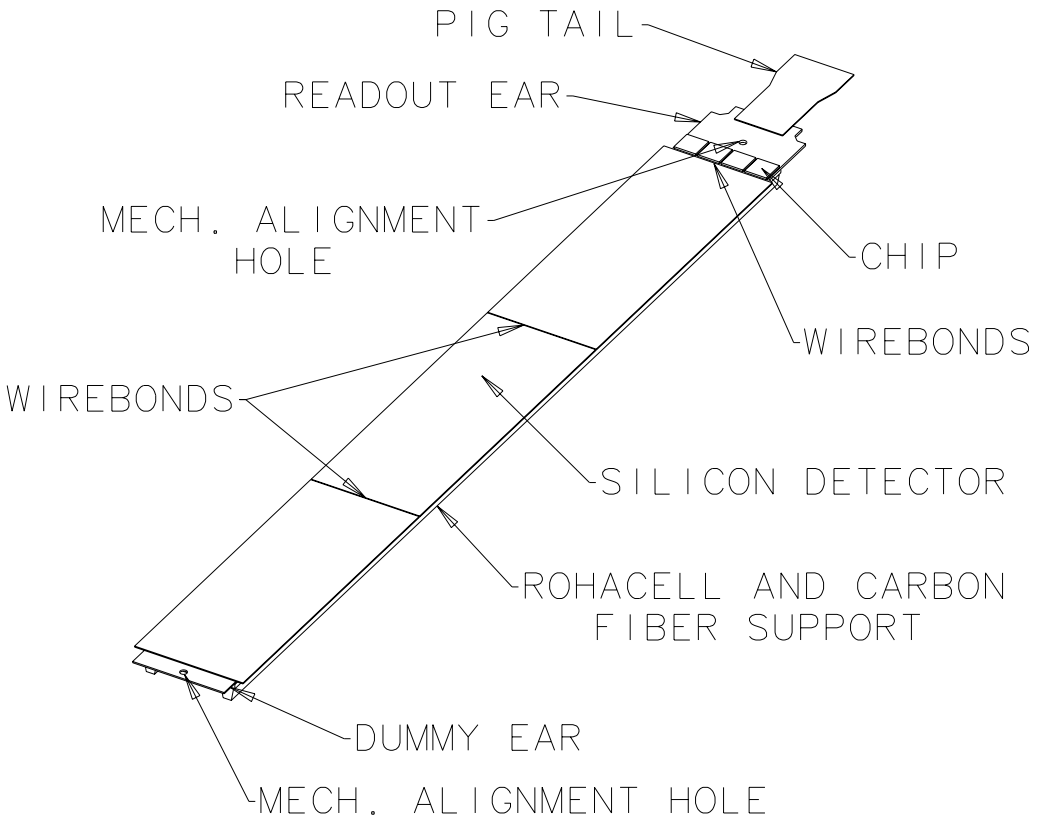

Figure 3.7: The SVX detector ladder, showing the three individual detector crystals and readout chips.

sured track parameters. Thus, the uncertainty in the track impact parameter, when SVX information is used, ranges from 50 μm for tracks with $P_T \approx 1$ GeV/c to 15 μm for tracks with $P_T \approx 10$ GeV/c. In this analysis, SVX helps to identify B-hadrons by discriminating the tracks coming from the vertices displaced from the primary interaction point.

The **vertex time projection chamber**, VTX, provides tracking information in the $r - z$ plane. It is divided into an east and a west half, each surrounding an SVX barrel. Each half of the VTX is composed of 28 octagonal modules which cover out to 22 cm in radius and to $|\eta| < 3.25$. The 18 chamber modules immediately surrounding the SVX contain 16 sense wires strung in the $r - \phi$ plane perpendicularly to a radial line extending from the origin. The remaining 10 modules have 24 sense wires and are located at larger z. The drift gap in the argon-ethane atmosphere is 4 cm. Adjacent modules are rotated by 11.3° in ϕ so that CTC $r - \phi$ track segments can be better matched to the VTX segments.

In this analysis the VTX information is used to provide a measurement of the z coordinate of the primary event vertex.

The **central tracking chamber** [36], CTC, is a cylindrical open-cell gas-filled drift chamber, which extends from outside the VTX to inside the solenoidal magnet covering a large part of the central pseudorapidity region $|\eta| < 1.1$. It has 84 sense wire layers arranged in nine superlayers. Five superlayers have wires aligned parallel to the beam axis. Between each pair of these axial superlayers there is a set of wires with a $\pm 3°$ tilt with respect to the beam axis to provide stereo information. Figure 3.8 shows a view of a CTC end plate. Hits on the CTC wires are matched to tracks and a fit is performed to measure all track parameters. Within each layer, groups of sense

Number of layers	84
Number of superlayers	9
Stereo angle for the superlayers	$0°$, $3°$, $0°$, $-3°$, $0°$, $3°$, $0°$, $-3°$, $0°$
Number of super cells per layer	30, 42, 48, 60, 72, 84, 96, 108, 120
Sense wire spacing	0.1 cm
Tilt angle	$45°$
Radius at innermost sense wire	30.9 cm
Radius at outermost sense wire	132.0 cm
Wire length	321.4 cm
Electric field	1350 V/cm
Magnetic field	14.1 KG
$r-\phi$ resolution	200 μm
$r-z$ resolution	0.6 cm
$\delta P_T/P_T$	$0.002 \times P_T$ (GeV/c)
Beam constrained $\delta P_T/P_T$	$0.0011 \times P_T$ (GeV/c)

Table 3.2: Summary of the CTC parameters.

wires and field shaping wires form cells which are tilted at $45°$ with respect to the radial direction. Table 3.2 lists the parameters associated with the CTC.

The CTC does not reconstruct tracks with $P_T < 200$ MeV/c. Its efficiency rises from 200 to 400 MeV/c and is uniform for tracks with $P_T > 400$ MeV/c [37, 38]. In this analysis particle momenta are derived from the CTC track parameters. Excellent momentum resolution is due to the large volume of the CTC and the magnetic field strength. Constrained fits (discussed later) are made in this analysis to further improve the momentum resolution. The CTC also gives a measurement of the ionization along its tracks, providing some information for particle identification based on ionization losses.

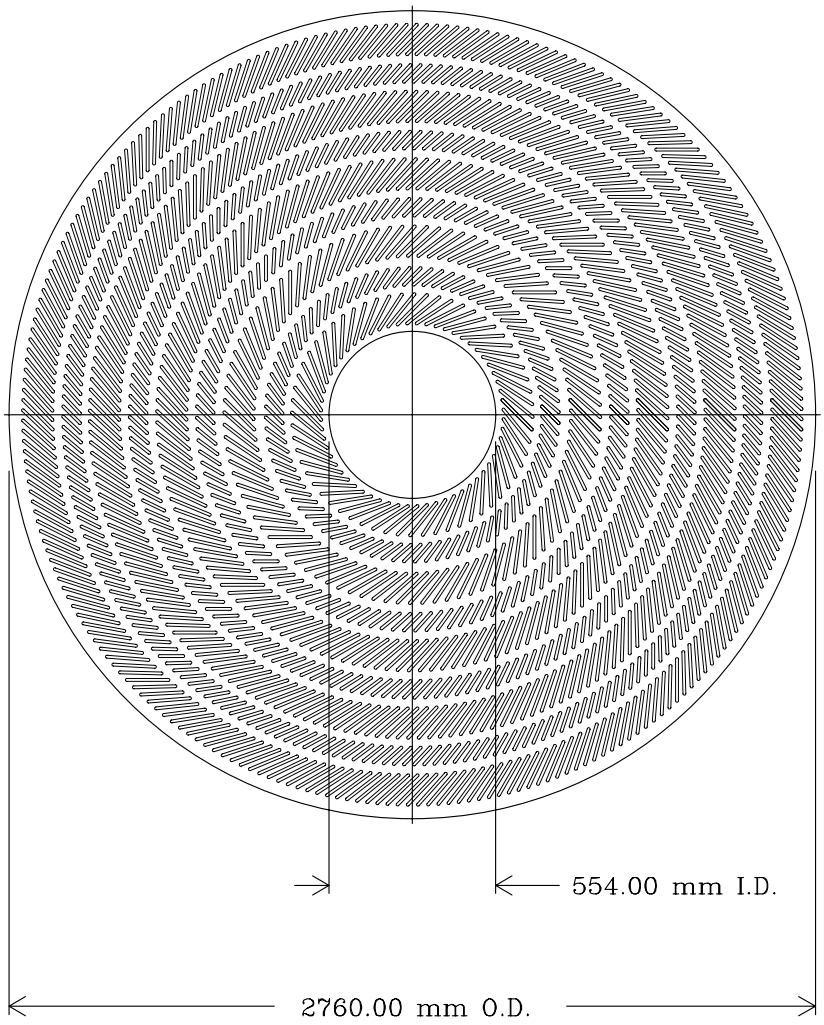

Figure 3.8: View of the CTC endplate showing the drift cells superlayer structure.

3.2.3 Muon Systems

The CDF muon system allows for the identification of muons. It consists of central and forward systems. The central system has three different detector subsystems, described below, each covering a different range of pseudorapidity.

The **central muon system** [39], CMU, provides muon identification and tracking out to $|\eta| \simeq 0.6$. The CMU system is divided at $\theta = 90^\circ$ into east and west half. In each half, the chambers are segmented into 24 wedges forming an approximate cylinder around the beamline. Each CMU wedge contains 48 drift cells, 226 cm in length, arranged along the z-axis. The arrangement of the drift cells within a chamber is shown in Figure 3.9 and that of the chambers within a calorimeter wedge in Figure 3.10. The total azimuthal coverage of the CMU system is approximately 85%. Timing information gives the $r-\phi$ position, charge division the $r-z$ position. These measurements can be compared to the position obtained by extrapolating a CTC track to improve muon identification and momentum measurement. The location of the muon chambers behind the central calorimeters introduces an effective cut-off of 1.4 GeV/c on the P_T of a detectable muon.

The **central muon upgrade system**, CMP, provides muon coverage behind additional steel shielding. The total amount of material traveled by a particle hitting the CMP amounts to about 8 absorption lengths. Only muons with P_T above 2.5 GeV/c are expected to reach the CMP. The percentage of real muons is higher when CMP confirmation is required for muon candidates registered in the CMU. In this analysis the CMP confirmation of a CMU hit is not required since the muons from J/ψ decays are rather soft

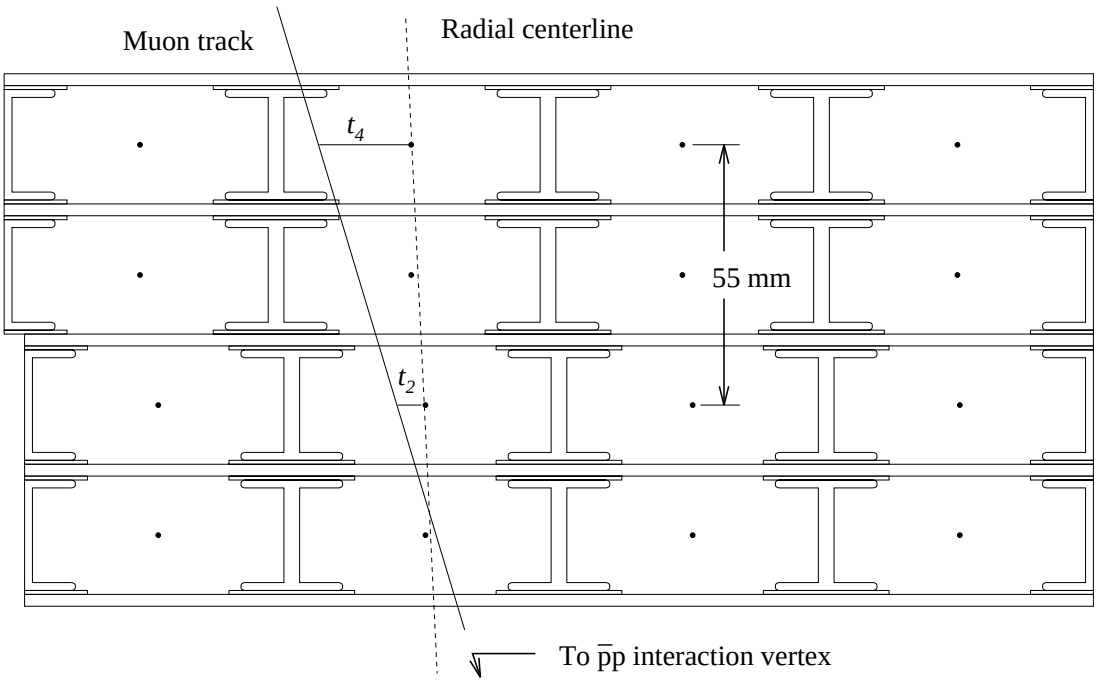

Figure 3.9: Arrangement of CMU drift cells, showing a muon track.

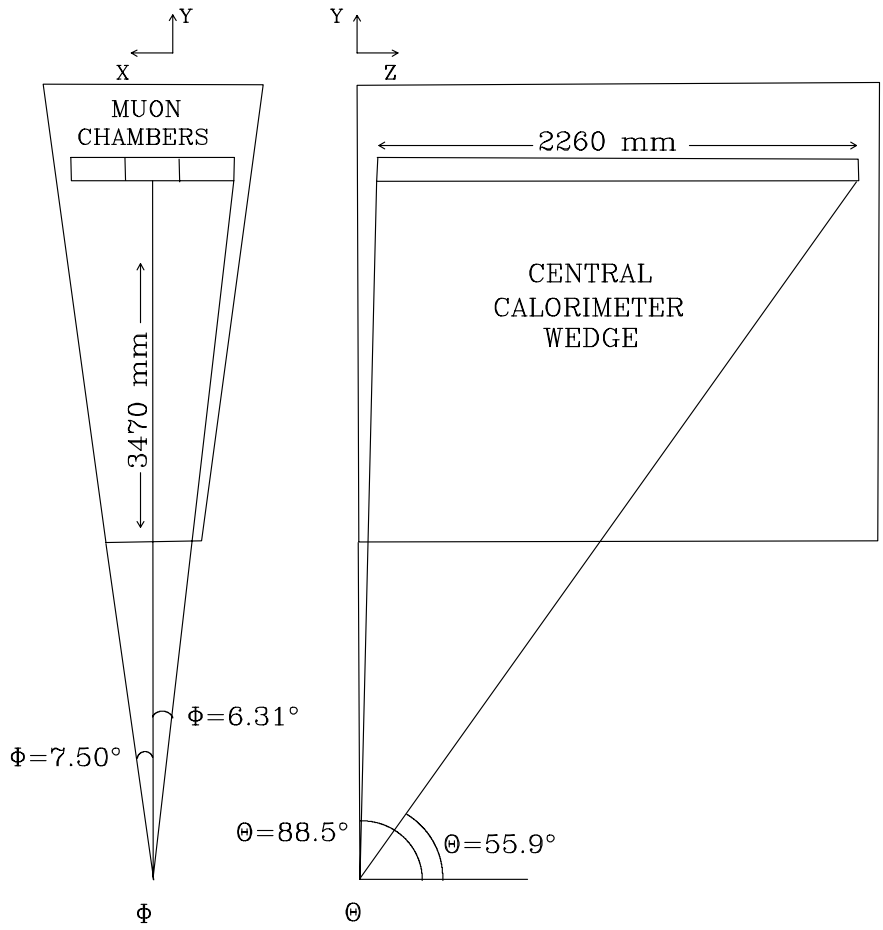

Figure 3.10: Location of central muon chambers within a calorimeter wedge.

and often have $P_T < 2.5$ GeV/c. The individual CMP chamber drift cells have the same size as the CMU cells, 63.5 mm $\times$ 26.8 mm in cross section, and are arranged along the z-axis, 320 cm long. Like the CMU, there are four layers of drift cells, and muon track stubs can be reconstructed in the transverse plane by measuring the drift times in all four layers. However, the charge deposited on the wires is not measured and no z information on the muon track is available from the CMP.

In general, the CMP chambers are used as confirmation for muon track stubs in the CMU chambers, both in the online and offline analyses. The addition of the CMP and its associated layer of steel was crucial in keeping the false trigger rate due to pion punch-trough down to a manageable level at high Tevatron luminosities.

The **central muon extension system**, CMX, covers the region $0.6 < |\eta| < 1.0$ and is located behind approximately 6 absorption lengths of calorimetry. The real μ to fake μ ratio in the CMX data is the worst among muon detectors and the trigger parameterization was not understood well enough to reproduce it in the Monte Carlo simulation. That gave us reason not to use CMX-triggered muons, which account for about 20% of registered J/ψ decays, in the cross section related measurements of this analysis.

3.2.4 Calorimetry

The CDF calorimetry system overview is given in Table 3.3. The pseudorapidity ranges are approximate and there are some overlapping regions near the edges of the components. The energy resolution consists of the two terms listed in the table, added in quadrature. The absorption thicknesses in the left column are in terms of radiation lengths for the electromag-

netic calorimeters (X_0), and pion absorption lengths for the hadronic ones (λ_0). The central electromagnetic calorimeter (CEM) consists of alternating layers of polystyrene scintillator and lead absorber. The central hadronic (CHA) calorimeter consists of steel and scintillator layers. The wall hadronic calorimeter (WHA) is designed to complete the η coverage of the CHA and is also made of steel and scintillator sandwich. Plug calorimeters (PEM and PHA) and forward calorimeters (FEM and FHA) are gas based.

Calorimetry was not used in this analysis other than to aid in muon identification by providing absorption layers.

Calorimeter	Coverage	Energy Resolution	Thickness
CEM	$0.0 < \|\eta\| < 1.1$	$13.7\%/\sqrt{E} \oplus 2\%$	18 X_0
PEM	$1.2 < \|\eta\| < 2.4$	$22\%/\sqrt{E} \oplus 2\%$	18-21 X_0
FEM	$2.4 < \|\eta\| < 4.2$	$26\%/\sqrt{E} \oplus 2\%$	18 X_0
CHA	$0.0 < \|\eta\| < 0.9$	$50\%/\sqrt{E} \oplus 3\%$	4.5 λ_0
WHA	$0.7 < \|\eta\| < 1.3$	$75\%/\sqrt{E} \oplus 4\%$	4.5 λ_0
PHA	$1.3 < \|\eta\| < 2.4$	$106\%/\sqrt{E} \oplus 4\%$	5.7 λ_0
FHA	$2.4 < \|\eta\| < 4.2$	$137\%/\sqrt{E} \oplus 4\%$	7.7 λ_0

Table 3.3: Summary of the CDF calorimetry components.

3.2.5 Trigger

This analysis relies on the ability to trigger effectively on events of interest. The total $\bar{p}p$ interaction cross section is about 80 mb [40], which is orders of magnitude larger than the cross section of a typical hard collision process. This fact drives interaction rates and beam intensities higher, in order to generate more rare events. However, it is impossible to record all the data produced in all the $\bar{p}p$ collisions. At CDF in Run I the collision rate is 300,000 Hz while the detector data can be recorded at a rate of 5 Hz. The on-line event

selection process at CDF is accomplished with a three-stage trigger system. The multi-stage structure minimizes deadtime by using fast, relatively simple triggers to filter events for slower, more complicated ones. For this analysis we use triggers designed to identify events containing a $J/\psi \rightarrow \mu^+\mu^-$ decay.

Detector elements are attached to front-end electronics which send signals to digitization modules for assembly into a CDF event record. The front end electronics include FASTBUS TDCs (Time to Digital Converter) to read out tracking and prompt muon data. These fast signals are used in the trigger decision. Other front-end modules, called RABBIT cards, are mounted on the detector and are used to read out calorimeter and muon chamber information. These front end systems are connected to digitization modules which do some processing such as formatting and adding header information. The data are then collected by an event builder which sorts them at a rate of $\sim$ 30 Hz. The average size of an event assembled by the event builder is about 200 kB. After passing it the data are submitted to a Level 3 trigger and events are logged onto 8 mm tape at a rate of $\sim$ 5 Hz.

The **Level 1** trigger reduces the incoming 300 kHz event rate to 1 kHz. It makes a decision every beam crossing, or every 3.5 μs. Only the most elementary comparisons are possible at this rate. The low-P_T dimuon trigger requires two "bronze" muons, meaning the Level 1 electronics found two muon track segments with P_T larger than 3.3 GeV/c. For most of run 1A one of the muon segments had to be a CMU type muon because backgrounds in the CMX chambers caused too high a Level 1 rate. The later run 1A and run 1B data did allow two CMX muons to initiate the trigger. The Level 1 trigger efficiency has been studied [41] and the results are used in this analysis with the Monte Carlo simulation.

The **Level 2** trigger filters events to a rate of 12 Hz by removing backgrounds which pass Level 1 and making requirements for better defined thresholds. For low-P_T dimuon triggers the requirement is that one of the muons stubs is matched to a CFT found track. CFT, or Central Fast Tracker [42], makes use of fast hit information from the five axial superlayers in the CTC.

For run 1A, the efficiency of the trigger was determined [41] by studying how often the second leg of J/ψ decays was matched to a CFT track, when the first one was responsible for the trigger. For run 1B Level 2 trigger conditions were changed, requiring both muons to be matched with a CFT track [43]. Accordingly, this analysis is using different muons P_T cuts for run 1A and run 1B data, as described later, as well as different trigger conditions for Monte Carlo when simulating run 1A and run 1B data.

The **Level 3** trigger consists of a software processor farm. When Level 2 accepts an event, the event data are packaged and sent to one of 48 Silicon Graphics computers which process them in a manner similar to the offline reconstruction, reducing the event rate to 5 Hz for data logging. During this reconstruction some of the applied conditions are:

- matching between muon stubs and CTC tracks within 4σ
- muon transverse momentum $P_T > 1.4$ GeV/c
- two muons have opposite charges
- dimuon invariant mass $2.8 < M_{\mu^+\mu^-} < 3.4$ GeV/c^2

Chapter 4

Data Set

This chapter describes the data set used for the analysis. CDF has recorded about 110 pb^{-1} of data during the Tevatron Collider Run I. These data contain more than 700,000 events with J/ψ candidates which passed the J/ψ trigger requirements. The invariant mass distribution for the J/ψ candidates passing the trigger is shown in Figure 4.1.

4.1 Offline Production

The raw events, written on tapes, are processed off-line and stored on disk in a compact format without keeping raw detector data. The production of the event files takes the raw detector information and calculates higher-level quantities. For example, digitized wire hits in the tracking and muon systems are converted into momenta, CTC-muon matching variables, vertices, and so on. Pattern recognition of CTC hits is performed and fitting is done to calculate the five track parameters for the identified tracks. These higher level quantities are accessed by the analysis to calculate the physics quantities of interest.

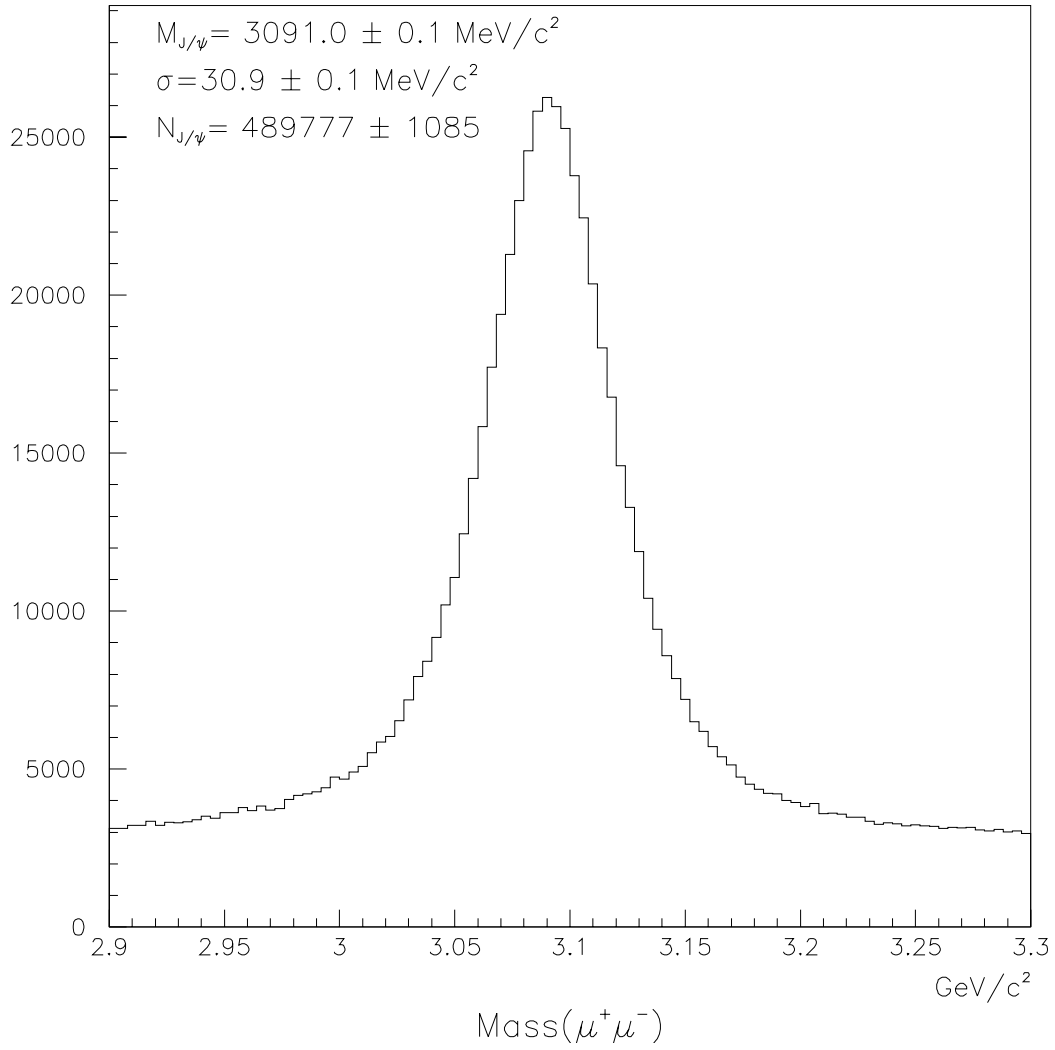

Figure 4.1: The $\mu^+\mu^-$ invariant mass reconstructed without vertex constraining the muon tracks.

4.2 J/ψ Selection

When reconstructing the J/ψ decays in this analysis, we always require the muons to originate from a common vertex. This requirement reduces the errors on the track parameters and improves the J/ψ mass resolution. The $\mu^+\mu^-$ invariant mass distribution shown in Figure 4.1 was obtained without such a requirement, and Figure 4.2 shows the $\mu^+\mu^-$ invariant mass after the vertex constraint. The procedure of geometric and kinematic fitting is described in greater detail in Section 5.2.

Additional selection criteria on muon candidates which pass the J/ψ trigger, can be applied to improve the signal-to-noise ratio for the J/ψ candidates. They involve making requirements on the P_T of the muon candidate and matching between the CTC track and the muon chamber stub. Muon backgrounds arising from hadronic punch-through, decay-in-flight (real muons), muon chamber noise, and back-scattered particles are less likely to have CTC tracks well-matched to the hits in the muon chambers. These backgrounds also tend to have lower P_T tracks matched to the hits. Figure 4.3 shows the transverse momentum distribution for μ candidates in the J/ψ signal region and sideband regions from run 1A data. For the purpose of optimizing the J/ψ selection cuts, the signal region is defined as the $\pm 3\sigma$ window around the world average J/ψ mass of 3096.88 ± 0.04 MeV/c^2 [8], where σ is the uncertainty on the measured J/ψ mass. The sideband regions are those outside the $\pm 4\sigma$ window. The distributions are separated by muon detector type. The sharp edge at 1.4 GeV/c is due to the reconstruction code which will not match muon hits to low momentum tracks since muons with $P_T < 1.4$ GeV/c on average will not traverse the calorimeter absorber. The edge at 2.5 GeV/c

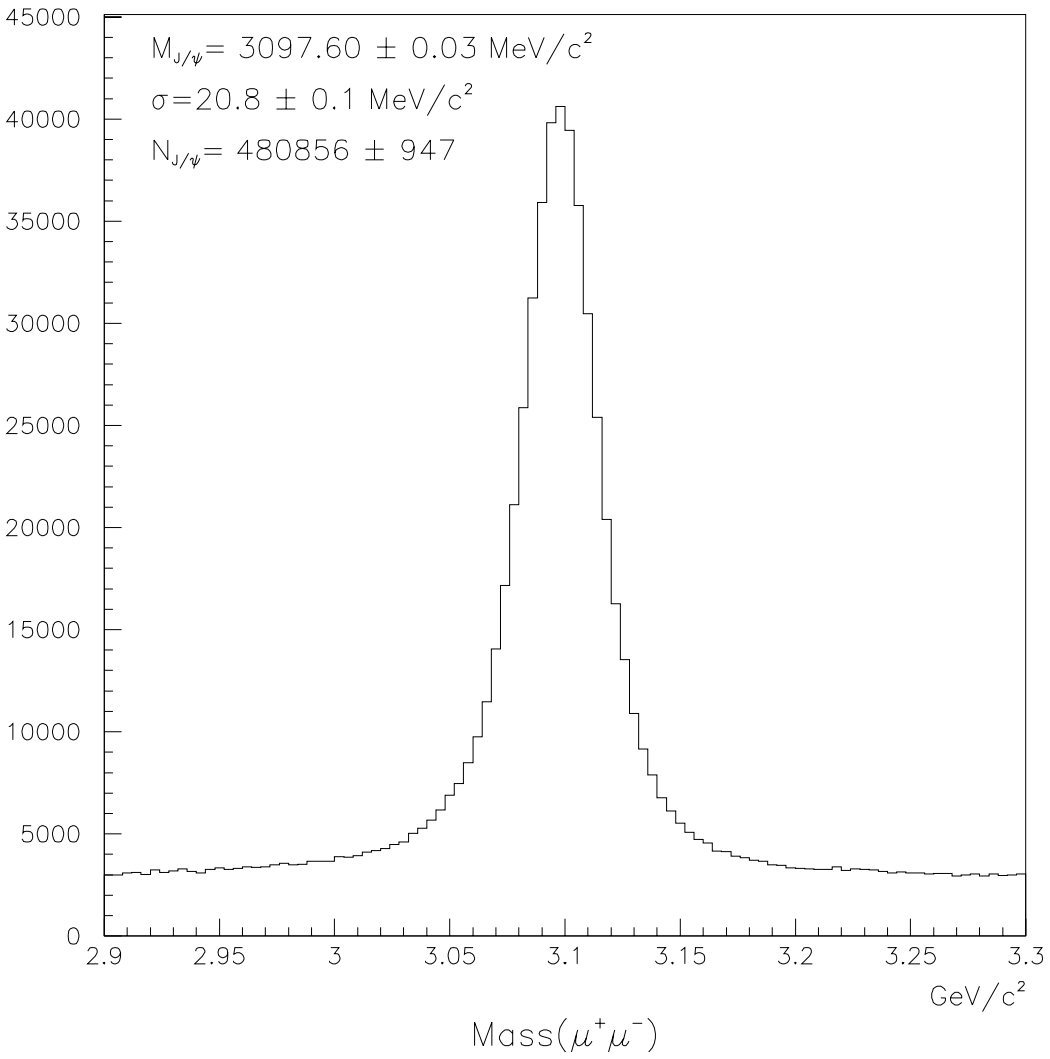

Figure 4.2: The $\mu^+\mu^-$ invariant mass distribution showing the J/ψ candidates after vertex constraining the muon tracks.

is an artifact of Level 2 trigger, which requires one of the J/ψ muon legs to be found by the CFT, which becomes efficient around 2.5 GeV/c. For the CMP, only muons with P_T higher than about 2.5 GeV/c are expected to pass trough the 8 absorption lengths of calorimeter. Figure 4.4 shows the same distributions from run 1B data demonstrating the differences in trigger requirements for that period of data taking.

For the analysis of run 1A data both muons are required to have a P_T higher than 1.8 GeV/c and at least one muon to have a P_T higher than 2.8 GeV/c; for the run 1B data both muons are required to have transverse momenta above 2.0 GeV/c. Figure 4.5 presents the invariant mass distribution of J/ψ candidates after applying the above requirements.

The J/ψ background is reduced by applying selection criteria on the quality of the match between the hits in the muon chamber and the extrapolated track in the CTC. For real muons, the uncertainty in extrapolating the CTC track to the muon chambers is dominated by multiple scattering within the calorimeter. This uncertainty is described by Equation 4.1 [44], which takes into account the CDF geometry.

$$\sigma_x \approx \frac{13.8}{P_T}\sqrt{\frac{0.59 + 0.41/\sin\theta}{1 - 0.71/P_T}} \quad \text{(cm)} \tag{4.1}$$

where P_T units are GeV/c. The typical uncertainty is such that a 3 GeV/c muon's track is expected to be extrapolated to within about 5 cm of the muon hits in the muon chambers. A χ^2 is formed by dividing the extrapolation distance by the multiple scattering uncertainty. This is done in the x coordinate except for the CMU where a χ^2 is calculated also in the z coordinate. Figure 4.6 shows these χ^2 distributions for the J/ψ signal and sideband regions. In this analysis we require matching within three standard deviations for x

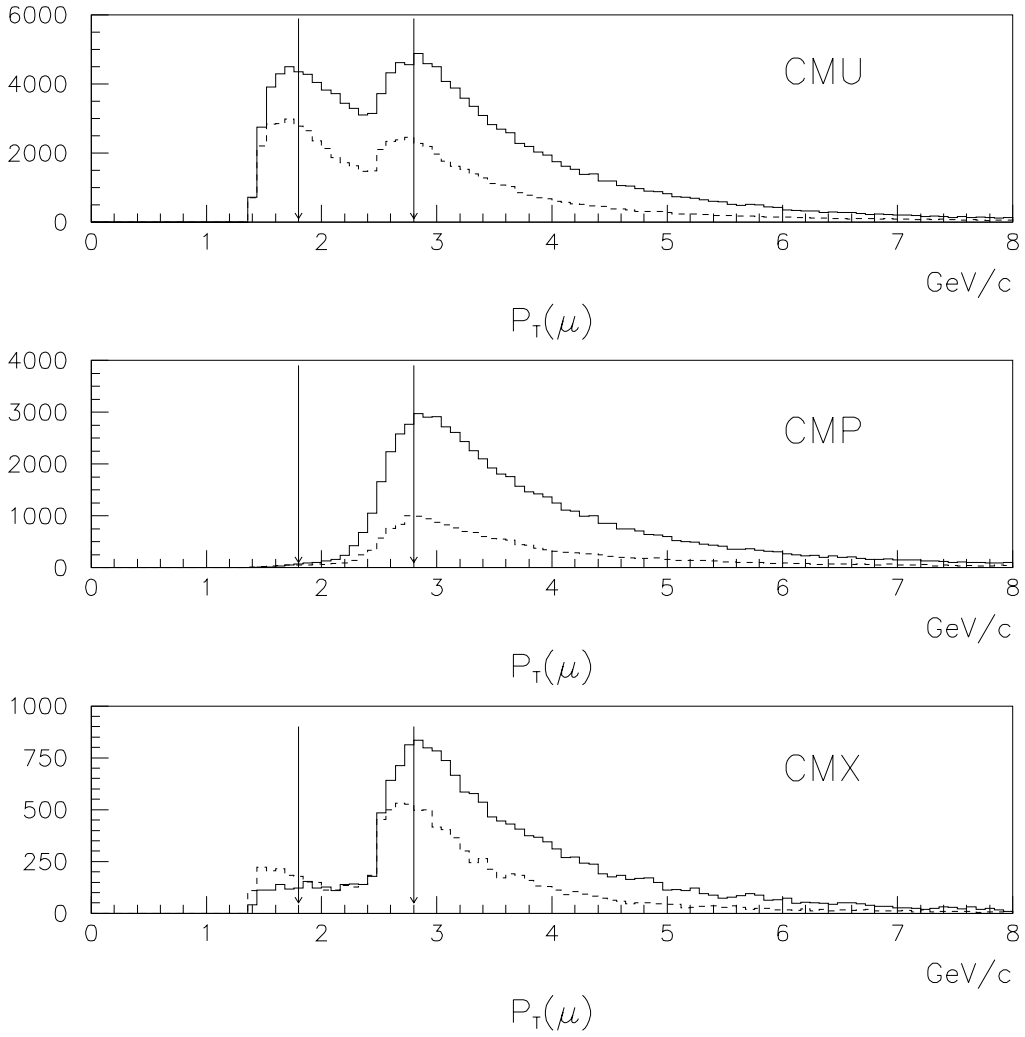

Figure 4.3: The P_T distribution of the muon candidates for the J/ψ signal region (solid) and sidebands regions (dashed) divided by the muon detector subsystem in Run 1A. Arrows show the values of the P_T cuts on the muon candidates.

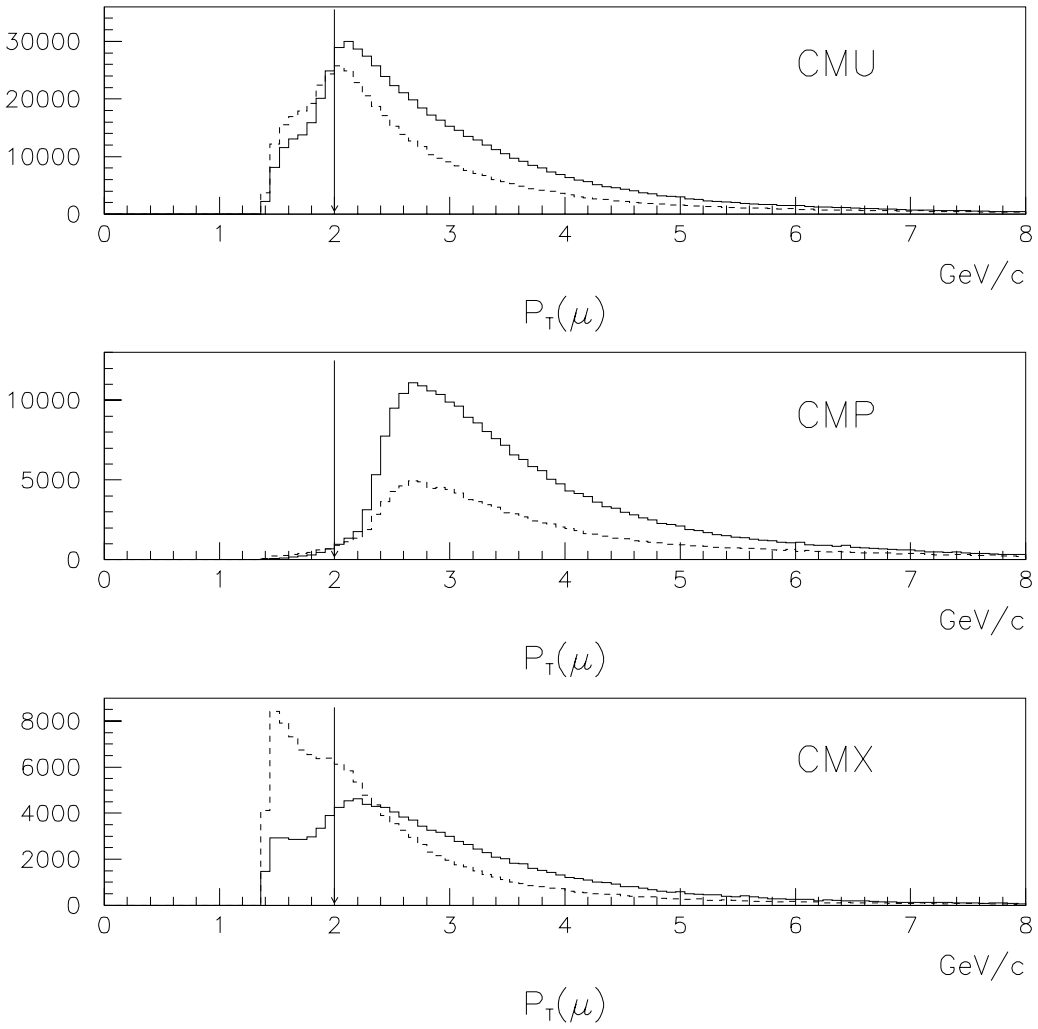

Figure 4.4: The P_T distribution of the muon candidates for the J/ψ signal region (solid) and sidebands regions (dashed) divided by the muon detector subsystem in Run 1B. Arrows show the value of the P_T cut on the muon candidates.

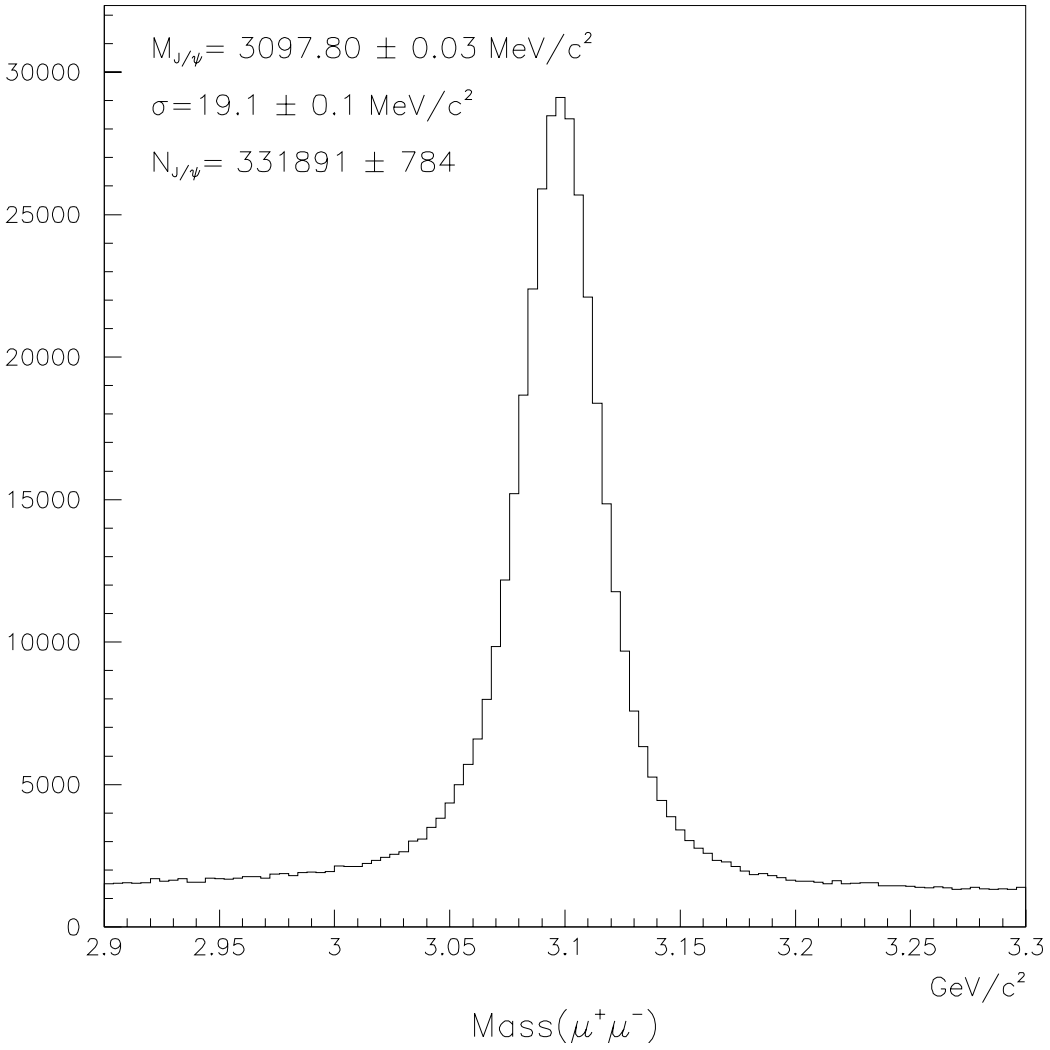

Figure 4.5: The $\mu^+\mu^-$ invariant mass distribution after the P_T cuts on the muon candidates discussed in the text; Run 1A and 1B data shown.

components and 3.5 standard deviations for CMU z component. Figure 4.7 shows the J/ψ invariant mass distribution after applying the "matching" requirements.

The signal-to-noise ratio in the J/ψ sample is rather high. This allows us to choose a wide mass window for the J/ψ candidates selection for the further analysis. Therefore, the measured dimuon mass is required to be within four standard deviations (calculated using the mass uncertainty of the event) of the world average. An alternative approach of selecting a fixed size mass window would be more simple, but it has one shortcoming: there are two tracking devices in CDF, CTC and SVX, with different momentum resolutions. This translates into different mass resolutions for the dimuons measured in the different detectors. The mass resolution varies from 15.28 MeV/c^2 for the J/ψ candidates which have both muons measured in the SVX to 26.38 MeV/c^2 for the J/ψ candidates which have only CTC information (Figure 4.8). In this analysis we use the SVX data when it is available and the CTC data otherwise. Thus, selecting the fixed J/ψ mass window would not provide the best signal-to-noise ratio for the final sample of the J/ψ candidates measured in both CTC and SVX detectors.

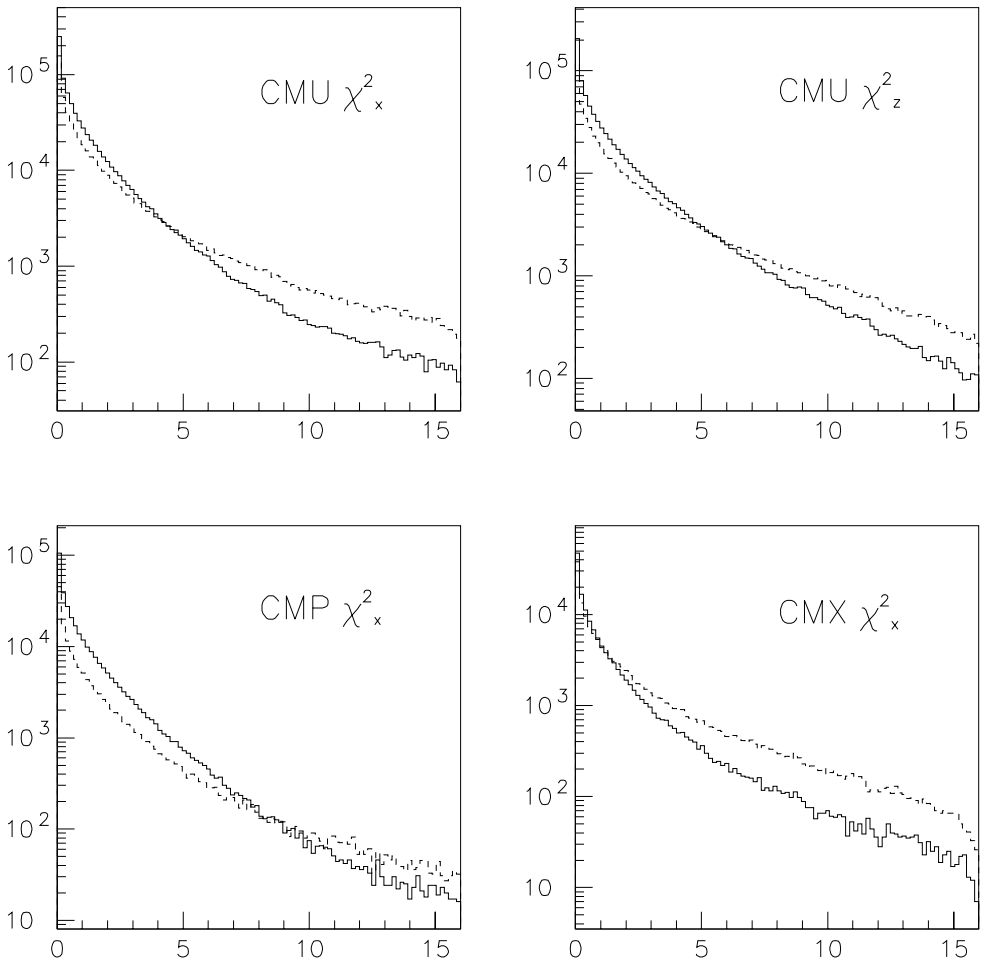

Figure 4.6: χ^2 distributions for matching between CTC tracks and muon stubs in the J/ψ signal region (solid) and sidebands (dashed) for each muon detector subsystem.

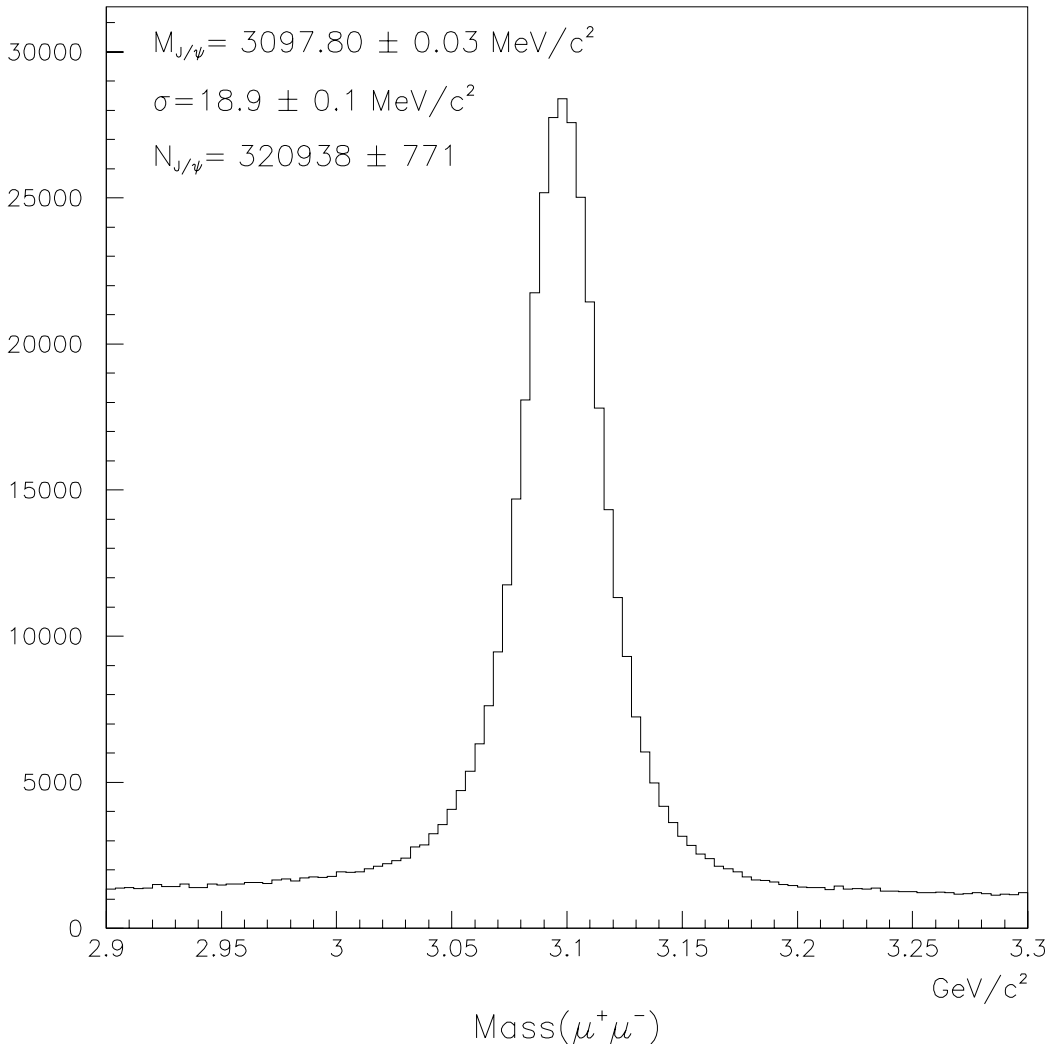

Figure 4.7: The $\mu^+\mu^-$ invariant mass distribution after making P_T cuts on muon candidates and requiring their CTC track and muon chamber stub to match. Run 1A and 1B data are shown.

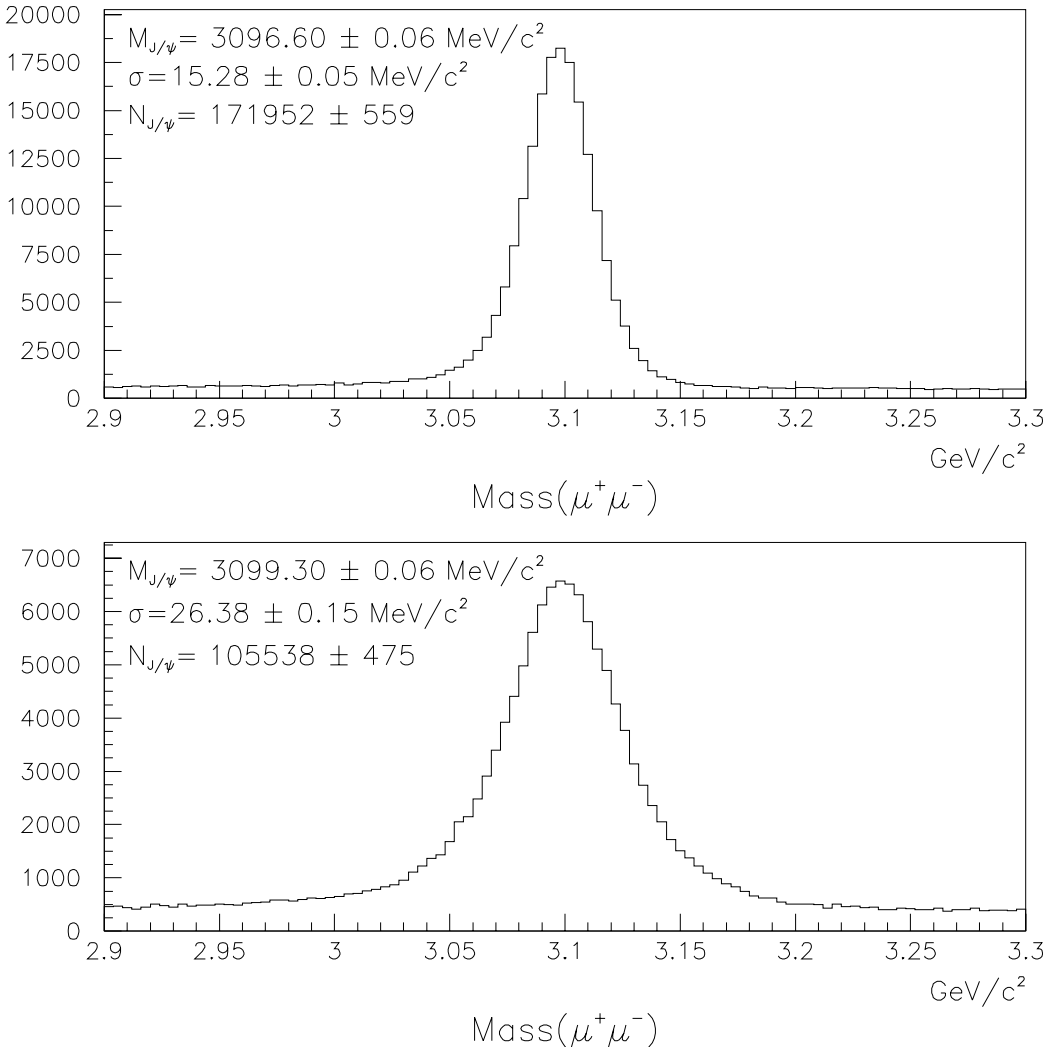

Figure 4.8: The $\mu^+\mu^-$ invariant mass distributions when both muons are measured in the SVX (top) and CTC (bottom); Run 1A and 1B data are shown together.

Chapter 5

Search for $\Lambda_b^0 \to J/\psi\,\Lambda(1520)$

The topology of the decay chain $\Lambda_b^0 \to J/\psi\,\Lambda(1520)$, $J/\psi \to \mu^+\,\mu^-$, $\Lambda(1520) \to p\,K$ in the plane transverse to the proton beam is shown in the Figure 5.1. We use only the decay modes into charged particles in order to be able to use the tracking system to obtain a good mass resolution. References to a specific charge state include also the charge conjugate state, unless explicitly stated otherwise. The distinctive feature of a B-hadron decay is that given the relatively high value of the b lifetime, the decay vertex is displaced from the primary vertex. This makes it possible to distinguish the Λ_b decays from backgrounds coming from the primary interaction vertex. Both Λ_b decay products, J/ψ and $\Lambda(1520)$, are short-lived, the J/ψ width being 87 ± 5 keV and the $\Lambda(1520)$ width being 15.6 ± 1.0 MeV. That makes the final decay particles, μ^+, μ^-, p, and K appear to come from the same vertex. These decay features suggest the reconstruction strategy described in this chapter.

The decay of the B-meson, $B^0 \to J/\psi\,K^*$ has the same topology as the $\Lambda_b^0 \to J/\psi\Lambda(1520)$ decay with the only exception that the final products are μ^+, μ^-, π, and K. We reconstruct both $\Lambda_b^0 \to J/\psi\Lambda(1520)$ and $B^0 \to J/\psi\,K^*$

decays, using the $B^0 \to J/\psi\, K^*$ for monitoring purposes and for the further cross-section related calculations described in the next chapter.

5.1 Track Selection

To reduce the combinatorial background and improve the mass resolution, we apply selection criteria to the reconstructed tracks. These criteria generally require the track to be well-measured in the CTC and the match between SVX and CTC track segments to be good.

5.2 Constrained Fits

In the course of the analysis we subject the track parameters to several geometrical and kinematic constraints to improve the mass resolution [45]. The idea of kinematic fitting is to reduce the measurement errors by applying known physical constraints. A first possible requirement is that the daughter tracks from a single decay must all come from the same vertex, such as in $J/\psi \to \mu^+\,\mu^-$ decay. Moreover, some combination of decay daughters must have a particular invariant mass. In the decay chain $\Lambda_b^0 \to J/\psi\,\Lambda(1520)$, $J/\psi \to \mu^+\,\mu^-$, $\Lambda(1520) \to p\,K$, the invariant mass of the two muons can be constrained to the known J/ψ mass. Finally, if the Λ_b^0 in the example above is produced at the primary vertex and decays at a secondary vertex, we may further require that the sum of the momenta of the decay products point away from the primary vertex. The fitting procedure involves an adjustment of the track parameters by imposing constraints to minimize the χ^2 calculated from the change in parameters with respect to their errors. The result of

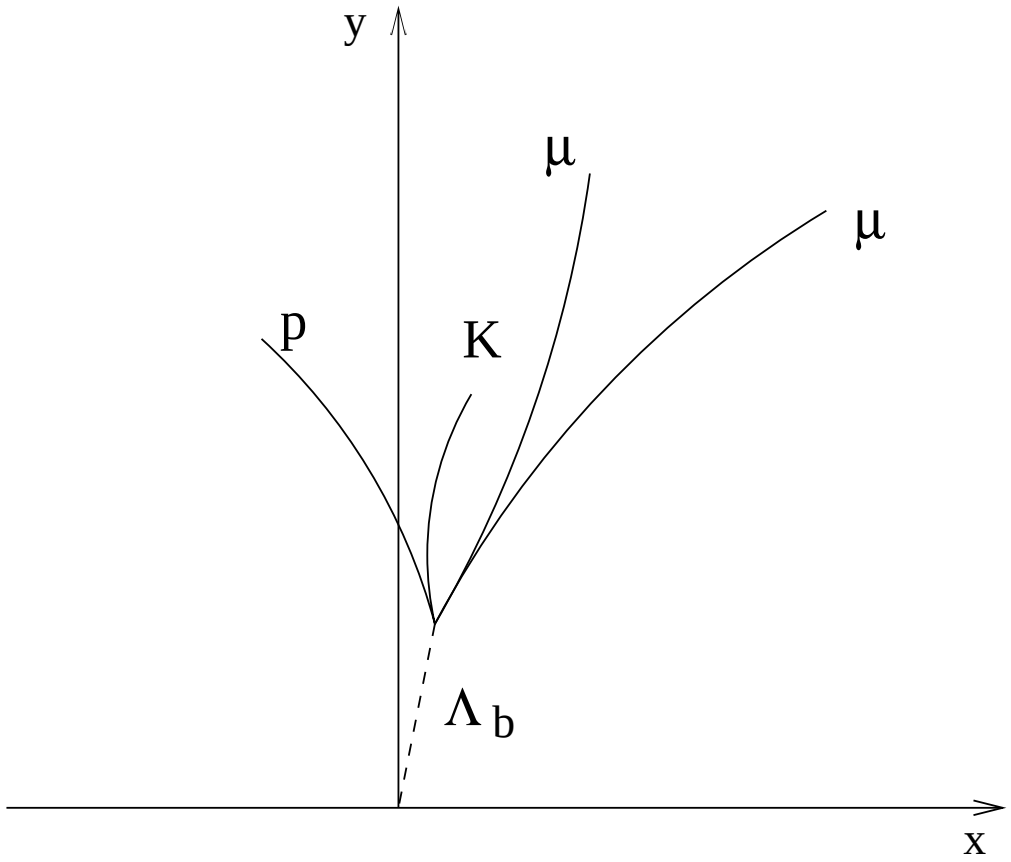

Figure 5.1: The transverse $\Lambda_b^0 \to J/\psi\Lambda(1520)$ event topology.

the constrained fit is a new set of track parameters and a corresponding new covariance matrix. For tracks that did not come from the same vertex the attempt to constrain the track parameters to have a common vertex results in a large χ^2 which can be used to distinguish this set of tracks from those which have higher probability of originating from a common vertex. Similar procedures are used for the mass and pointing constraints.

5.3 P_T Scale

The transverse momentum scale is used to convert a measured track curvature into a transverse momentum according to:

$$P_T(\mathrm{GeV}/c) = 1.5 \times 10^{-4} B(\mathrm{kG})/C(\mathrm{cm})$$

where B is the magnetic field and C is the curvature of the track. The P_T scale therefore depends on the magnetic field intensity which has a default value of 14.116 kG in the offline reconstruction program. This value is based on measurements made with 5000 A current in the solenoid and extrapolating the measurement to the operating level of 4650 A. The accuracy of the magnetic field measurement is 0.05% [46] at 5000 A.

In addition to the magnetic field, the P_T scale also depends on corrections to the measured curvature due to energy losses experienced by the particle passing through material such as beam pipe, SVX, cables, supports, inner wall of the CTC, and the CTC gas and wires. This correction can be applied as an average correction since the actual energy loss of a particle is not known. The correction depends on the particle's type and velocity, and on the amount and type of the material traversed.

We have also adjusted the scale factor for the magnetic field by requiring the reconstructed J/ψ mass to match the world average value. Thus, the average values of the magnetic field we use are 14.12598 kG for Run 1A data and 14.12427 kG for Run 1B data. The magnetic field value is monitored in CDF using nuclear magnetic resonance devices in Run 1B and by measuring the magnet current in Run 1A. We found that fluctuations in the field strength do exist. We correct for these fluctuations by reading out the measured magnetic field values and scaling the average field value on an event by event basis if the fluctuation is less than 0.3% of the nominal field value. If the field fluctuation is higher than 0.3% (which is an extremely rare case) we discard the event. The mass resolution for the J/ψ measured in the SVX is 15.28 ± 0.05 MeV/c^2 after the magnetic field correction and 15.57 ± 0.05 MeV/c^2 without the field correction.

5.4 $\Lambda_b^0 \to J/\psi\Lambda(1520)$ Decay Reconstruction

5.4.1 $\Lambda(1520)$ and K^* Candidate Selection

After the J/ψ is identified (see Chapter 4) all the remaining tracks in the event are combined in oppositely charged pairs and their invariant mass is tested for consistency with the $\Lambda(1520)$. Even tracks identified as muons participate here, as there is a fraction of hadrons mistakenly tagged as muons. Each pair of tracks is constrained to a common vertex and if the χ^2 probability for the two tracks to come from the same vertex is greater than 1% the invariant mass is calculated. Each pair of tracks gets both mass assignments of the $\Lambda(1520)$ daughters ($p--K$ and $K--p$) resulting in two possible candidates out of each pair. Only the assignment resulting in the invariant mass closer

to the $\Lambda(1520)$ world average mass is kept. A Monte Carlo study shows that the misidentification rate for this method is only about 5%.

We do not observe a $\Lambda(1520)$ signal enhancement over the combinatorial background, since the latter is extremely high, so we identify a pair of tracks as a $\Lambda(1520)$ candidate if their invariant mass is between 1504 and 1535 MeV/c^2. This corresponds to a window of two natural widths (, = 15.5 MeV) around the pole for $\Lambda(1520)$ ($M(\Lambda(1520)) = 1519.5 \pm 1.0$ MeV/c^2).

The same procedure is followed to select the K^* candidates from the $B^0 \rightarrow J/\psi K^*$ decay. The K^* signal is also not distinguished from the combinatorial background in our data too. The mass window to identify the K^* candidates is taken to be between 842 and 940 MeV/c^2 (for the K^*, , = 49.8 MeV and $M(K^*) = 891.59 \pm 0.24$ MeV/c^2).

5.4.2 Λ_b^0 and B^0 Candidates

In order to select Λ_b^0 candidates, the J/ψ and $\Lambda(1520)$ candidates are tested for a common vertex with a χ^2 probability greater than 1%. The track parameters of the four-particle system passing this test are recalculated, requiring simultaneously the two muons to have the J/ψ mass, the four tracks to have a common vertex, and the total momentum of the four particles to point to the primary vertex. If the combined χ^2 probability of this constrained fit is greater than 1%, the invariant mass of the system is calculated and if it falls within a search window between 5500 and 5800 MeV/c^2, we consider the event a Λ_b^0 candidate. The B^0 candidates are selected according to the same strategy with a mass window between 5150 and 5450 MeV/c^2. The invariant mass distribution of the Λ_b^0 candidates is shown in the top plot of Figure 5.2. The bottom plot shows the invariant mass distribution of the B^0 candidates.

The bin width is 5 MeV/c^2 for this and all the following Λ_b^0 and B^0 plots. It is evident that further actions are required to reduce the combinatorial backgrounds.

5.5 Cut Optimization

The expected Λ_b^0 signal is very small and care must be taken to ensure that the analysis cuts do not enhance a background fluctuation. Rather than tuning cuts on the signal, the specific requirements for $\Lambda_b^0 \to J/\psi\Lambda(1520)$ are based on the optimization of signal-to-noise ratio for $B^0 \to J/\psi K^*$ decay along with Monte Carlo studies. In a counting experiment, the statistical error on a signal S is $\sqrt{S+B}$, where B is the background. Maximal significance is therefore achieved when $S^2/(S+B)$ is maximized. Our intention is also to use as few cuts as possible.

5.5.1 Additional Tracking Selection and $c\tau$ Cut

The average lifetime of the Λ_b^0 is 1.14 ± 0.08 ps [8] and that of the B^0 meson is 1.56 ± 0.06 ps [8]. This translates into decay lengths of the order of 400 and 500 μm respectively for transverse momenta of the order of 10 GeV/c. These decay lengths are large compared with the expected resolution using the SVX and comparable to the expected resolution using the CTC information. The signal is therefore expected to have a measurable proper lifetime distribution which is distinguishable from the lifetime of the combinatorial background. Therefore, to reject the combinatorial background coming from prompt tracks we apply a $c\tau$ cut. Table 5.1 lists the signal and background behavior for the B^0 invariant mass distribution when different

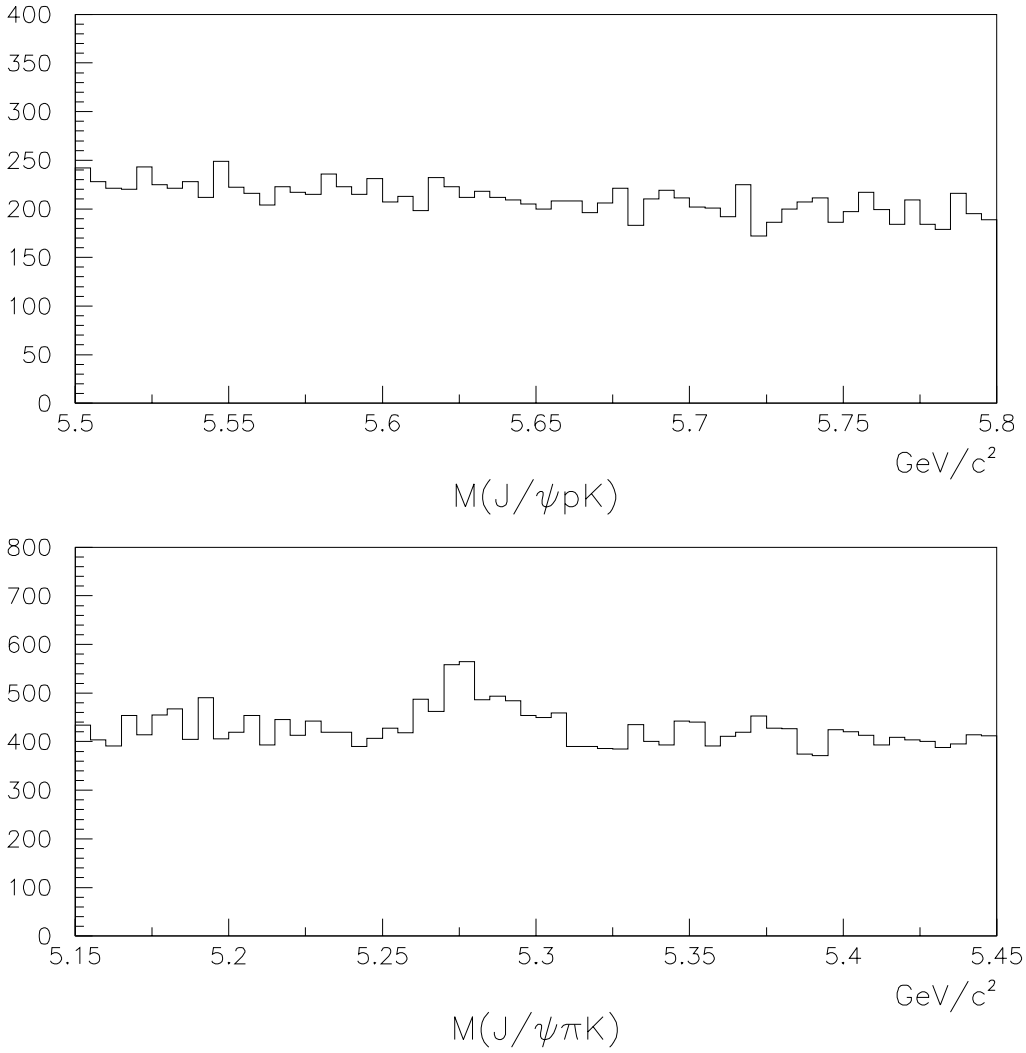

Figure 5.2: The J/ψ–p–K (top) and J/ψ–K–π (bottom) invariant masses after applying the selection procedure discussed in section 5.4.

numbers of tracks in the $B^0 \to J/\psi\, K^*$ decay are required to have the SVX information. WE consider a track to be an SVX-measured, it it has at least three hits in the SVX detector. Since the case when at least two tracks are measured in the SVX has the best signal-to-noise ratio for the $B^0 \to J/\psi\, K^*$, we will require a minimum of two SVX-measured tracks for $\Lambda_b^0 \to J/\psi\, \Lambda(1520)$ and $B^0 \to J/\psi\, K^*$ decay products.

Minimum number of SVX Tracks Required	0	1	2	3	4
Signal	392	278	270	261	199
Background	499	143	99	87	40
$S^2/(S+B)$	172	183	198	196	165

Table 5.1: Signal and background for different numbers of tracks with SVX information for the $B^0 \to J/\psi K^*$ decay after all other cuts described in sections 5.5.1 and 5.5.2 have been applied.

$c\tau$ Cut Value, μm	N/A	0	50	100	150	200
Signal	352	305	281	270	237	217
Background	1037	564	193	99	65	50
$S^2/(S+B)$	89	107	167	198	186	176

Table 5.2: Signal and background for the different values of the $c\tau$ cut for $B^0 \to J/\psi K^*$ all other cuts described in sections 5.5.1 and 5.5.2 have been applied.

The $c\tau$ is calculated in the transverse plane according to the formula:

$$c\tau = \frac{(P_x \cdot L_x + P_y \cdot L_y) M_b}{P_T^2}$$

where P_x and P_y are the momentum components of the decaying object, $P_T^2 = P_x^2 + P_y^2$, M_b is the object's mass, and L_x and L_y are the x and y projections of

the distance from the primary vertex to the decay vertex. Table 5.2 lists the number of signal and background events for the B^0 after applying different $c\tau$ cuts. The statistical significance is highest for a 100 μm cut. The recent CDF measurement [48] finds the Λ_b^0 lifetime only 15% shorter than the lifetime of the B^0 which gives us a reason to choose a 100 μm cut for both Λ_b^0 and B^0 for simplicity and consistency. Figure 5.3 shows the invariant mass distributions for Λ_b^0 and B^0 after requiring two tracks to have SVX information and the proper lifetime to be above 100 μm. The arrows on the Λ_b^0 plot mark the area where we expect to see the mass peak. The B^0 invariant mass distribution is shown together with the result of a binned likelihood fit.

5.5.2 Kinematics Cuts

In order to further reduce the combinatorial background, which consists mostly of low-momentum tracks, we apply P_T cuts on the Λ_b^0/B^0 and $\Lambda(1520)/K^*$ candidates. Figure 5.4 presents the P_T spectra of the Monte Carlo simulated Λ_b^0 and $\Lambda(1520)$ (solid) and the P_T spectra of Λ_b^0 and $\Lambda(1520)$ candidates (shown in Figure 5.3) after performing the selection requirements described earlier in this chapter. Here we can see that selecting Λ_b^0 candidates with transverse momenta above 6 GeV/c is almost harmless for the signal while removing some fraction of the background. By requiring the transverse momentum of the $\Lambda(1520)$ to be greater than 2 GeV/c we remove a significant amount of the background and preserve a large portion of the signal. The result of applying several different P_T cuts on the B^0 candidates is shown in the Table 5.3. We choose $P_T(\Lambda_b^0\, B^0) > 5.0$ GeV/c and $P_T(\Lambda(1520)\, K^*) > 2.0$ GeV/c as being the most efficient in terms of signal-to-noise ratio. The results of these P_T cuts are shown in Figure 5.5.

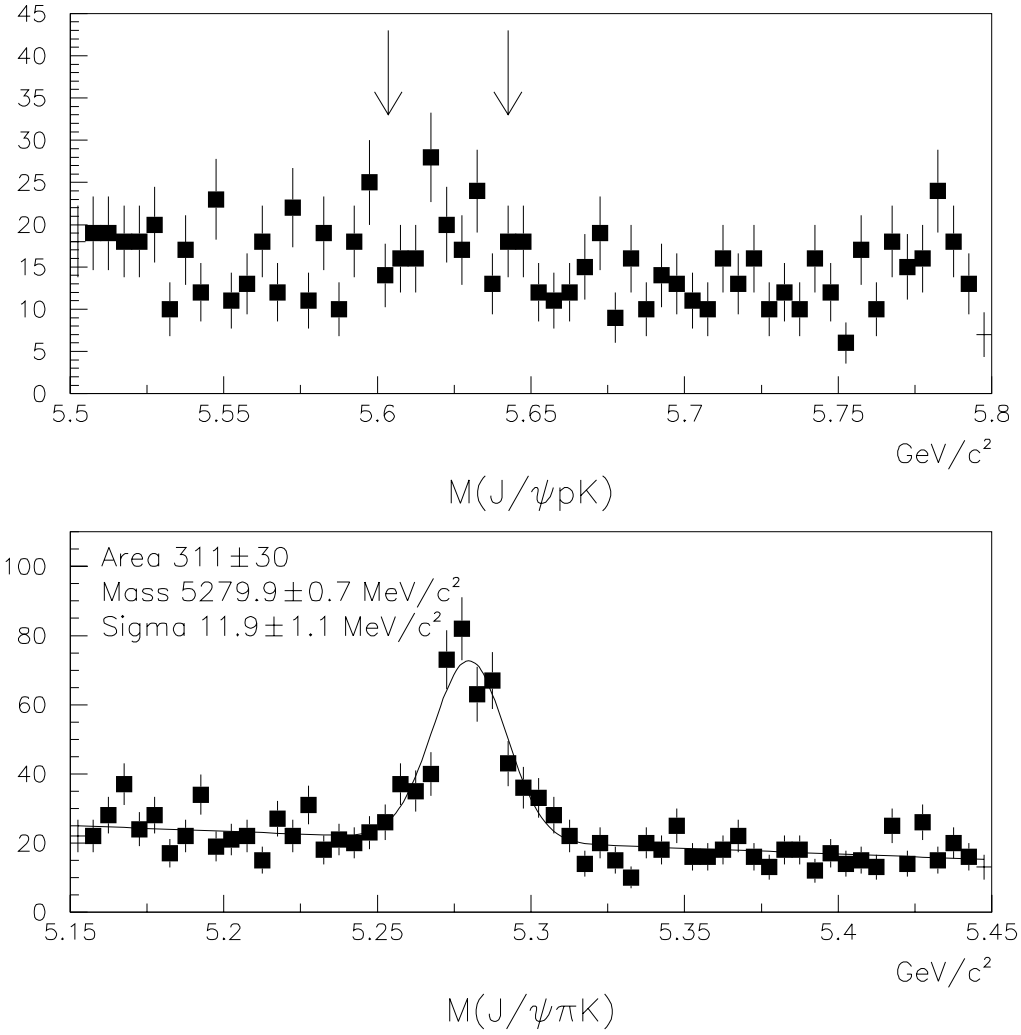

Figure 5.3: The J/ψ–p–K (top) and J/ψ–K–π (bottom) invariant masses after applying selection procedure discussed in the section 5.4 and requiring $c\tau$ greater than 100 μm and at least two tracks to have SVX information.

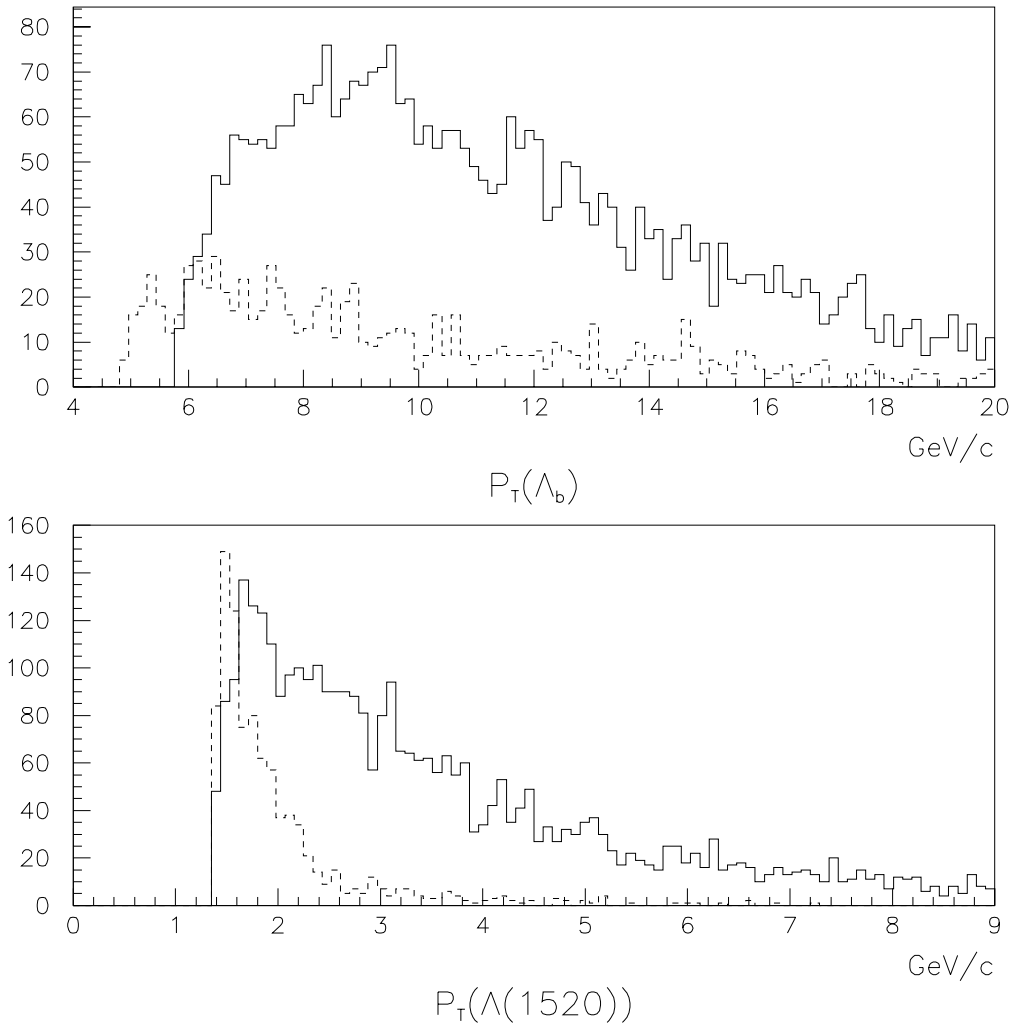

Figure 5.4: Solid — P_T distribution of Monte Carlo simulated Λ_b^0 (top) and $\Lambda(1520)$ (bottom), dashed — P_T distribution of the background from the data. Both plots have arbitrary normalization of the real and simulated data. The bottom plot has an arbitrary cut-off at 1.4 GeV/c.

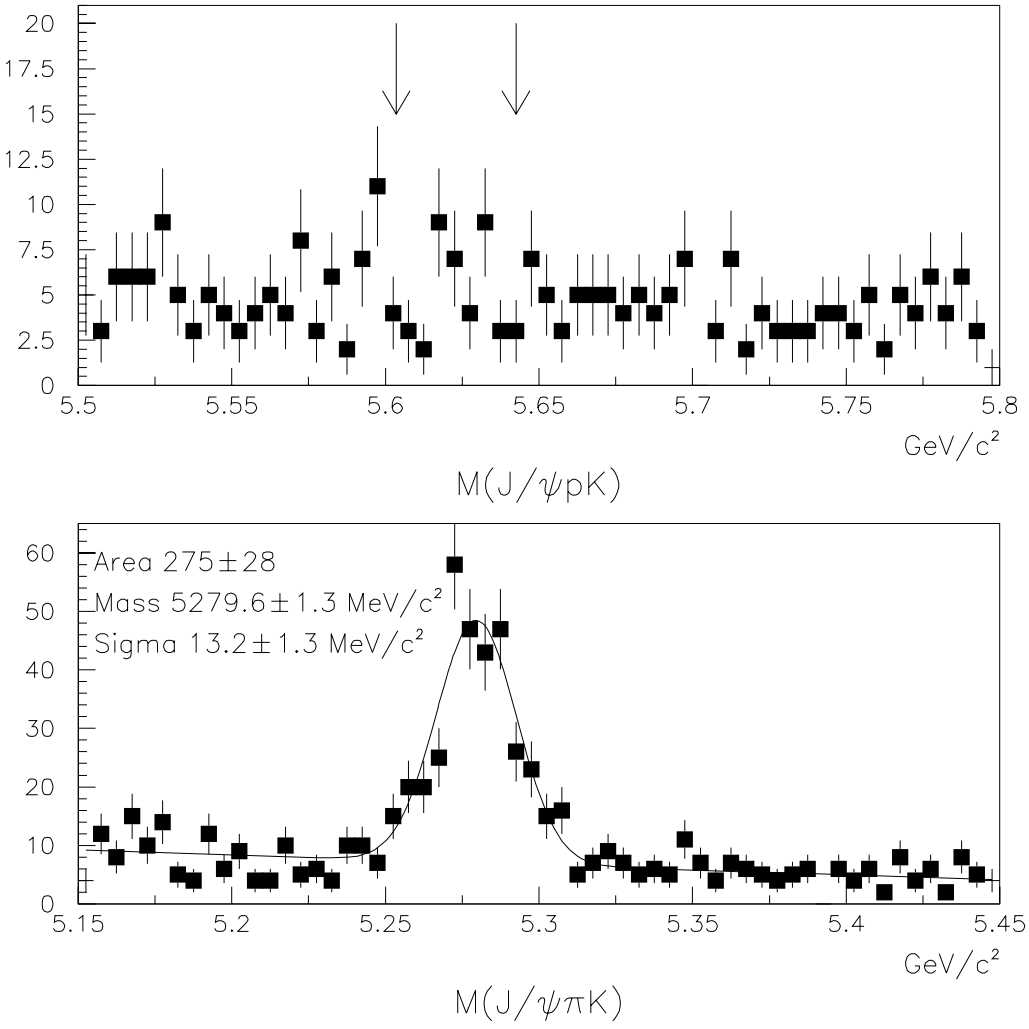

Figure 5.5: The J/ψ–p–K (top) and J/ψ–K–π (bottom) invariant mass distributions after applying the selection procedure discussed in section 5.4, the $c\tau$ cut discussed in section 5.5.1 and the P_T cuts on the B-particle and its daughter hadron. The background levels are reduced by approximately the factor of three in comparison to the distributions shown in Figure 5.3.

B^0, K^* P_T cut, GeV/c	5.0, 1.5	5.0, 2.0	5.0, 2.5	6.0, 1.5	6.0, 2.0	6.0, 2.5	7.0, 1.5	7.0, 2.0	7.0, 2.5
Signal	321	276	214	299	270	213	273	250	207
Background	253	108	55	209	99	53	144	84	49
$S^2/(S+B)$	180	198	170	176	198	171	179	187	167

Table 5.3: Signal and background for several values of the P_T cut on B^0 and K^*.

5.5.3 Check for B^0 Reflections

The combinatorial background is a major source of background for the Λ_b^0 decay mainly because we do not have a reliable way of identifying the $\Lambda(1520)$ decay products and have to loop over all track combinations to find the $\Lambda(1520)$ candidates. As demonstrated above, the combinatorial background can be suppressed by requiring a positive proper lifetime cut for Λ_b^0 and P_T cuts for $\Lambda(1520)$ and Λ_b^0 candidates. On the other hand, we reconstruct hundreds of B-mesons which possess similar P_T and $c\tau$ characteristics as B-baryons. The tracks of B-meson decay products with masses assigned according to a Λ_b^0 decay hypothesis can be another source of Λ_b^0 background since the B-meson mass in such a case is "reflected" into the Λ_b^0 search window. Figure 5.6 shows the result of a Monte Carlo study of the B^0 reflections, when pion and kaon from the K^* decay are treated as kaon and proton of a possible $\Lambda(1520)$ decay. The top plot shows the simulated B^0 peak, while the bottom plot presents the reflected B^0's into the Λ_b^0 search window.

According to the Monte Carlo, about 8% of B^0's contribute to the Λ_b^0 background. That means that having reconstructed 275 B^0 mesons (Figure 5.5, bottom), we could have observed about 22 Λ_b^0 candidates which are consistent with being reflected B^0 mesons. We check this on the data by reas-

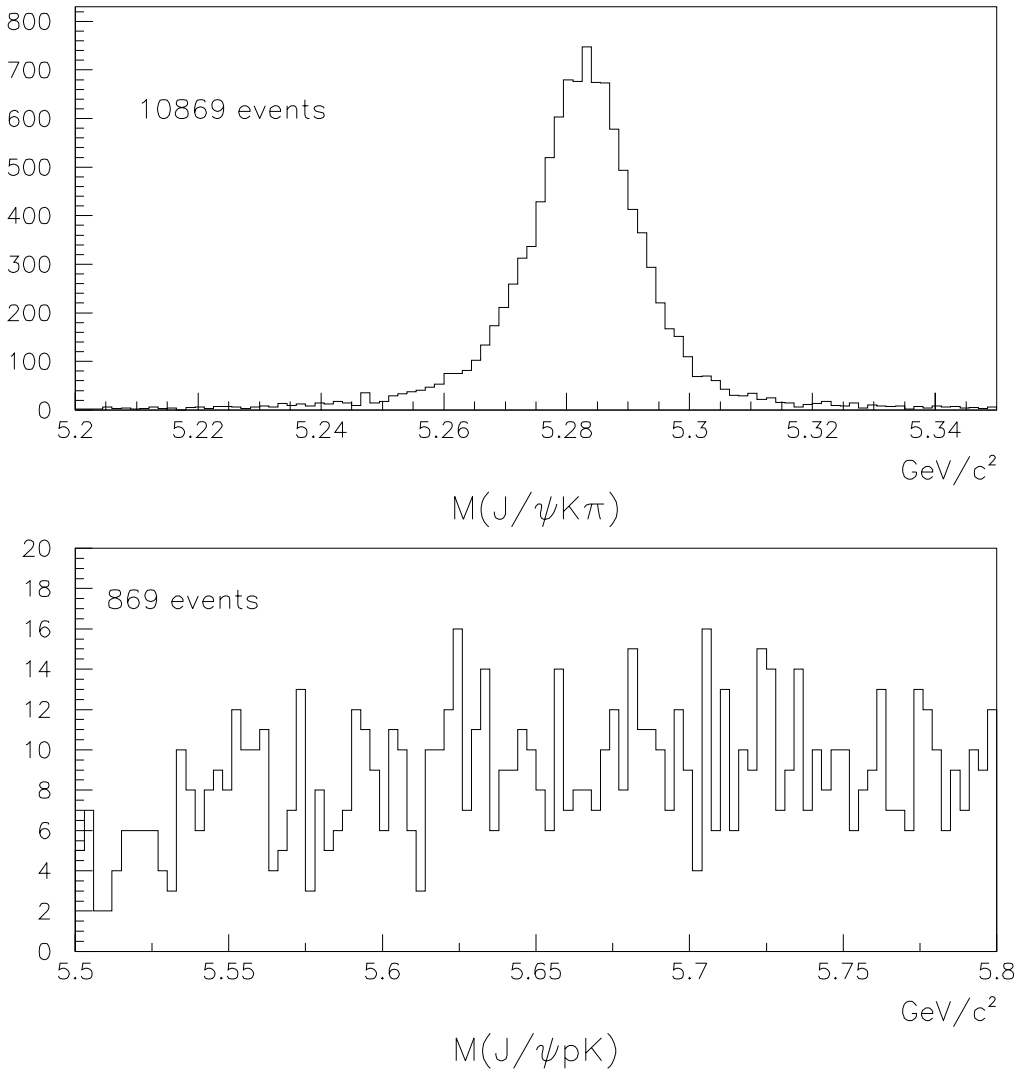

Figure 5.6: Invariant mass distribution of the Monte Carlo generated B^0 mesons (top) when reconstructed according to the Λ_b^0 decay hypothesis (bottom).

signing the masses for the tracks selected as $\Lambda(1520)$ candidates. Proton and kaon tracks are assigned kaon and pion masses respectively, and if the invariant mass becomes consistent with the K^* mass within ± 2, and the four-particle system invariant mass is consistent with the B^0 mass within $\pm 2\sigma$, we consider the event a B^0 reflection and discard it. This procedure rejects 24 Λ_b^0 candidates from Figure 5.5. Figure 5.7 shows Λ_b^0 candidates (top) after removing the B^0 reflections, and the removed events are shown in the bottom plot.

We are not able to distinguish a $\Lambda_b^0 \to J/\psi\Lambda(1520)$ decay in the data accumulated by CDF through the Tevatron Run I. The next chapter presents the calculation of the limit on the $\Lambda_b^0 \to J/\psi\Lambda(1520)$ branching ratio.

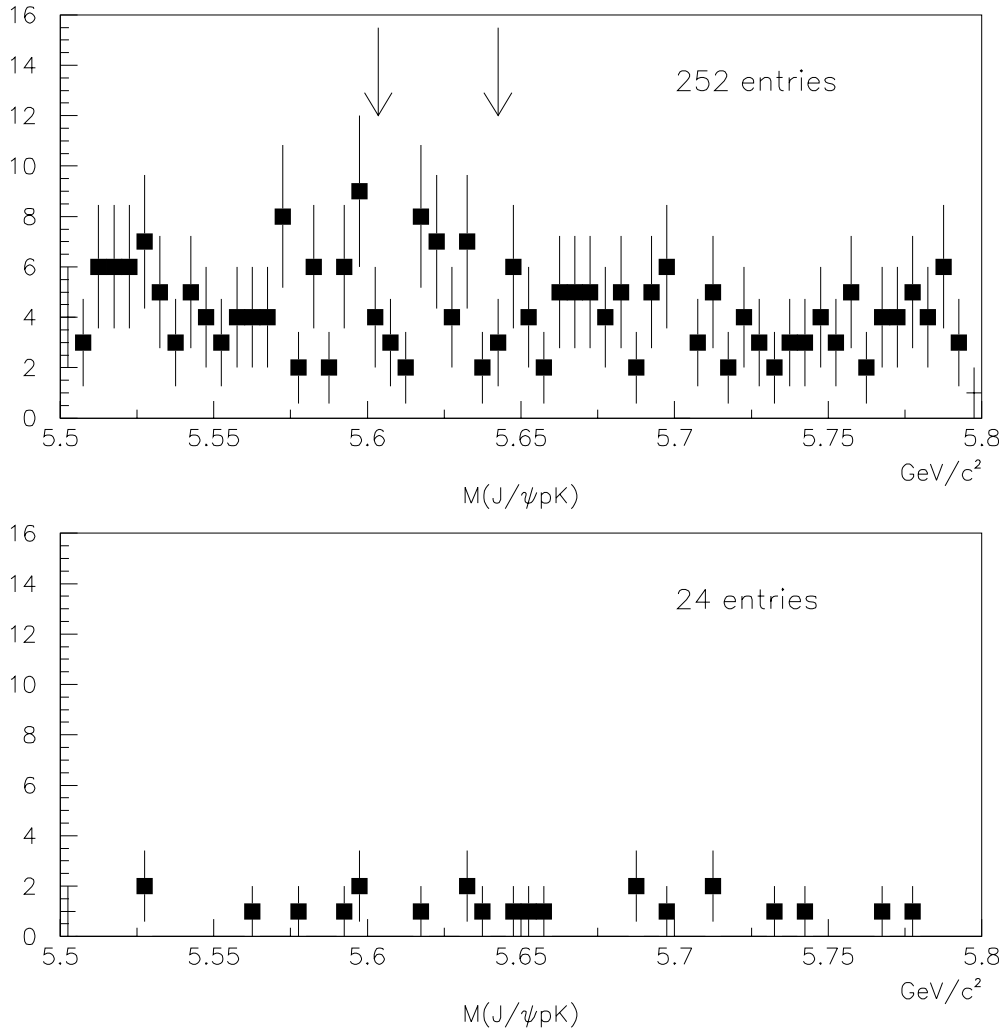

Figure 5.7: The J/ψ–p–K invariant mass distribution after removing events consistent with the reflected B^0 mesons (top) and the events recognized as B^0 reflections (bottom).

Chapter 6

Limit on $\frac{\sigma_{\Lambda_b^0}}{\sigma_{B^0}} B(\Lambda_b^0 \to J/\psi\,\Lambda(1520))$

A direct calculation of the limit on the Λ_b^0 production cross section times branching fraction $\sigma_{\Lambda_b^0} B(\Lambda_b^0 \to J/\psi\,\Lambda(1520))$ is possible with our data, but the result will contain large systematic uncertainties, including the uncertainties in the b-quark production cross section and P_T spectrum. Instead, we can calculate the limit on the ratio of the Λ_b^0 and B^0 branching fractions according to the equation:

$$\frac{\sigma_{\Lambda_b^0} B(\Lambda_b^0 \to J/\psi\Lambda(1520)) B(\Lambda(1520) \to pK) \varepsilon_{\Lambda_b^0}}{\sigma_{B^0} B(B^0 \to J/\psi K^*) B(K^* \to K\pi) \varepsilon_{B^0}} = \frac{N_{\Lambda_b^0}}{N_{B^0}} \qquad (6.1)$$

where $B(B^0 \to J/\psi K^*) = (1.58 \pm 0.28) \cdot 10^{-3}$, $B(K^* \to K^{\pm}\pi^{\mp}) = 0.66513 \pm 0.00013$, $B(\Lambda(1520) \to pK) = 0.30 \pm 0.01$ [8]. In order to do this, we have to determine the value of ε_{B^0} and $\varepsilon_{\Lambda_b^0}$ from the Monte Carlo and extract the number of observed B^0 (N_{B^0}) and an upper limit for the number of Λ_b^0 ($N_{\Lambda_b^0}$) from the data. This method allows us to minimize the systematic uncertainties since they almost completely cancel out in this ratio.

6.1 Additional Selection Requirements

In order to minimize the systematic uncertainty on the calculation of the ratio of reconstruction efficiencies for Λ_b^0 and B^0, we impose additional requirements on the samples of Λ_b^0 and B^0.

First of all, we require the J/ψ muons to be reconstructed in the CMU system, since the efficiencies of the CMX detectors are not very well measured and would introduce an unknown systematic effect. The result of this cut on the B^0 signal is shown in Figure 6.1.

The second requirement is due to the fact that the CDF tracking system efficiency is P_T-dependent for particles with transverse momenta below 400 MeV/c [47]. Another consideration is that the track reconstruction efficiency is different for tracks that pass through the whole CTC volume and those that exit the CTC from the sidewall without crossing all the CTC superlayers. Therefore, we require all tracks to have transverse momentum above 400 MeV/c and a CTC exit radius greater than 130 cm, which ensures that tracks traverse all the CTC superlayers. These cuts are relatively minor, since the P_T cuts of 2 GeV/c on $\Lambda(1520)$ and K^* do not leave many low-momentum tracks. Figure 6.2 shows the sample of B^0 candidates after this requirement.

Finally, we have limited the sample to events where the tracks of the Λ_b^0 and B^0 decay products are all reconstructed in the SVX. The requirement on the hadron proper lifetime to be greater than 100 μm, discussed in Chapter 5, will have different efficiencies for events with different numbers of tracks measured in the SVX, since the $c\tau$ resolution depends on the proportion of tracks measured in the SVX and CTC. By limiting the data sample to events with all tracks measured in the SVX, we avoid the systematic uncertainties

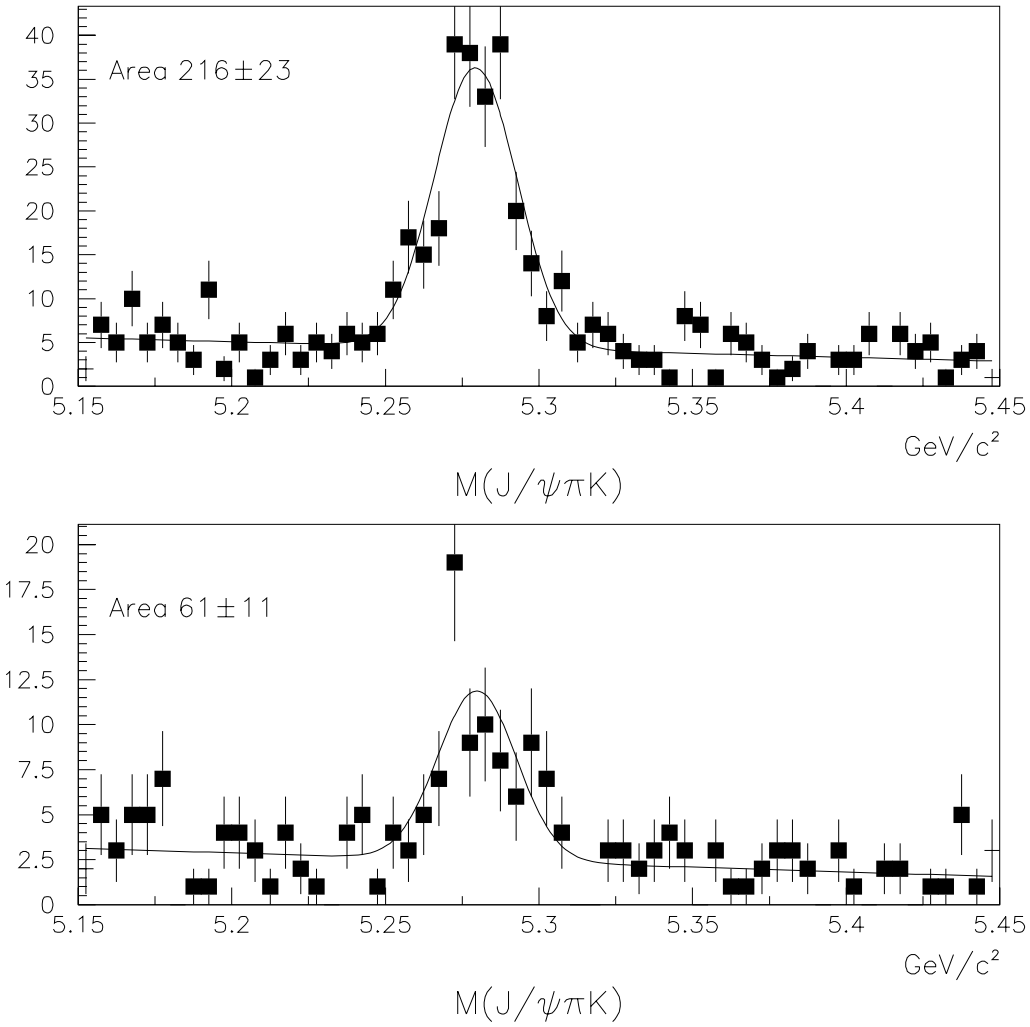

Figure 6.1: The B^0 signal after requiring the muons to be detected in the CMU system only (top) and the events removed by this cut (bottom).

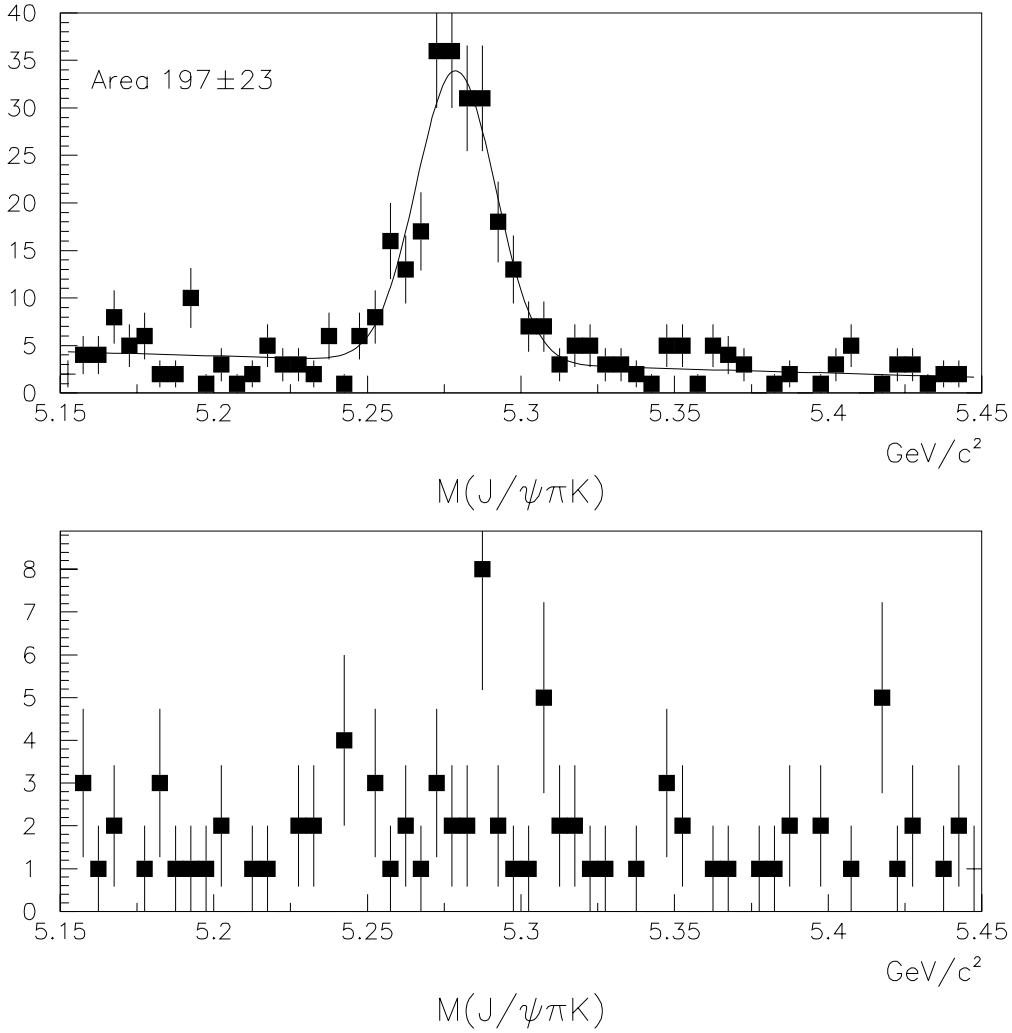

Figure 6.2: The B^0 signal after requiring tracks to have transverse momentum above 400 MeV/c and to exit the CTC at a radius greater that 130 cm (top), and the B^0 candidates removed by this cut (bottom).

associated with the detector simulation and the way in which the data is distributed along the beamline. This cut rejects 24% of the B^0 signal.

Figure 6.3 shows the B^0 invariant mass distribution after the additional cuts described in this section have been applied. This subsample is used as a reference signal for the Λ_b branching fraction limit measurement.

The additional requirements, described above, reduce the B^0 signal by about 45%. The individual rejection power of these track quality cuts on the Λ_b^0 sample is shown in Figure 6.4 and the remaining sample of Λ_b^0 candidates, which we use to find the branching fraction limit, is presented in Figure 6.5.

6.2 Ratio of Efficiencies and Systematic Uncertainties

We find the relative Λ_b^0 and B^0 reconstruction efficiencies using a Monte Carlo simulation including next-to-leading order QCD calculations [49] with renormalization scale $\mu_0^2 = (P_T^2 + m_b^2)$ and a b-quark mass $m_b = 4.75 GeV/c^2$, and the MRSD0 proton parton distribution functions. The detector simulation includes J/ψ Level-1 and Level-2 trigger simulation. We use the CDF measured Λ_b^0 lifetime [48] and the world average value for the B^0 lifetime [8].

After reconstructing the generated events with the analysis module and imposing all the cuts and selection procedures described earlier, we find the ratio of the Λ_b^0 and B^0 efficiencies, $\varepsilon_{B^0}/\varepsilon_{\Lambda_b^0} = 0.97 \pm 0.01$, where the uncertainty is statistical only. To estimate the systematic uncertainty on this ratio, we vary several theoretical and experimental parameters by their uncertainties and calculate the resulting change in $\varepsilon_{B^0}/\varepsilon_{\Lambda_b^0}$. Table 6.1 gives a breakdown of

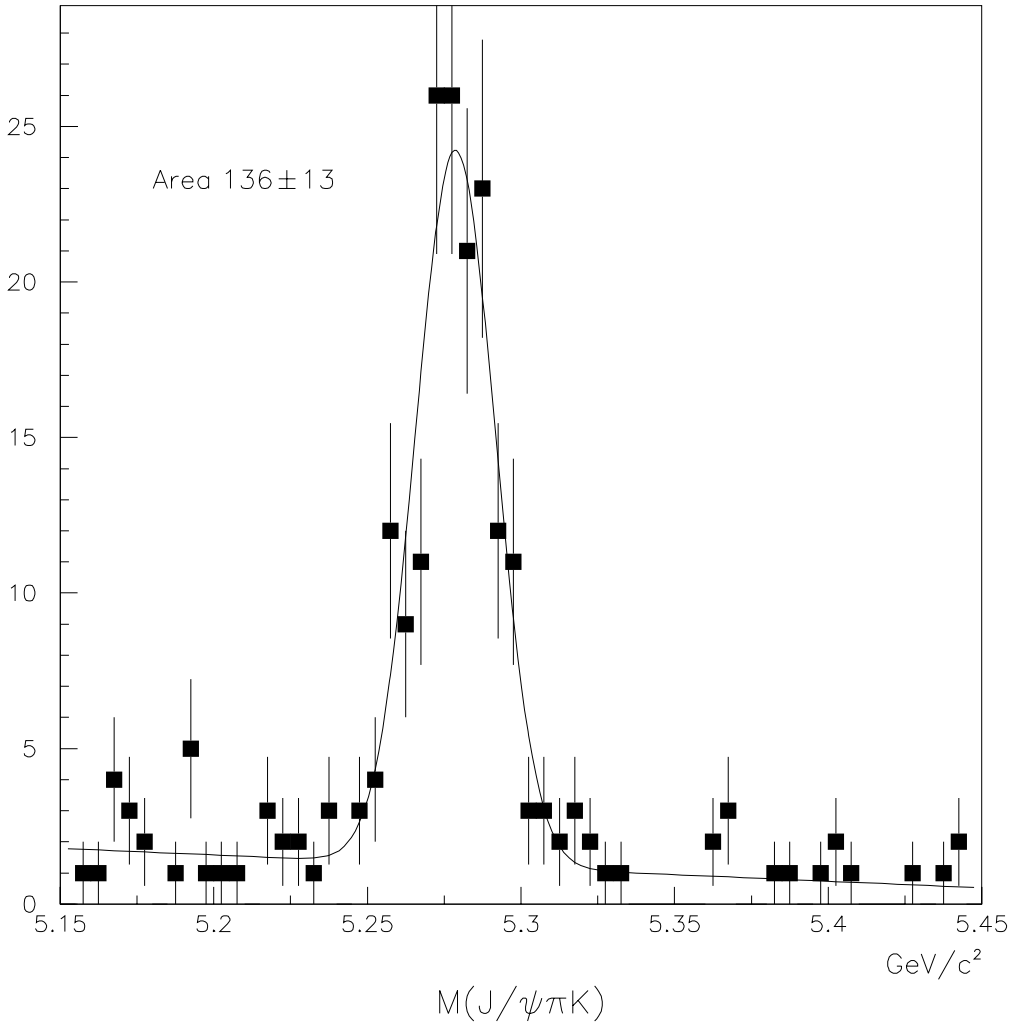

Figure 6.3: The invariant mass distribution of the B^0 candidates used as a reference signal for the Λ_b branching fraction limit measurement. All additional cuts described in Section 6.1 have been applied.

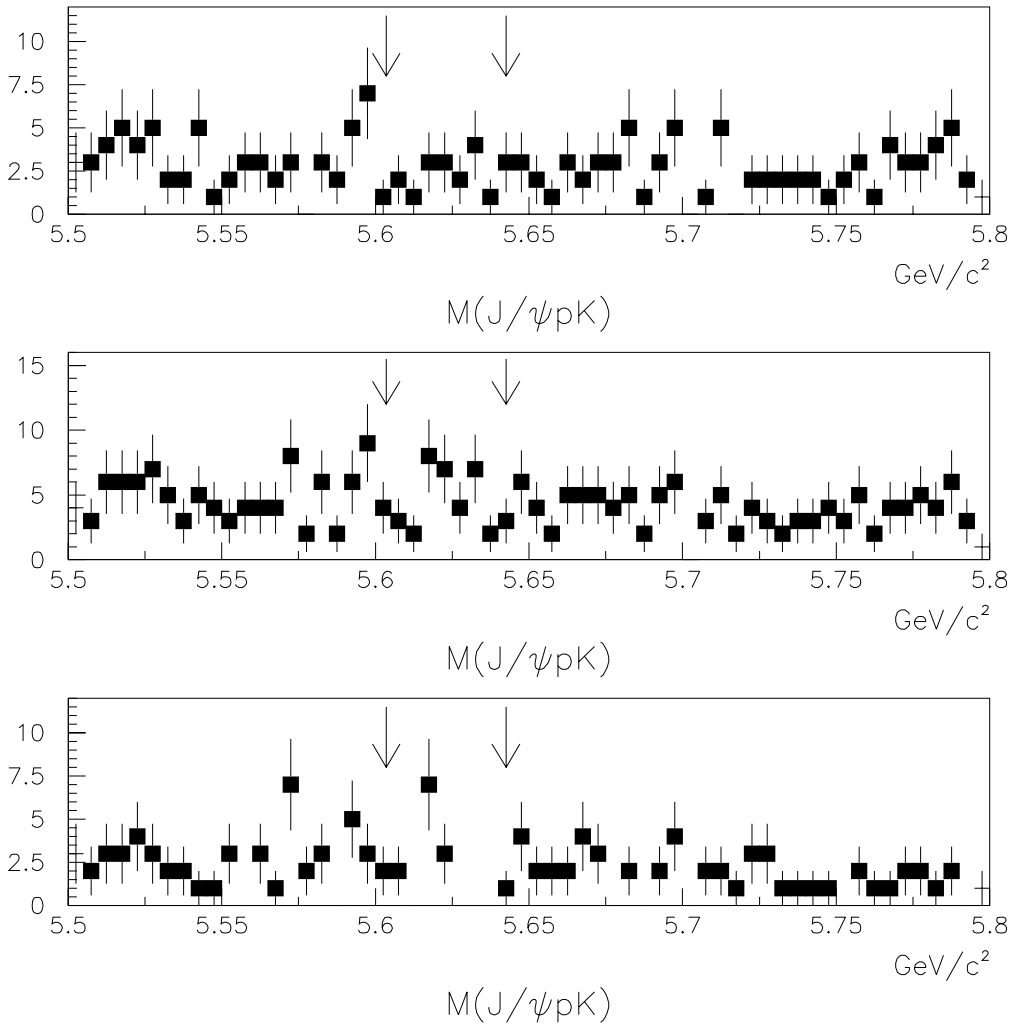

Figure 6.4: Λ_b^0 candidates rejected by the track quality requirements: CMU requirement (top), track P_T cut (middle), and SVX information requirement (bottom).

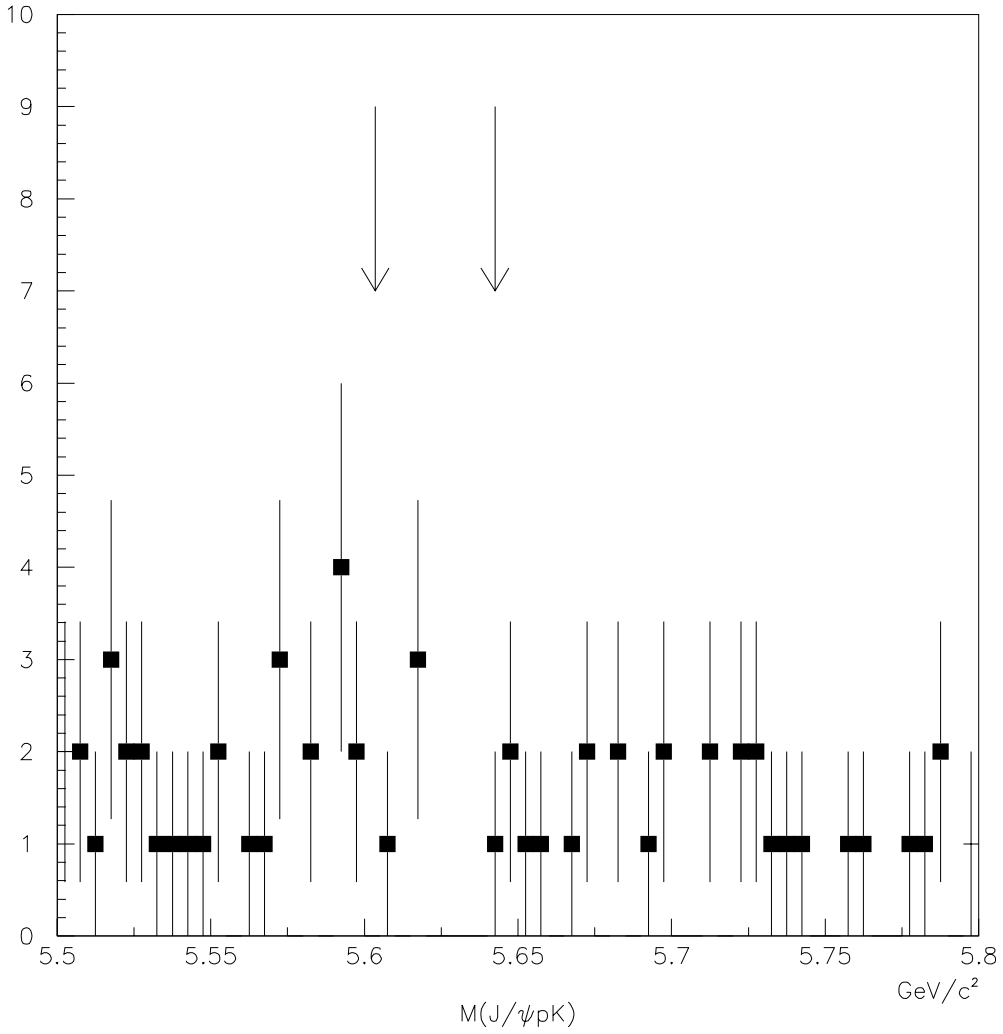

Figure 6.5: The Λ_b^0 sample after performing track quality cuts used for the branching ratio limit calculation.

the systematic uncertainties on $\varepsilon_{B^0}/\varepsilon_{\Lambda_b^0}$.

Source of Uncertainty	Central Value Used in Analysis	Variation Range	Change in $\frac{\varepsilon_{B^0}}{\varepsilon_{\Lambda_b^0}}$, %
Λ_b^0 polarization, %	0	-1 — 1	2.0
B^0 polarization, %	74	65 — 80	1.0
Peterson ϵ for Λ_b	0.006	0.002 — 0.010	8.9
Peterson ϵ for B_d	0.006	0.004 — 0.008	3.9
$c\tau(\Lambda_b)$, μm	351	318 — 384	1.5
$c\tau(B^0)$, μm	484	461 — 507	1.0
SVX $c\tau$ resolution, μm	40	0 — 80	0.5
$\Lambda(1520)$ width, MeV	15.6	14.6 — 16.6	1.3
K^* width, MeV	50.5	49.9 — 51.1	1.3
Detector mass resolution for $\Lambda(1520)$ and K^*, MeV	3 ($\Lambda(1520)$) 5 (K^*)	$\pm 25\%$ $\pm 25\%$	0.7
J/ψ trigger efficiency	standard	$\pm 1\sigma$	1.3
b spectrum	$M_b = 4.75$ GeV/c^2, $\mu = \mu_0$	$M_b = 4.5$ GeV/c^2 $\mu = \mu_0/4$ — $M_b = 5.0$ GeV/c^2 $\mu = 2 \times \mu_0$	0.7
Tracking efficiency for p, %	98.5	97 — 100	0.8
Total			10.5

Table 6.1: One standard deviation systematic uncertainties on $\varepsilon_{B^0}/\varepsilon_{\Lambda_b^0}$.

The major contribution to the uncertainty on the ratio of efficiencies is the theoretical uncertainty in the fragmentation parameters for B-mesons and especially for B-baryons (see Chapter 2). Variations in the fragmentation parameter result in different spectra of B-particles, with an impact on the overall reconstruction efficiency due to the J/ψ trigger and the tracking system inefficiency at low momenta. We find an 8.9 % (3.9 %) change in $\varepsilon_{B^0}/\varepsilon_{\Lambda_b^0}$ due to the uncertainty in the fragmentation parameter for the Λ_b^0 (B^0).

The polarizations of the Λ_b^0 and B^0 decays affect the $\Lambda(1520)$ and K^* P_T spectra. Since the Λ_b^0 polarization is not yet measured experimentally and the B^0 polarization is known with a significant uncertainty [50], [51], they introduce systematic errors in the Λ_b^0 and B^0 reconstruction efficiencies. By varying the Λ_b^0 and B^0 polarization parameters in the Monte Carlo we obtain 2 and 1 per cent change in $\varepsilon_{B^0}/\varepsilon_{\Lambda_b^0}$ respectively.

Other systematics include the uncertainties in the Λ_b^0 and B^0 lifetimes, the lifetime and mass resolution of the detector, the trigger and tracking efficiencies and the b-quark cross section uncertainty. Their contributions are rather small; most of them affect the Λ_b^0 and B^0 reconstruction in the same way and cancel out in the ratio measurement. The systematic uncertainties added in quadrature result in a 10.5% total systematic uncertainty on $\varepsilon_{B^0}/\varepsilon_{\Lambda_b^0}$.

6.3 Determination of $N_{\Lambda_b^0}$ and N_{B^0}

It is possible to determine the number of Λ_b^0 candidates, $N_{\Lambda_b^0}$, by counting the number of entries in a given mass window and subtracting the background estimated from the sidebands. Poisson statistics could then be used to calculate an upper limit. This counting method has the advantages of being simple and conservative. Its major disadvantage is insensitivity to fluctuations in the background shape. If the search window, for example, happens to have two spikes at the window edges, the counting experiment would consider them both as possible candidates. In the counting method, the limit also depends on the size of the chosen window.

An alternative method is to perform an unbinned maximum likelihood fit to the data with a two-component function (a linear function to

describe the background and a Gaussian to describe the possible signal). In this case the shape of the distribution is taken into account, yielding a more precise result. This fit involves maximizing the following likelihood function:

$$\mathcal{L} = e^{-(n_s+n_b)}\frac{(n_s+n_b)^N}{N!}\prod_{i=1}^{N}\frac{n_s\,\frac{e^{-\frac{(m_i-P_1)^2}{2(k\sigma_i)^2}}}{k\sigma_i\sqrt{2\pi}} + n_b\,(P_2 m_i + P_3)}{n_s+n_b} \qquad (6.2)$$

where n_s and n_b are the number of signal and background events respectively, which together with P_n are the parameters of the fit. N is the total number of events in the mass distribution, m_i and σ_i are the measured mass and mass uncertainty for each event, and k is a scaling factor for σ_i. Its value is determined from a fit to the distribution of $(M(B^0) - m_i)/\sigma_i$, where $M(B^0)$ is the world average mass of the B^0, and m_i and σ_i are mass and mass uncertainty of each event in the B^0 sample used as a reference signal for the Λ_b branching fraction limit measurement (Figure 6.3). The expected distribution of $(M(B^0) - m_i)/\sigma_i$ is a Gaussian centered at zero with $\sigma = 1$ when both m_i and σ_i are determined correctly. The fit result shown in Figure 6.6 suggests that the mass uncertainty is underestimated by a factor of 1.44 ± 0.13. We correct it by scaling σ_i in Formula 6.2 by $k = 1.44$.

In order to find the most probable number of signal events, we fix n_s and maximize the likelihood function with respect to the other fit parameters. For the determination of $N_{\Lambda_b^0}$, parameter P_1, which corresponds to the mass of the signal being fitted, is allowed to vary only between the bounds determined from our Λ_b^0 mass measurement described in the next chapter, i.e. between 5603.5 and 5642.5 MeV/c^2. This procedure is repeated for different values of n_s. The top plot of Figure 6.7 shows the distribution of $-2\ln(\mathcal{L})$ versus the number of Λ_b^0 signal candidate events. According to the fit, the most probable

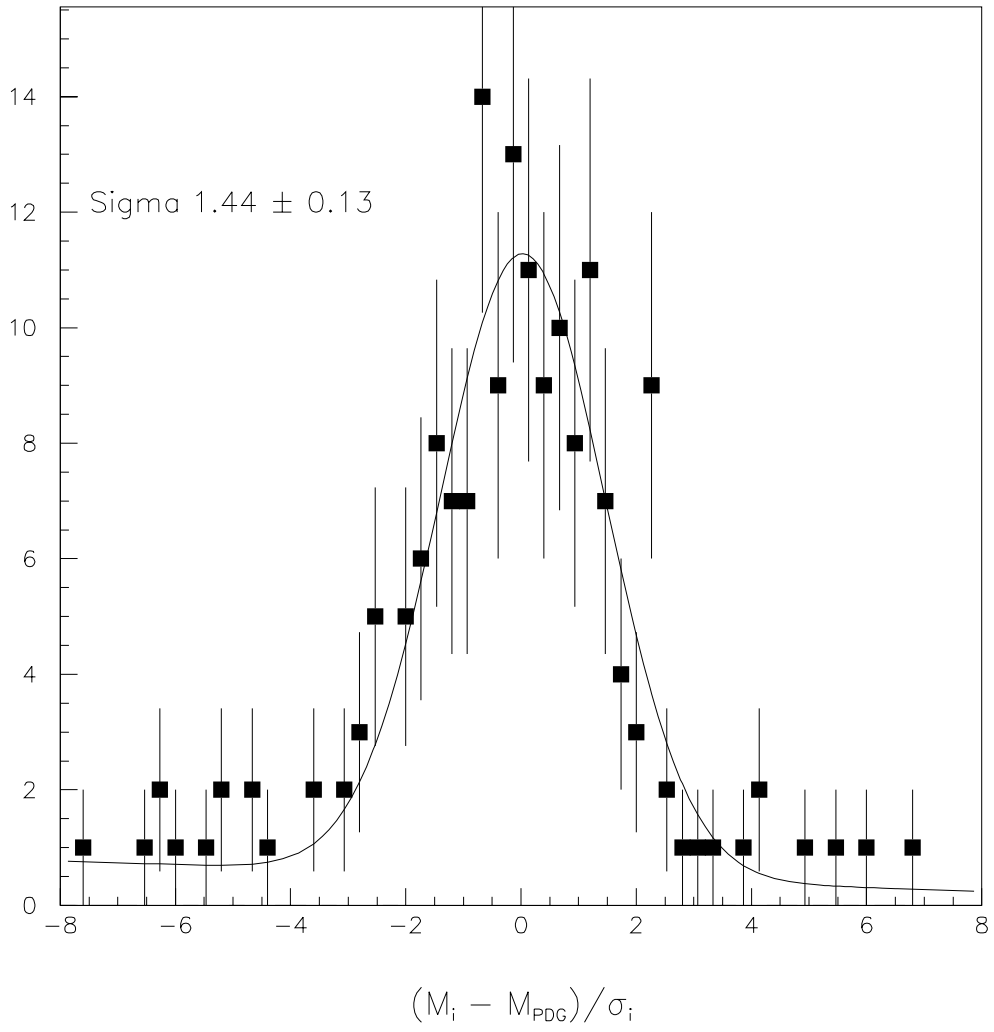

Figure 6.6: The distribution of the difference between world average and measured mass weighted by the measured mass uncertainty for the B^0 sample. The Gaussian fit to this distribution has $\sigma = 1$ when mass uncertainty is scaled by $k = 1.44$.

number of Λ_b^0 events in our data is $N_{\Lambda_b^0} = 0$. The same method, applied to the sample of B^0 candidates, returns the result $N_{B^0} = 135.9$ (bottom plot of Figure 6.7). The likelihood intervals corresponding to a 68.3% probability have a total width of $\Delta N_{\Lambda_b^0} = 3.1$ and $\Delta N_{B^0} = 25.0$ events respectively.

To check the effect of the scaling factor k uncertainty on the measurement, the above procedure was performed for $1.3 < k < 1.6$. The variation of k affects both N_{B^0} and the limit on $N_{\Lambda_b^0}$ (at 90% confidence level) by no more than 2%. The limit on the ratio $N_{\Lambda_b^0}/N_{B^0}$ changes by less than 1% when k is varied. This effect is very small compared, for example, to the statistical uncertainty on N_{B^0} and is not taken into account in further calculations of the limit.

6.4 The Limit on the Branching Ratio

We can rewrite Equation 6.1 so that the left-hand part of the equation is the product for which the limit is being found:

$$\frac{\sigma_{\Lambda_b^0}}{\sigma_{B^0}} B(\Lambda_b^0 \to J/\psi\Lambda(1520)) = B(B^0 \to J/\psi K^*) \frac{B(K^* \to K\pi)}{B(\Lambda(1520) \to pK)} \frac{\varepsilon_{B^0}}{\varepsilon_{\Lambda_b^0}} \frac{N_{\Lambda_b^0}}{N_{B^0}} \tag{6.3}$$

A simplified way of calculating the limit on $\frac{\sigma_{\Lambda_b^0}}{\sigma_{B^0}} B(\Lambda_b^0 \to J/\psi\Lambda(1520))$ is to find the upper limit for $N_{\Lambda_b^0}$ with a certain confidence level (for example, 90%) and increase $B(B^0 \to J/\psi K^*) \frac{B(K^* \to K\pi)}{B(\Lambda(1520) \to pK)} \frac{\varepsilon_{B^0}}{\varepsilon_{\Lambda_b^0}} \frac{1}{N_{B^0}}$ by a given amount to take into account possible upward fluctuations. For example, if we increase $B(B^0 \to J/\psi K^*) \frac{B(K^* \to K\pi)}{B(\Lambda(1520) \to pK)} \frac{\varepsilon_{B^0}}{\varepsilon_{\Lambda_b^0}} \frac{1}{N_{B^0}}$ by one standard deviation, we get:

$$\frac{\sigma_{\Lambda_b^0}}{\sigma_{B^0}} B(\Lambda_b^0 \to J/\psi\Lambda(1520)) < (B(B^0 \to J/\psi K^*) + \sigma(B(B^0 \to J/\psi K^*))) \times$$

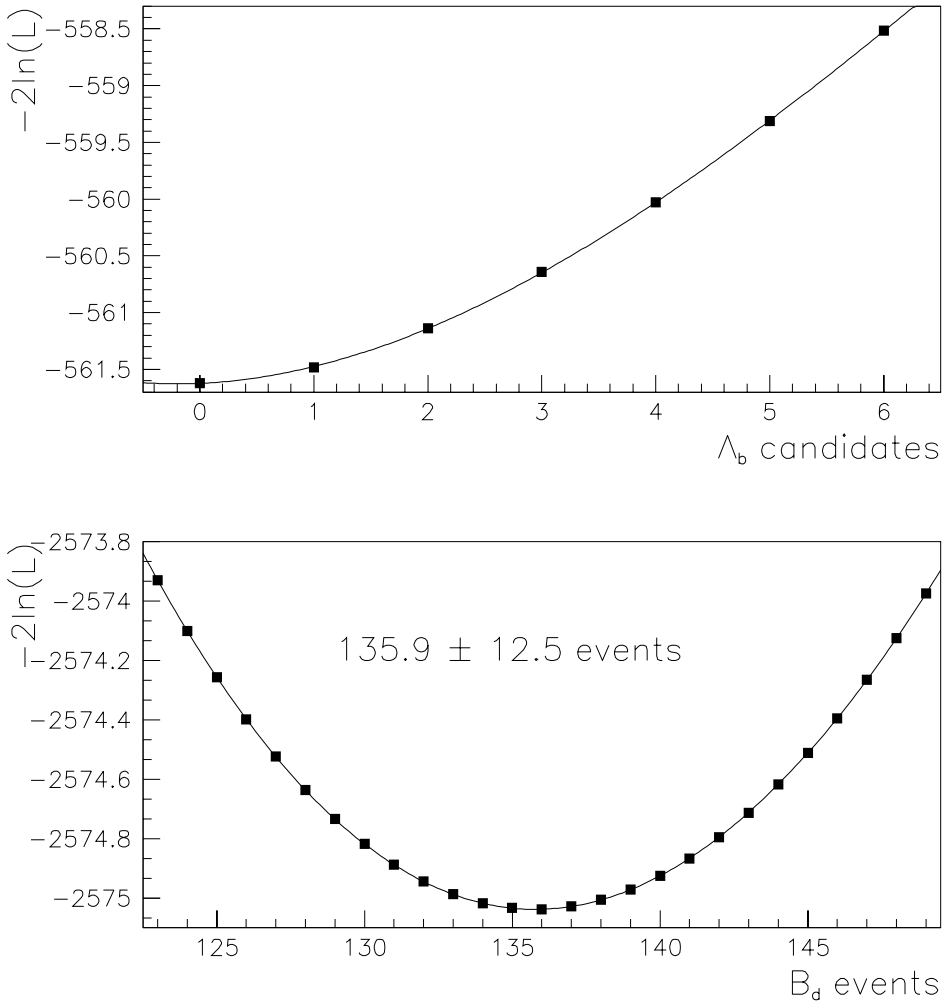

Figure 6.7: Likelihood as a function of the number of signal events for Λ_b^0 (top) and B^0 (bottom).

$$\times \frac{B(K^* \to K\pi) + \sigma(B(K^* \to K\pi))}{B(\Lambda(1520) \to pK) - \sigma(B(\Lambda(1520) \to pK))} \times (\frac{\varepsilon_{B^0}}{\varepsilon_{\Lambda_b^0}} + \sigma(\frac{\varepsilon_{B^0}}{\varepsilon_{\Lambda_b^0}})) \frac{N_{\Lambda_b^0}^{(90\% CL)}}{N_{B^0} - \sigma(N_{B^0})}$$

where $N_{\Lambda_b^0}^{(90\% CL)}$ is the limit on the number of observed Λ_b^0 events at the 90% confidence level, and $\sigma(X)$ is the uncertainty on X. The result of this calculation is:

$$\frac{\sigma_{\Lambda_b^0}}{\sigma_{B^0}} B(\Lambda_b^0 \to J/\psi\Lambda(1520)) < 1.67 \times 10^{-4}.$$

Unfortunately, this approach does overestimate the limit. If the product $B(B^0 \to J/\psi K^*)\frac{B(K^* \to K\pi)}{B(\Lambda(1520) \to pK)}\frac{\varepsilon_{B^0}}{\varepsilon_{\Lambda_b^0}}\frac{1}{N_{B^0}}$ was known with infinite precision, using $N_{\Lambda_b^0}$ limit at the 90% confidence level would provide the limit on $\frac{\sigma_{\Lambda_b^0}}{\sigma_{B^0}} B(\Lambda_b^0 \to J/\psi\Lambda(1520))$ at the same 90% confidence level. The fact that all uncertainties on $B(B^0 \to J/\psi K^*)\frac{B(K^* \to K\pi)}{B(\Lambda(1520) \to pK)}\frac{\varepsilon_{B^0}}{\varepsilon_{\Lambda_b^0}}\frac{1}{N_{B^0}}$ have to be taken into account increases the value of the confidence level for $\frac{\sigma_{\Lambda_b^0}}{\sigma_{B^0}} B(\Lambda_b^0 \to J/\psi\Lambda(1520))$.

The correct way of calculating the limit is to construct the likelihood function with the parameter $B(B^0 \to J/\psi K^*)\frac{B(K^* \to K\pi)}{B(\Lambda(1520) \to pK)}\frac{\varepsilon_{B^0}}{\varepsilon_{\Lambda_b^0}}\frac{N_{\Lambda_b^0}}{N_{B^0}}$ and find a 90% confidence interval with respect to this parameter. This procedure is not practical since the experimental observable is the invariant mass distribution and the fitting parameter must be a number of events.

To find the limit, therefore, we use a numerical Monte Carlo method with the assumption that all the components from

$$B(B^0 \to J/\psi K^*)\frac{B(K^* \to K\pi)}{B(\Lambda(1520) \to pK)}\frac{\varepsilon_{B^0}}{\varepsilon_{\Lambda_b^0}}\frac{1}{N_{B^0}}$$

have Gaussian errors. The probability distribution of observing a number of Λ_b^0 events in our data, shown in Figure 6.8, is found by maximizing the likelihood function 6.2. Then the number of Λ_b^0 events, $N_{\Lambda_b^0}$, is generated randomly

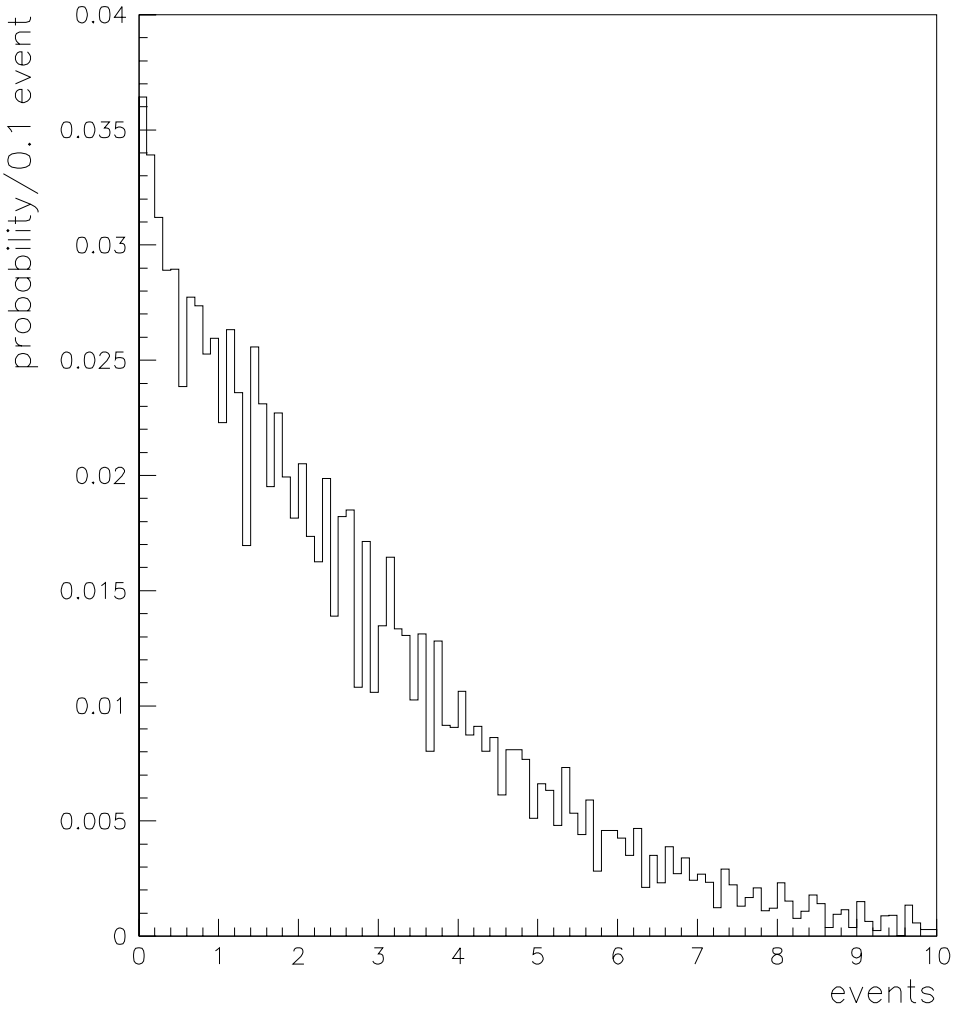

Figure 6.8: The probability distribution of observing a number of Λ_b signal events.

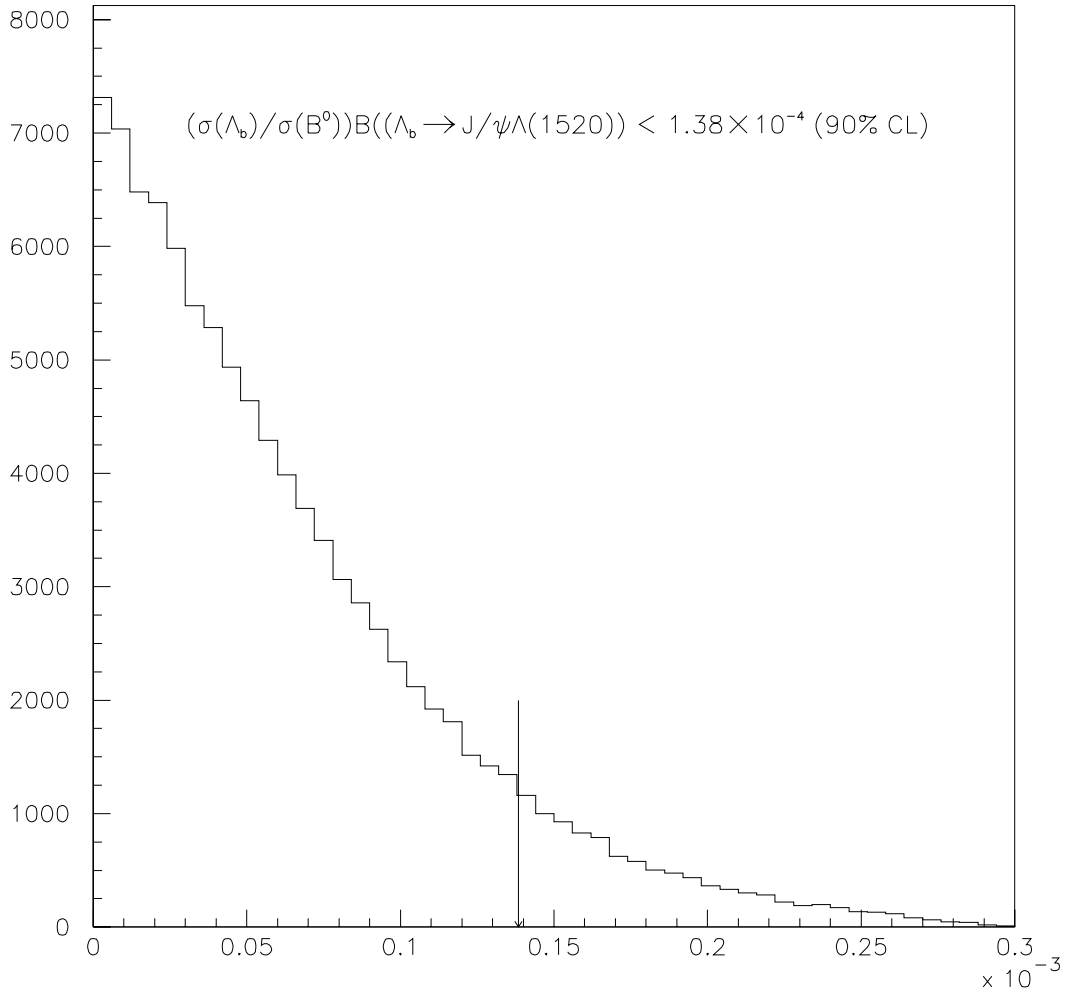

Figure 6.9: $\frac{\sigma_{\Lambda_b^0}}{\sigma_{B^0}} B(\Lambda_b^0 \to J/\psi\Lambda(1520))$ distribution. The histogram area to the left of the arrow is 90% of the total histogram area.

according to this distribution and the other terms from the right part of Equation 6.3 are generated independently according to the Gaussian distribution with corresponding means and widths. The product $\frac{\sigma_{\Lambda_b^0}}{\sigma_{B^0}} B(\Lambda_b^0 \to J/\psi\Lambda(1520))$ is then calculated from Equation 6.3. This procedure is repeated a large number of times and the distribution of $\frac{\sigma_{\Lambda_b^0}}{\sigma_{B^0}} B(\Lambda_b^0 \to J/\psi\Lambda(1520))$, shown in Figure 6.9, is obtained. In this approach, therefore, all the components from the right-hand part of the Equation 6.3 assume all their possible values within known limits instead of being fixed at a predetermined level. We find that 90% of the time the value of $\frac{\sigma_{\Lambda_b^0}}{\sigma_{B^0}} B(\Lambda_b^0 \to J/\psi\Lambda(1520))$ is less than $1.38 \cdot 10^{-4}$.

Chapter 7

Observation of $\Lambda_b^0 \to J/\psi\,\Lambda$

Another exclusive B-baryon decay that can be studied at CDF is the $\Lambda_b^0 \to J/\psi\,\Lambda$ decay. The advantage of this mode is that it is easy to form an efficient dimuon trigger, as in the case of $\Lambda_b^0 \to J/\psi\,\Lambda(1520)$, and the Λ is easily identified even without particle identification system because of its characteristic decay pattern and the long decay length. The transverse topology of the decay chain $\Lambda_b^0 \to J/\psi\,\Lambda$, $J/\psi \to \mu^+\,\mu^-$, $\Lambda \to p\,\pi$ is shown in Figure 7.1. The main difference between this decay mode and the one discussed in the previous two chapters is that the Λ_b^0 daughter, the Λ, is long lived with an average lifetime of $(2.632 \pm 0.020) \times 10^{-10}$ s [8]. Another feature of the Λ decay is that the proton is carrying more than 80% of the parent momentum (for Λ momenta much larger than the Q value of the decay). This makes it easy to distinguish proton and pion, but severely reduces the decay's reconstruction efficiency because of the CDF tracking system cut-off at low momenta.

When reconstructing the $\Lambda_b^0 \to J/\psi\Lambda(1520)$ decay, we use the decay of the B-meson , $B^0 \to J/\psi\,K^*$ for monitoring purposes. Now we will use

another B^0 decay mode, $B^0 \to J/\psi\, K_s^0$ with $K_s^0 \to \pi^+\pi^-$ for the same purposes, since it has decay kinematics similar to $\Lambda_b^0 \to J/\psi\Lambda$. The K_s^0 has an average lifetime of $(0.8927 \pm 0.0009) \times 10^{-10}$ s [8], so in both cases we have to reconstruct two displaced vertices.

We use the same track selection procedures and geometric and kinematic constrained fits for this part of the analysis as described in Chapter 5.

7.1 Λ and K_s^0 Candidate Selection

The candidates for the $\Lambda \to p\,\pi^-$ events in the J/ψ are sample are identified by testing all pairs of oppositely charged tracks (except for those identified as the J/ψ daughters) for consistency with the Λ mass. We assign the proton mass to the track with the highest momentum in each pair. According the a Monte Carlo study, this is always correct for Λ reconstructed in the CDF detector. At the same time we search the data for $K_s^0 \to \pi^+\pi^-$ events. The Λ and K_s^0 candidates are subjected to the vertex constraints and three requirements are imposed to reduce the combinatorial backgrounds. We require the Λ/K_s^0 vertex to be displaced by more than 1.0 cm with respect to the $\mu^+\mu^-$ vertex in the transverse plane in the direction of the Λ/K_s^0 transverse momentum. This reduces the background due to tracks originating from the primary vertex. For each track belonging to a Λ/K_s^0 candidate we require consistency between the ionization loss measured in the CTC and the expected loss for the type of particle and its momentum. It is easy to separate pions and protons because of the difference in their masses and we are able to identify which track corresponds to the proton candidate. If the measured ionization is

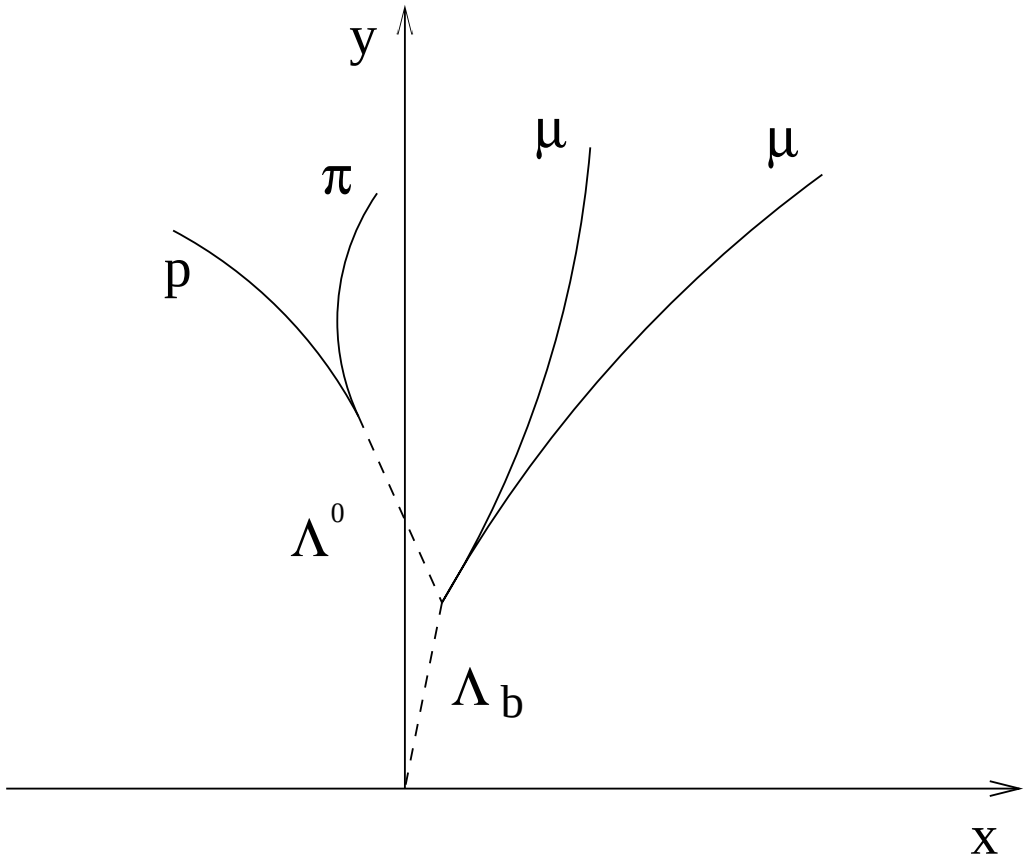

Figure 7.1: The transverse $\Lambda_b^0 \to J/\psi\,\Lambda$ event topology.

different from the predicted value by more than 2σ, we reject that candidate. As in the $\Lambda(1520)/K^*$ reconstruction procedure, we make a P_T cut on the Λ and K_s^0 candidates. Because of the soft spectrum of pions from $\Lambda \rightarrow p\,\pi^-$ decay, the requirement is $P_T > 1.5$ GeV/c for Λ and K_s^0 candidates in order to preserve the signal. Figures 7.2 and 7.3 show the invariant mass distributions of the $p\,\pi^-$ and $\pi^+\,\pi^-$ samples respectively after the selection criteria listed above.

7.2 Λ_b^0 and B^0 Candidate Selection

To reconstruct the $\Lambda_b^0 \rightarrow J/\psi\Lambda$ decay, we select Λ candidates with invariant mass within ± 4 MeV/c^2 of the world average Λ mass of 1115.7 MeV/c^2 (arrows on Figure 7.2) and combine them with the J/ψ candidates. The mass window for K_s^0 candidates is taken to be ± 12 MeV/c^2 around the K_s^0 mass of 497.67 MeV/c^2. The four tracks are subjected to a constrained fit where the dimuon is required to have the J/ψ mass, the Λ/K_s^0 momentum is required to point away from the dimuon vertex and the total momentum of the four tracks is pointing away from the primary vertex. The cuts, listed in Chapter 5, are also used in this analysis: the Λ_b^0 and B^0 candidates are required to have a lifetime $c\tau > 100$ μm, and a transverse momentum $P_T > 6.0$ GeV/c. Figure 7.4 shows the $J/\psi\,\Lambda$ invariant mass spectrum after following the above procedures and rejecting $\pi - p$ candidates if a $\pi - \pi$ mass assignment results in an invariant mass consistent with K_s^0 decay (similar to the procedure described in Section 5.5.3). Figure 7.5 shows the $J/\psi\,K_s^0$ invariant mass distribution.

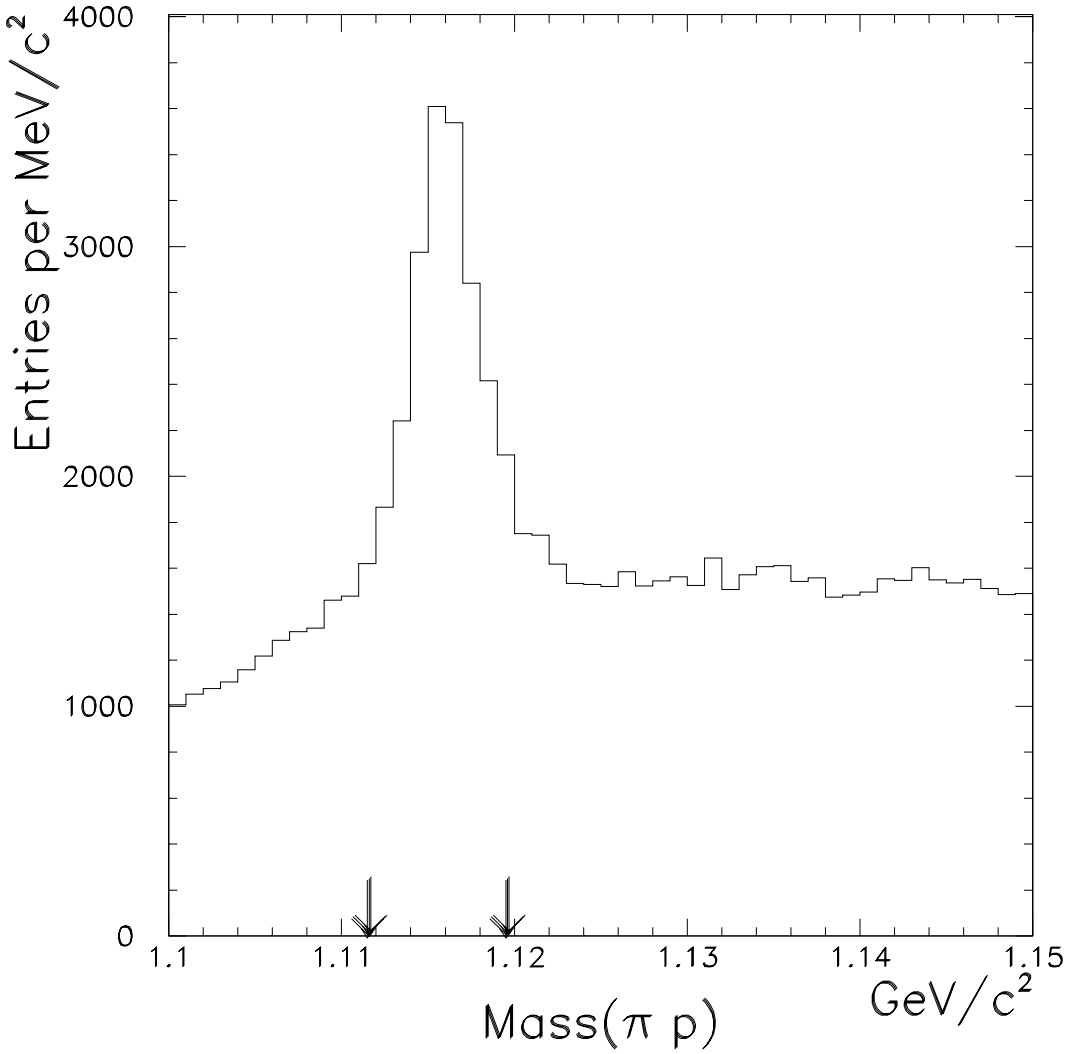

Figure 7.2: The $p\pi^-$ invariant mass distribution; the area between the arrows indicates the range used as Λ candidates.

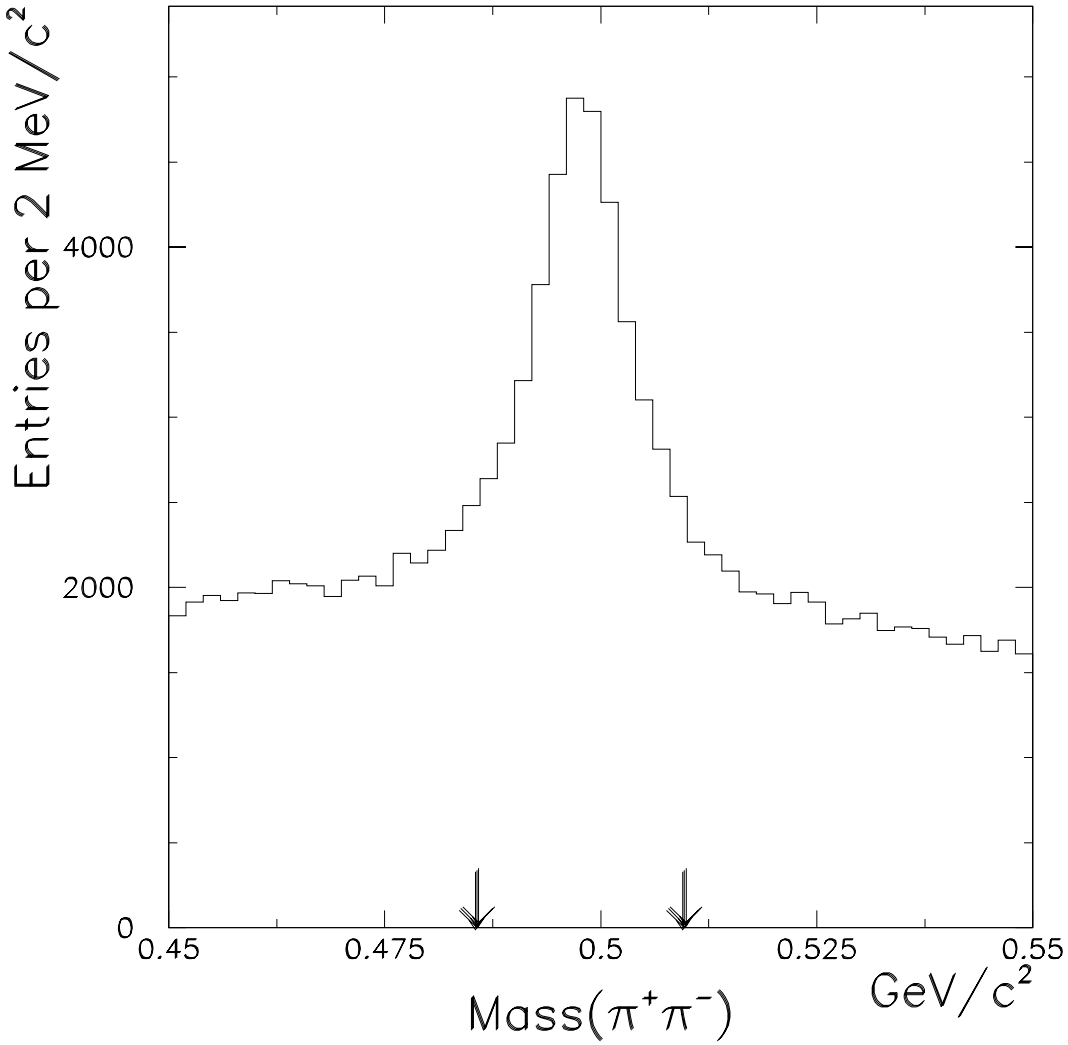

Figure 7.3: The $\pi^+ \pi^-$ invariant mass distribution; the area between the arrows indicates the range used as K_s^0 candidates.

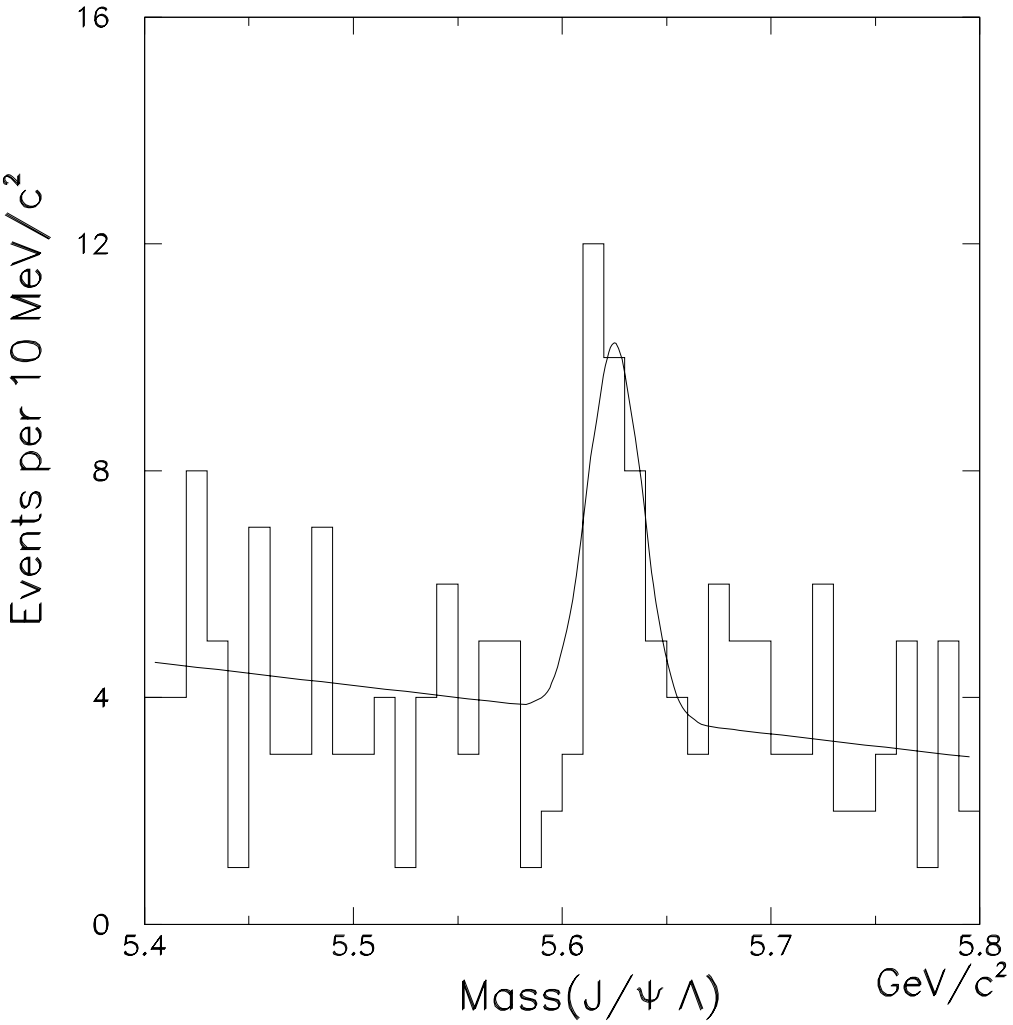

Figure 7.4: The $J/\psi\,\Lambda$ invariant mass distribution; the result of a binned likelihood fit with width of the Gaussian fixed to 13 MeV/c^2 is shown.

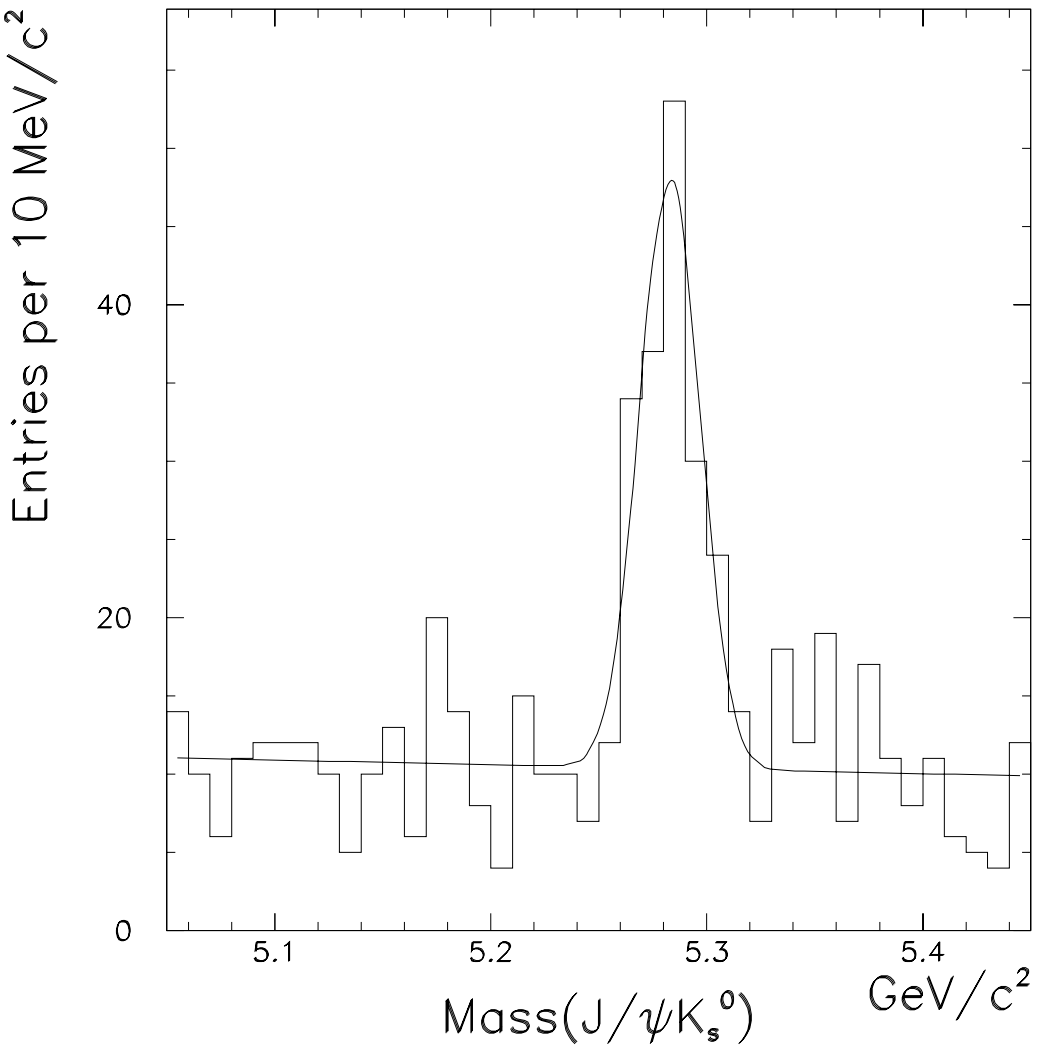

Figure 7.5: The $J/\psi\, K_s^0$ invariant mass distribution.

7.3 Λ_b^0 Mass Determination

We observe 38 events in the mass range 5.60 – 5.65 GeV/c^2 (Figure 7.4), which should contain 90% of the Λ_b^0 signal given an expected mass resolution of 13 MeV/c^2. The expected average number of background events in this mass region is 18.1 ± 1.6, as interpolated from a linear fit to the sidebands. The number of Λ_b^0 candidates in the signal region, returned from the Gaussian part of the fit is 19.9 ± 6.4. The probability that this signal is due to a background fluctuation corresponds to approximately 3.1σ for a normal distribution. The statistical significance of the signal has also been tested for variations in the event selection requirements and the signal was found to be robust. The measured B^0 mass of 5281.3 ± 1.8 MeV/c^2 (Figure 7.5) is consistent with the world average value of 5279.2 ± 1.8 MeV/c^2, and the width is consistent with the expected mass resolution.

To determine the Λ_b^0 mass, we apply an unbinned likelihood fit to the data of Figure 7.4. We use the likelihood of Equation 6.2, developed for the $\Lambda_b^0 \to J/\psi\,\Lambda(1520))$ analysis, and obtain $M(\Lambda_b^0) = 5621 \pm 4$ MeV/c^2.

7.4 Systematic Uncertainties on the Λ_b^0 Mass Measurement

The absolute value of the momentum scale in CDF is calibrated by normalizing the average reconstructed J/ψ mass to its world average value, as described in Chapter 5. During the course of Run I we observe a time dependent variation of the magnetic field which results in the J/ψ mass variation shown in Figure 7.6. The full range of field variation corresponds to a mass

variation of 2.6 MeV/c^2 for both B^0 and Λ_b^0. We take one half of this variation as the systematic uncertainty due to the momentum scale.

A variation in the measured J/ψ mass as a function of the difference in polar angle between the two muons was noted in the earlier CDF mass measurements [53, 54]. The uncertainty in the J/ψ mass shown in Figure 7.7 translates into an uncertainty in the Λ_b^0 and B^0 mass of 2.0 MeV/c^2.

The measured mass uncertainty for each event, σ_i from Formula 6.2, is a function of the reconstructed track parameter uncertainties which can be miscalculated because of lack of understanding of the material in the detector. The track fitting procedure has been modified for the Λ_b^0 and B^0 candidates to include the effect of multiple scattering in all known detector materials by scaling the covariance matrix. A mass shift of 0.5 MeV/c^2 is seen when the covariance matrix scaling is varied over a wide range, and this value is assigned as the systematic uncertainty in mass due to uncertainty in track parameter measurement.

Reconstructed tracks have their momentum measurements corrected for the energy loss due to passage through the material within the tracking system. The error in this correction has the potential of introducing a systematic uncertainty in the measured Λ_b^0 mass because the relatively slow moving proton in the Λ decay would be quite sensitive to it. The change in mass of the $J/\psi\,\Lambda$ candidates is studied for a variety of energy loss corrections as described in [53] and an average shift of 0.6 MeV/c^2 is observed. This value is taken as the systematic uncertainty due to the energy loss correction.

The summary of the systematic uncertainties on the Λ_b^0 mass measurement is given in Table 7.1. The total uncertainty of 3.0 MeV/c^2 is obtained by adding the listed numbers in quadrature. This number is also a valid es-

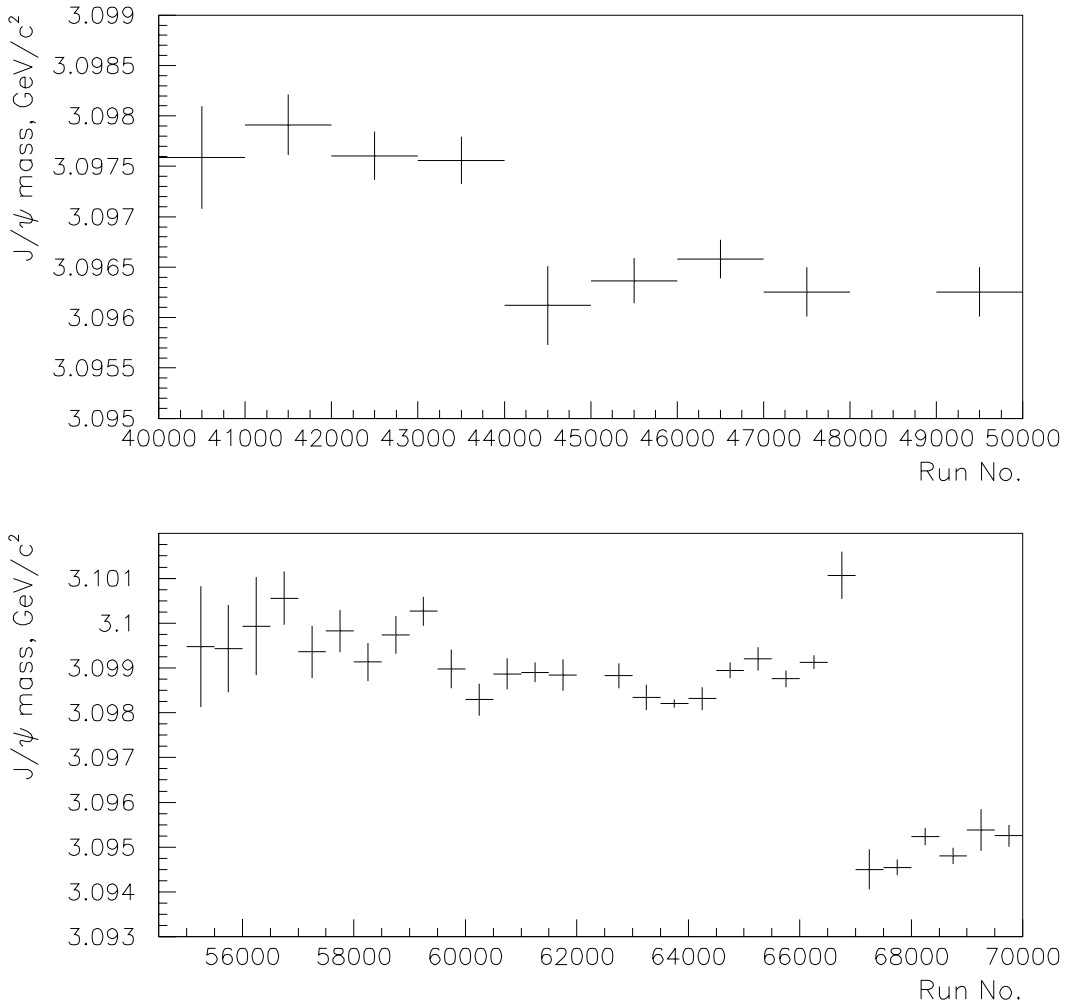

Figure 7.6: The measured J/ψ mass variation in the course of Run 1A (top) and Run 1B (bottom).

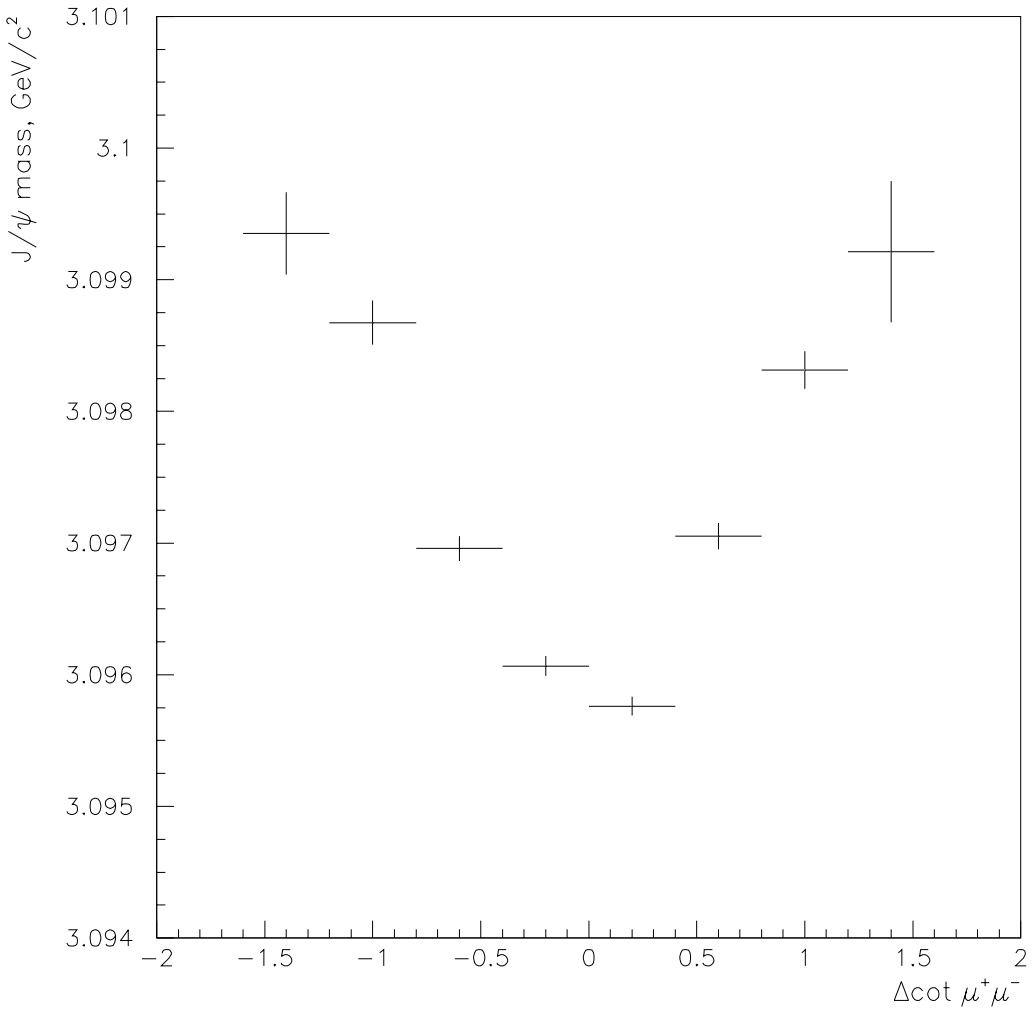

Figure 7.7: The measured J/ψ mass variation as a function of the opening angle between the two muons.

Source of Uncertainty	Change in Λ_b^0 mass, MeV/c^2
Momentum Scale	1.3
$\Delta \cot\theta$ effect	2.0
Track measurement	0.5
Energy loss	0.6
Total	3.0

Table 7.1: Systematic uncertainties in the Λ_b^0 mass measurement.

timate of the systematic uncertainty for the B^0 mass measurement. The difference between our B^0 mass measurement result and the world average value is 2.1 MeV/c^2, which is an indication that no other large source of systematic error is present in the measurement. Therefore, our Λ_b^0 mass measurement result is

$$M(\Lambda_b^0) = 5621 \pm 4(stat.) \pm 3(sys.) MeV/c^2.$$

The systematic effects influence the mass measurements of the Λ_b^0 and B^0 similarly, so the measured difference in their masses is almost free of systematic errors. We have studied the systematic uncertainty on the difference between Λ_b^0 and B^0 masses by means of Monte Carlo. The largest shift in mass difference introduced by the sources of uncertainty listed in Table 7.1 was found to be 1.0 MeV/c^2. Consequently,

$$M(\Lambda_b^0) - M(B^0) = 340 \pm 5(stat.) \pm 1(sys.) MeV/c^2.$$

7.5 Determination of $\frac{\sigma_{\Lambda_b^0} \cdot B(\Lambda_b^0 \to J/\psi\,\Lambda)}{\sigma_{B^0} \cdot B(B^0 \to J/\psi\,K_s^0)}$

To measure the branching ratio of $\Lambda_b^0 \to J/\psi\,\Lambda$ decay, we follow a procedure similar to the one described in the Chapter 6. We determine the

ratio of production cross section times branching ratio of $\Lambda_b^0 \to J/\psi\,\Lambda$ and $B^0 \to J/\psi\,K_s^0$ decays, described by:

$$\frac{\sigma_{\Lambda_b^0} \cdot B(\Lambda_b^0 \to J/\psi\,\Lambda)}{\sigma_{B^0} \cdot B(B^0 \to J/\psi\,K_s^0)} = \frac{B(K_s^0 \to \pi^+\,\pi^-)}{B(\Lambda \to p\,\pi^-)} \times \frac{\varepsilon_{B^0}}{\varepsilon_{\Lambda_b^0}} \times \frac{N_{\Lambda_b^0}}{N_{B^0}} \qquad (7.1)$$

where $B(B^0 \to J/\psi\,K_s^0) = (3.7 \pm 1.0) \times 10^{-4}$, $B(\Lambda \to p\,\pi^-) = 0.639 \pm 0.005$, $B(K_s^0 \to \pi^+\,\pi^-) = 0.686 \pm 0.003$ [8]; $N_{\Lambda_b^0}$ and N_{B^0} are the numbers of observed Λ_b^0 and B^0 events respectively, and ε_{B^0} and $\varepsilon_{\Lambda_b^0}$ are the overall reconstruction efficiencies of Λ_b^0 and B^0 states.

In order to reduce the systematic uncertainties on the ratio of reconstruction efficiencies, $\frac{\varepsilon_{B^0}}{\varepsilon_{\Lambda_b^0}}$, we impose additional requirements similar to those discussed in the Chapter 6. We require both muons to be reconstructed in the SVX. Hadrons are not required to have SVX-measured tracks, because both Λ and K_s^0 are long-lived particles and most of their decays occur outside the SVX volume. Λ and K_s^0 decay products are required to have $P_T > 400$ MeV/c and CTC exit radius greater than 130 cm to ensure the uniform tracking efficiency. We use only events where the J/ψ is measured in the CMU system, restricting the data to a pseudorapidity range of $-0.6 < \eta < 0.6$, to rely on the trigger simulation in our Monte Carlo. Figure 7.8 shows the distributions of $J/\psi\,\Lambda$ (top) and $J/\psi\,K_s^0$ (bottom) invariant masses after applying these additional selection criteria.

The unbinned likelihood fit of a Gaussian signal plus linear background yields $N_{\Lambda_b^0} = 7.8 \pm 3.4$ and $N_{B^0} = 57.6 \pm 8.7$.

The ratio of reconstruction efficiencies of the Λ_b^0 and B^0 states was found using the Monte Carlo technique developed for the $\Lambda_b^0 \to J/\psi\,\Lambda(1520)$ analysis. We find $\frac{\varepsilon_{\Lambda_b^0}}{\varepsilon_{B^0}} = 2.02 \pm 0.05$.

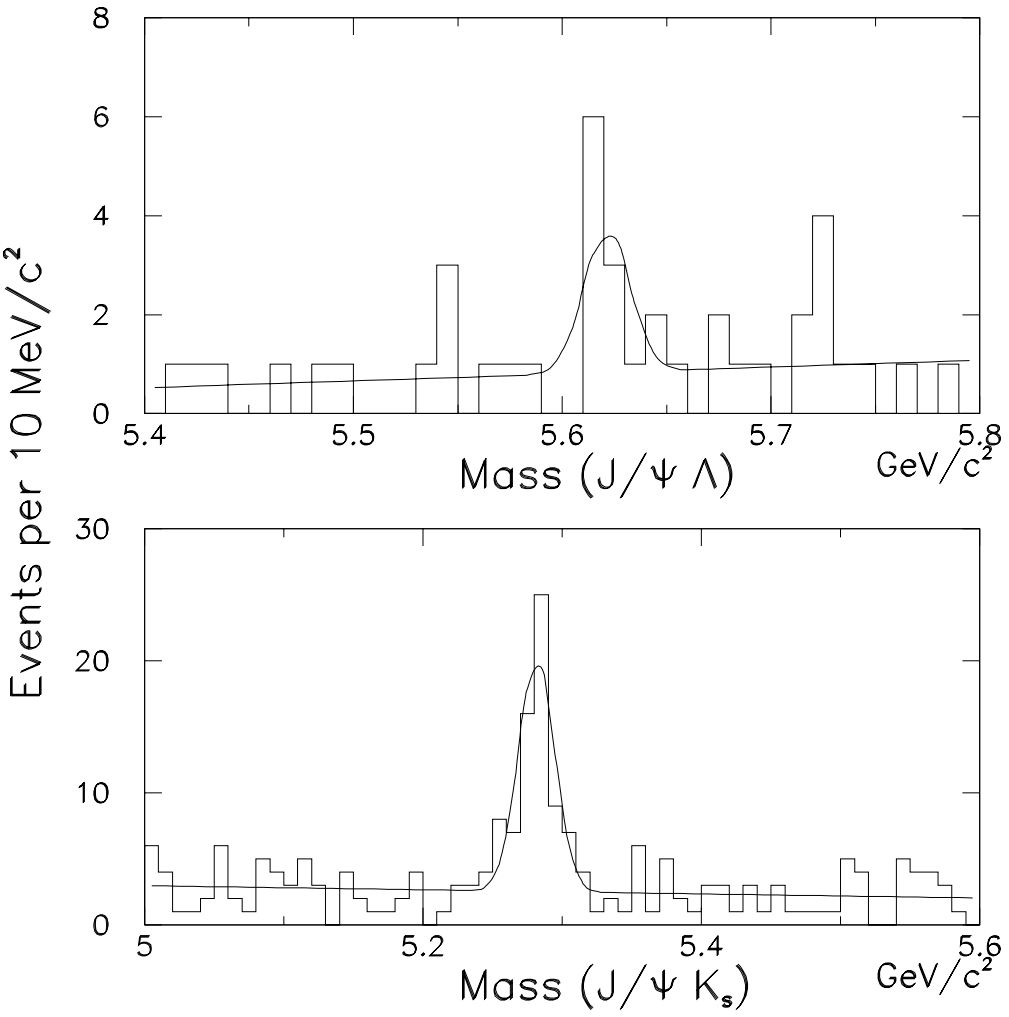

Figure 7.8: Λ_b^0 and B^0 candidates used for the Λ_b^0 production branching fraction measurement.

Source of Uncertainty	Central Value Used in Analysis	Variation Range	Change in $\frac{\varepsilon_{B_d}}{\varepsilon_{\Lambda_b}}$, %
Λ_b polarization	0	-1 — 1	15
J/ψ helicity	0	-1 — 1	2
Peterson ϵ for Λ_b	0.006	0.002 — 0.010	8.5
Peterson ϵ for B_d	0.006	0.004 — 0.008	4
$c\tau(\Lambda_b)$, μm	400	352 — 448	1.5
$c\tau(B_d)$, μm	450	417 — 483	0.5
SVX $c\tau$ resolution, μm	50	40 — 60	0.5
J/ψ trigger efficiency	standard	$\pm 1\sigma$	2.5
b spectrum	$M_b = 4.75\ GeV/c^2$, $\mu = \mu_0$	$M_b = 4.5\ GeV/c^2$, $\mu = \mu_0/4$ — $M_b = 5.0\ GeV/c^2$, $\mu = 2 \times \mu_0$	1.5
Mass uncertainty scale parameter	1.15	0.9 — 1.7	2.5
Total			19

Table 7.2: One standard deviation systematic uncertainties on $\varepsilon_{B^0}/\varepsilon_{\Lambda_b^0}$.

The systematic uncertainties that can affect $\frac{\varepsilon_{B_d}}{\varepsilon_{\Lambda_b}}$ were studied by varying the theoretical parameters known with limited precision in the Monte Carlo simulation. The summary of the uncertainties is given in Table 7.2. The greatest contribution is due to the unknown polarization of the Λ_b^0 decay. The reconstruction efficiency of $\Lambda \to p\,\pi^-$ decays is affected by the soft spectrum of the pion transverse momentum. The softness depends on the Λ_b^0 decay polarization parameters. In particular, the emission angle of the Λ with respect to the polarization direction in the Λ_b^0 rest frame, Θ, follows the distribution $I(\Theta) \propto \alpha(\Lambda_b^0)P(\Lambda_b^0)\cos(\Theta)$, where the decay parameters $\alpha(\Lambda_b^0)$ and the polarization $P(\Lambda_b^0)$ are unknown. Wide ranges of possible values for $\alpha(\Lambda_b^0)$ and $P(\Lambda_b^0)$ have been used in the simulation and we determine the 1σ variation in $\frac{\varepsilon_{B_d}}{\varepsilon_{\Lambda_b}}$ to be $\simeq 15\%$. Similarly, we vary the parameters from the other sources of

systematic uncertainty, listed in Table 7.2, and add the resulting uncertainty values in quadrature to obtain a total of 19% as a 1σ systematic uncertainty in the ratio of efficiencies.

We find the ratio of cross section times branching fraction with the $P_T(\Lambda_b^0, B^0) > 6$ GeV/c and $|\eta(\Lambda_b^0, B^0)| < 0.6$ to be

$$\frac{\sigma_{\Lambda_b^0} \cdot B(\Lambda_b^0 \to J/\psi\,\Lambda)}{\sigma_{B^0} \cdot B(B^0 \to J/\psi\,K_s^0)} = 0.27 \pm 0.12(stat.) \pm 0.05(sys.).$$

Chapter 8

Conclusions

The $J/\psi \to \mu^+ \mu^-$ sample of the 1992 – 1995 CDF data taking run has been used to search for exclusive Λ_b^0 decays. The decay $\Lambda_b^0 \to J/\psi \Lambda$ has been observed and an upper limit for the $\Lambda_b^0 \to J/\psi \Lambda(1520)$ decay established.

The Λ_b^0 mass is measured to be:

$$M(\Lambda_b^0) = 5621 \pm 4\,(stat.) \pm 3\,(sys.)\, MeV/c^2$$

and the mass difference with the B^0 is:

$$M(\Lambda_b^0) - M(B^0) = 340 \pm 5\,(stat.) \pm 1\,(sys.)\, MeV/c^2.$$

Figure 8.1 presents a summary of the results on the Λ_b^0 mass measurements reported by different experiments, showing the superior precision of our measurement.

We measure the ratio of production cross section times branching ratio for the $\Lambda_b^0 \to J/\psi \Lambda$ and $B^0 \to J/\psi K_s^0$ decays to be:

$$\frac{\sigma_{\Lambda_b^0} \cdot B(\Lambda_b^0 \to J/\psi \Lambda)}{\sigma_{B^0} \cdot B(B^0 \to J/\psi K_s^0)} = 0.27 \pm 0.12\,(stat.) \pm 0.05\,(sys.).$$

Assuming $\sigma_{\Lambda_b^0}/\sigma_{B^0} = 0.132/0.378$ [14] and $B(B^0 \to J/\psi K_s^0) = 3.7 \times 10^{-4}$ [8], we find

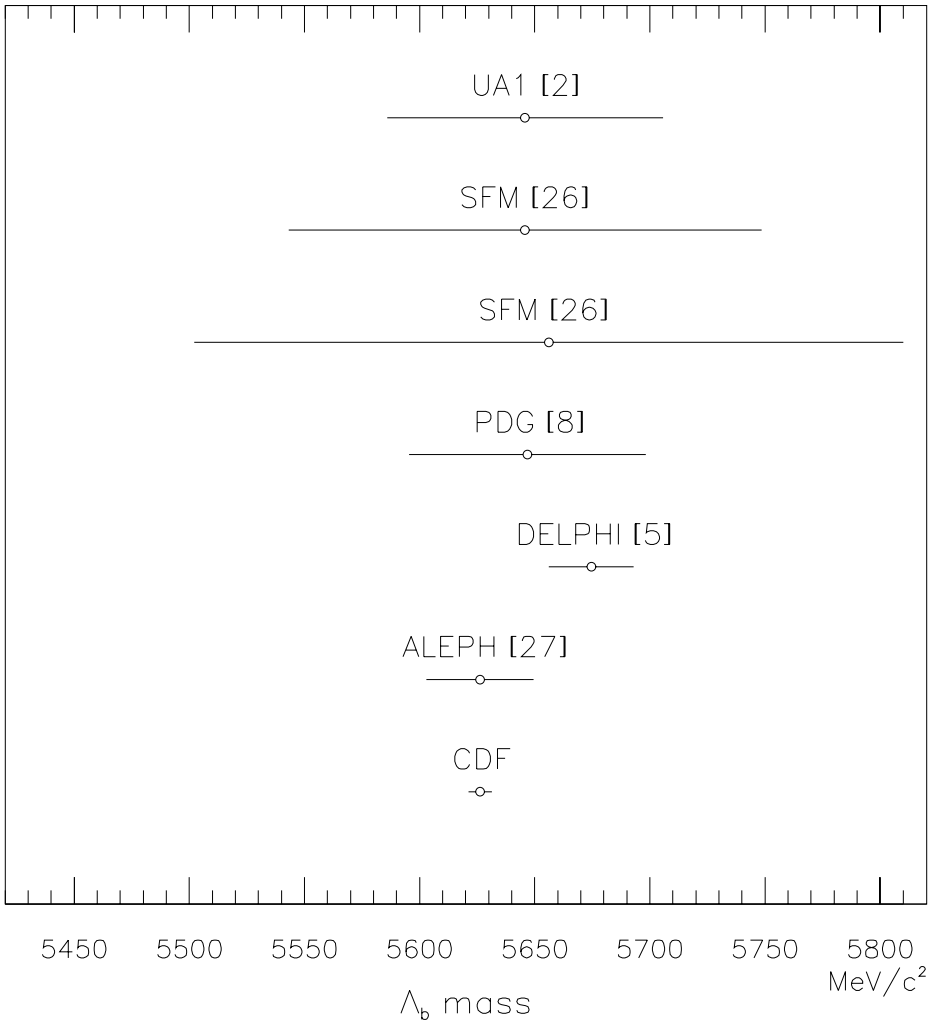

Figure 8.1: Measurements of the Λ_b^0 mass by different experiments. Error bars indicate statistical and systematic uncertainties added in quadrature.

$$B(\Lambda_b^0 \to J/\psi\,\Lambda) = (2.86 \pm 1.27\,(stat.) \pm 0.53\,(sys.)) \times 10^{-4}.$$

This value is approximately a factor of 50 smaller than the result reported by UA1 [2] and is in agreement with theoretical expectations [28] and earlier limits from CDF [3] and LEP experiments [4], [5]. Figure 8.2 presents a summary of the results on the $\Lambda_b^0 \to J/\psi\,\Lambda$ branching ratio measurements from the different experiments and theoretical predictions. We can conclude, that the branching ratio of the $\Lambda_b^0 \to J/\psi\,\Lambda$ decay mode is comparable to the branching ratios of B-meson decay with a J/ψ in the final state.

A 90% confidence level upper limit was established for the ratio of production cross section for Λ_b^0 and B^0 states times the $\Lambda_b^0 \to J/\psi\,\Lambda(1520)$ branching fraction:

$$\frac{\sigma_{\Lambda_b^0}}{\sigma_{B^0}} B(\Lambda_b^0 \to J/\psi\Lambda(1520)) < 1.38 \cdot 10^{-4}.$$

and assuming $\sigma_{\Lambda_b^0}/\sigma_{B^0} = 0.132/0.378$, we have

$$B(\Lambda_b^0 \to J/\psi\,\Lambda(1520)) < 3.95 \times 10^{-4}.$$

The fact that we do not observe $\Lambda_b^0 \to J/\psi\,\Lambda(1520)$ decay supports the theoretical prediction [7] that , $_S(\Lambda_b^0 \to J/\psi\,\Lambda(1520)) = 0$, providing an experimental input for the development of theoretical models of B-baryon decays.

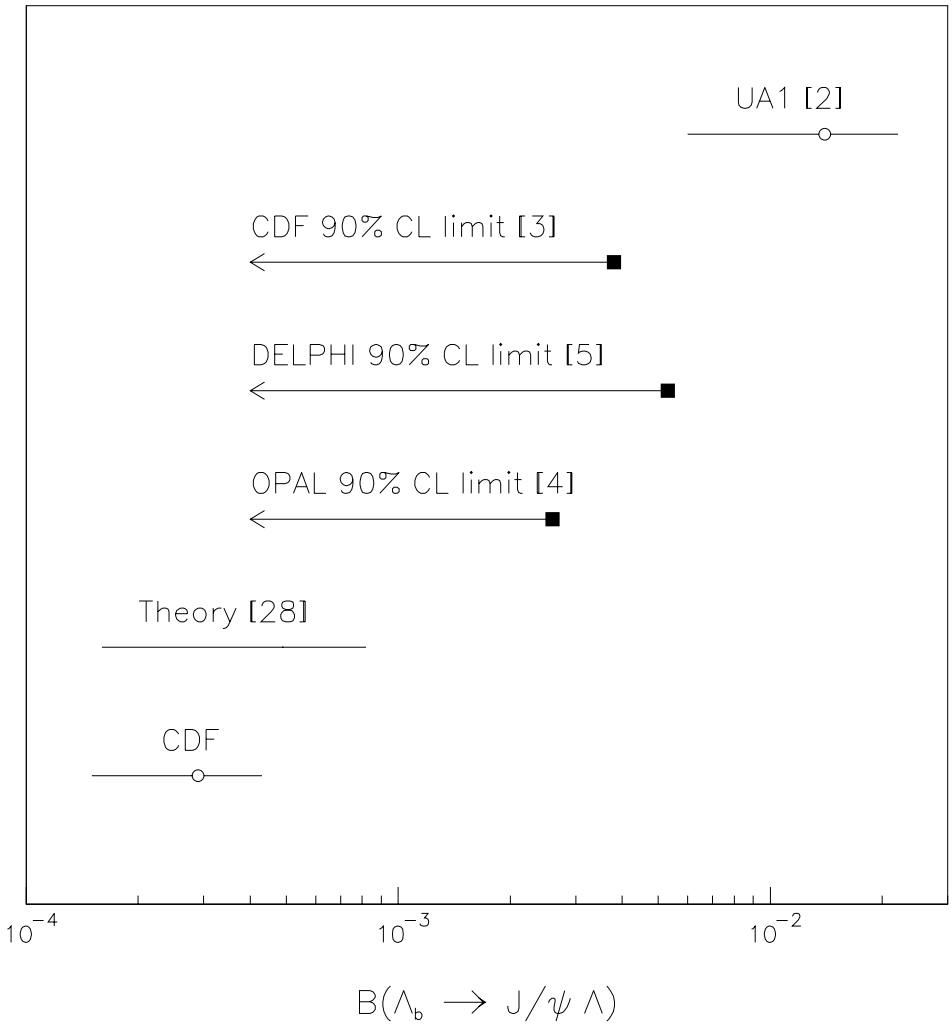

Figure 8.2: Measurements of the $\Lambda_b^0 \to J/\psi\,\Lambda$ branching ratio by various experiments, and a range of theoretical predictions. Squares indicate the 90% confidence level limits; error bars indicate statistical and systematic uncertainties added in quadrature.

Bibliography

[1] S.L. Glashow, Nucl. Phys. **22**, 579 (1961); S. Weinberg, Phys. Rev. Lett. **19**, 1264 (1967); A. Salam, *Elementary Particle Theory: Relativistic Groups and Analyticity* (Nobel Symposium No. 8), edited by W. Swartholm (Almqvist and Wiksell, Stockholm), 367 (1968).

[2] C. Albajar *et al.,* "First observation of the beauty baryon Λ_b in the decay channel $\Lambda_b \to J/\psi\,\Lambda$ at the CERN proton-antiproton collider" Phys. Lett. B **273**, 540 (1991).

[3] F. Abe *et al.,* "Search fot the Λ_b Baryon at CDF" Phys. Rev D **47** (1993).

[4] R. Akers *et al.,* "Search for Exclusive Λ_b^0 Decays with the OPAL Detector at LEP", OPAL Physics Note PN164, February 26, 1995.

[5] DELPHI Collab., P. Abreu *et al.,* "Search for exclusive decays of the Λ_b^0 baryon and measurement of its mass", submitted to Phys. Lett. B.

[6] F. Abe *et al.*, "Observation of $\Lambda_b^0 \to J/\psi\,\Lambda$ at the Fermilab Proton-Antiproton Collider" Phys. Rev. D **55**, 1142, 1997.

[7] A. Le Yaouanc, L. Oliver, O. Pène, and J.-C. Raynal "Calculations of Branching Fractions for $\Lambda_b^0 \to J/\psi\,\Lambda$ and $\Lambda_b^0 \to J/\psi\,\Lambda(1520)$", private communication.

[8] Particle Data Group, Phys Rev. D **54** (1996).

[9] H. Fritzch, M. Gell-Mann, and H. Leutwyler, Phys. Lett. B **47**, 365 (1973).

[10] P. Nason, S. Dawson, R.K. Ellis, Nucl. Phys. **B303**, 608 (1988); **B327**, 49 (1989).

[11] A. Martin, R. Roberts, and J. Stirling, RAL-92-021 (1992); DTP/92/16 (1992).

[12] C. Peterson *et al.*, Phys. Rev. D **27** (1983).

[13] J. Chrin, Z. Phys. **C36**, 165 (1987).

[14] K. Honscheild "Production and Decay of b-Flavored hadrons" Phys. Rev. D **54**, 477 (1996).

[15] N. Cabibbo, Phys. Rev. Lett. **10**, 531 (1963); M. Kobayashi and K. Maskawa, Progr. Theor. Phys. **49**, 652 (1973).

[16] CERN-Bologna Collab., M. Basile *et al.*, Lett. Nuovo Cimento 31 (1981) 97.

[17] A. Putzer Proc. Intern. Conf. on High energy physics (Lisbon, 1981), eds. J. Dias de Deus and J. Soffer.

[18] D.P. Stanley and D. Robson, Phys. Rev. D **21** (1980) 3180; Phys. Rev. Lett. 45 (1980 235.

[19] K. Maltman and N. Isgur, Phys Rev. D **22** (1980) 1701.

[20] D. Izatt *et al.,* Nucl. Phys. B **199** (1982) 269.

[21] J.M. Richard and P. Taxil, Phys. Lett. B **128** (1983) 453.

[22] J.L. Basdevant and S. Boukraa, Z. Phys. C **30** (1986) 103.

[23] A. Martin and J.M. Richard, Phys. Lett. B **185**, 426 (1987).

[24] D.B. Lichtenberg, R. Roncaglia, J.G. Wills, and E. Predazzi, Z. Phys. C **47**, 83 (1990).

[25] W. Kwong and J. Rosner "Masses of new particles containing b quarks", Phys. Rev. D **44**, 212 (1991).

[26] SFM Collab., G. Bari *et al.,* Nuovo Cimento A **104** (1991) 1787.

[27] ALEPH Collab., D. Buskulic *et al.,* "Measurement of the Mass of the Λ_b^0 Baryon", submitted to Phys. Lett. B.

[28] H.Y. Cheng Phys. Lett. B **289**, 455 (1992); H.Y. Cheng and B. Tseng IP-ASTP-22-94 (November, 1994).

[29] Izard Duniets, Fermilab, private communication.

[30] F. Abe *et al.,* "Measurement of the B meson differential cross section $d\sigma/dp_T$ in $p\overline{p}$ collisions as $\sqrt{s}$ = 1.8 TeV", Phys. Rev. Lett. **75**, 1451 (1995).

[31] R. Alexan, A. Le Yaouanc, L. Oliver, O. Pène, and J.-C. Raynal, Phys Rev D **51**, 6235 (1995).

[32] F. Abe *et al., Nucl. Instrum. Methods A* **271**, 387 (1988).

[33] C. Newman-Holmes, E.E. Schmidt, and R. Yamada, Nucl. Instrum. Methods Phys. Res., Sect. A **274**, 443 (1989).

[34] D. Amidei *et al.,* "The Silicon Vertex Detector of the Collider Detector at Fermilab" Nucl. Instrum. Methods Phys. Res., Sect. A **350**, 73 (1994).

[35] "SVX′, The New CDF Silicon Vertex Detector" Presented by F.G. Sciacca at the 6th Pisa Meeting on Advanced Detectors, Italy, May 1994.

[36] F. Bedeschi *et al.,* Nucl. Instrum. Methods Phys. Res., Sect. A **268**, 50 (1988).

[37] P. Lukens, G. Apollinari "Low Momentum Track Efficiency for the Λ_b Analysis", CDF note 3450 (December 1995).

[38] M.W. Bailey, A.F. Garfinkel, S.M. Tkaczyk "CTC Tracking Efficiency for B Cross-section Analysis", CDF note 2815 (November 1994).

[39] G. Ascoli *et al.,* Nucl. Instrum. Methods Phys. Res., Sect. A **268**, 33 (1988).

[40] F. Abe *et al.*, "Measurement of the antiproton-proton total cross section at $\sqrt{s} = 546$ and 1800 GeV", Phys Rev. D **50**, 5550 (1994).

[41] F. DeJong and R. Hans "Level 1 and Level 2 Low P_T Central Muon Trigger Efficiencies for Run 1A", CDF note 1999.

[42] G.W. Foster *et al.,* "A Fast Hardware Track finder for the CDF Central Tracking Chambers", Nucl. Instrum. Methods A **269**, 93 (1988).

[43] S. Pappas, J. Lewis " Run 1B Low P_T Central Dimuon Trigger Efficiencies" CDF note 3070.

[44] D. Frei, "Multiple Scattering of Central Muons", CDF note 1430.

[45] J. Marriner "Secondary Vertex Fit with (optional) Mass Constraints and (optional) Pointing Constraints", CDF Note 1996.

[46] C. Newman-Holmes, E.E. Schmidt, and R. Yamada, Nucl. Instrum. Methods A **274**, 443 (1989).

[47] P. Lukens and G. Apollinari "Low Momentum Track Efficiency for the Λ_b Analysis", CDF Note 3450.

[48] F. Abe *et al.*, Phys. Rev. Lett. **77**, 1439 (1996).

[49] P. Nason, S. Dawson, and R.K. Ellis, Nucl. Phys. **B327**, 49 (1989).

[50] F. Abe *et al.*, "Measurement of the Polarization in the Decays $B_d \to J/\psi K^{*0}$ and $B_s \to J/\psi\phi$", Phys. Rev. Lett 75, 3068 (1995)

[51] M.S. Alam *et al.*, Phys. Rev. D **50**, 43 (1994).

[52] Jay Orear, Laboratory for Nuclear Studies Cornell University, "Notes on Statistics for Physicists, Revised", CLNS 82/511 (1982).

[53] F. Abe *et al.*, "Measurement of the Mass of the B_s Meson", Phys Rev. D **53**, 3496 (1996).

[54] F.Abe *et al.*, "Measurement of the W Boson Mass", Phys Rev. D **52**, 4784 (1995).

[55] R. Akers *et al.,* "Measurement of the Average b-Baryon Lifetime and the Product Branching Ratio $f(b \to \Lambda_b) \cdot B(\Lambda_b \to \Lambda\, \ell^-\, \bar{\nu}\, X)$", CERN PPE-95-90, submitted to Phys. Lett. B.

[56] D. Buskulic *et al.,* "Measurement of the b Baryon Lifetime" CERN PPE-95-65.

[57] P. Abreu *et al.,* "Determination of the average lifetime of the b-baryons", Z. Phys., C **71**, 199, 1996.

[58] F.Abe *et al.*, "Beauty Baryons: Recent CDF Results", Proceedings 2nd International Conference on Hyperons, Charm and Beauty Hadrons, Montreal, Quebec, Canada, 27-30 August, 1996.